Contributions to Nanophotonics: linear, nonlinear and quantum phenomena

a dissertation presented
by
Pablo M. de Roque
to
UPC - Universitat Politècnica de Catalunya

in partial fulfillment of the requirements
for the degree of
Doctor of Philosophy
in the subject of
Photonics

ICFO - The Institute of Photonic Sciences
Barcelona, Spain
January 2022

Contents

1 Introduction

Nanophotonics can be defined as the science and technology studying the control optical fields at the nanoscale and their interaction with matter.

Let me start by reflecting on some of the words of the last sentence. The field studies optical fields. The characteristic wavelengths of these electromagnetic fields lie in the visible to near-infrared spectrum. This implies wavelengths in the 310 nm to 1100 nm range. In order to spatially control such fields we need structures with characteristic dimensions of the order of the wavelength. Structures must then be nanometric in size.

A way to control optical fields at this scale is the use of nanoantennas. Nanoantennas are the optical equivalent of radio-antennas, interfacing far- with near-fields down to the nanometer scale[1]. Acting as funnels, they concentrate radiation into the near-field, where the increased field intensities enhance the excitation rate of optical emitters[2]. Following the radio-frequency analogy, optical emitters act in this situation as current sinks[3]. Due to the increased local fields, optical antennas are also used for spectroscopic studies[4]. From zero-mode waveguides[5] to Raman spectroscopy[6,7].

Nanoantennas alternatively provide efficient interfaces between near-fields generated by light sources and radiative channels. Typical emitters include molecules[8], semiconductor quantum dots[9] and NV centers[10]. Nanoantennas increase radiation rates[11], improve radiation efficiencies[12], and affect the directionality of the radiation[13]. For this reason nanoantennas offer great promises for novel light sources, from LEDs to single photon emitters. In Chapter 2 I describe these interactions between optical antennas and single photon emitters.

A complementary way to control optical field in the nanoscale is using dielectric confinement. This is a concept analogous to transmission lines for radio-waves. Waveguides and photonic crystals provide a way to control the flow of light at the nanoscale[14]. In Chapter 3 I explore the combination of dielectric waveguides with optical antennas creating an optical

circuit for energy transfer at distances comparable to the wavelength of light.

Nanoantennas increase near-field by orders of magnitude??. In these conditions, nonlinear optical effects start to play a role. Metals offer superior nonlinear electric susceptibility, which potentially increases nonlinear effects. However they are opaque, which hampers their use in favorable phase matching conditions. Nanoantennas have subwavelenght characteristic dimensions allowing radiation to scape, and can then steer clear of this constraint. Chapter 4 is devoted to these nonlinear interactions mediated by nanoantennas.

Optical fields are functions of space, but also of time. The development of broadband femtosecond lasers and pulse shaping techniques allows control of optical field down to the femtosecond timescale. By combining shaped laser fields with microscopy techniques we have the opportunity to control the interaction between laser fields and single photon emitters. Chapter 5 explores techniques that can be applied to ultrafast laser fields and their interactions with nanometric sources of light.

Based on their success to effectively control all kinds of optical fields, plasmon supporting nanoantennas are being actively researched in the field of quantum optics. In Chapter 6 I we describe a quantum eraser experiment mediated by structures suporting surface plasmon resonances.

This thesis contains both numerical simulations and experimental contributions to the field of nanophotonics. Numerical simulations are based on the finite-differences in the time domain (FDTD) method. The method provides solutions to Maxwell's equations in arbitrary configurations. By monitoring the electromagnetic fields within the simulations, physical magnitudes can be extracted that allow us to develop an intuition for our experiments.

Experimentally, the use of microscopy techniques is imperative in all the experiments described in this thesis. High numerical aperture microscope objectives provide the maximum achievable spatial resolution using far-field optical techniques. They also provide high collection efficiencies needed to detect signals at the few-photon level. Signals are typically detected avalanche photo diodes operating in Geiger mode. The experimental framework is related to the field of single molecule detection in the solid state[15,16].

Due to the varied nature of the chapters of this manuscript, each chapter provides its own specific scientific context. The rest of this manuscript is divided as follows:

Linear interactions

Chapter 2: Subwavelength lifetime imaging using near-field microscopy

In this chapter I study the interaction between single photon emitters and optical antennas. We start the chapter introducing a method to numerically simulate the interaction. A key concept to solving Maxwell equations is that of the Green function. We will show how this function relates to the emission rate of optical emitters in a nanophotonic environment. We then describe an our efforts to build a lifetime-imaging near-field scanning optical microscope. Using this rig we are able to measure changes changes in the emission rate of single emitters that interact with resonant optical antennas.

Chapter 3: Long range energy transfer in nanophotonic environments

This is a theoretical chapter related to energy transfer between two dipole emitters in nanophotonic environmets. I generalize the one point Green function formalism introduced in Chapter 2, and show how this is related to the energy transfer rate between a donor and an acceptor. I then propose a simple hybrid structure, combining nanoantennas and a dielectric waveguide that increases substantially the energy transfer rate at distances of the order of the wavelengths of the transferred photons. The chapter finishes by discussing the role that the local density of optical states has on the energy transfer efficiency.

Nonlinear interactions

Chapter 4: Nonlinear effect in nanoantennas with deeply subwavelength features

I explore nonlinear interactions in resonant nanoantennas, in particular SHG. First I introduce a method to numerically compute the contributions to SHG generated by the metal in nanoantennas. Both surface and bulk contributions to SHG are considered. We use the numerical method to show that narrowings within the antenna shape are sources of increased SHG. The increase in SHG is attributed to increase of the local field gradients, that increase to the bulk contribution to SHG. We numerically validate our results by performing SHG measurements at the single resonant antenna level.

Chapter 5: Closed loop coherent control of single quantum dots

In this chapter I explore the control of optical fields in time. Using phase shaping methods we optimize the two-photon absorption process in single QDs. I introduce a new optimization algorithm, that allows us to perform the optimization using as feedback signal the luminesce from single QDs. We then compare our results with standard phase shaping techniques.

Quantum interactions

Chapter 6: A plasmonic quantum eraser experiment

The last chapter details our efforts to perform a quantum eraser experiment in a Young's double-slit configuration. I first explain the details and subtleties of a quantum eraser experiment. I then detail our efforts to reproduce previously reported results about how to fabricate elliptical bullseye antennas behaving as quarter waveplates. Quarter waveplates are a required part for the quantum eraser effect to take place. We then perform a quantum eraser experiment mediated by plasmons. A key component of our experiment is a bright, state-of-the-art entangle polarization entangle photon source that is described at length.

2

Subwavelength lifetime imagaging using near-field microscopy

What goes up must come down. After excitation, single photon emitters such as molecules or quantum dots experience spontaneous emission. The 'speed' or rate at which they decay can be calculated using Fermi's Golden Rule. Assuming we can approximate the emitter to be a dipole, the decay rate can be expressed within a homogeneous environment as[3]:

$$\Gamma = \frac{1}{\tau} = \frac{\pi\omega}{3\hbar\varepsilon_0}|p|^2\varrho_p(r_0, \omega_0) \tag{2.1}$$

where Γ is the rate at which an emitter radiates light of frequency ω_0 (the inverse of the excited state lifetime τ). This rate Γ is proportional (up to a multiplicative constant) to the product of the magnitude of the emitters dipole moment p and ϱ_p. The function ϱ_p is referred to as the local density of optical states (LDOS) at the point r_0 and frequency ω. What this equation tells us is that emission rate is not intrinsic to the emitter in question and given by its dipole moment $|p|^2$, but that is can be modulated by the LDOS[17]. In other words, if we can engineer the environment in the electromagnetic sense, we can change the way emitters radiate. This *effect* was first described by Purcell[18]. Before his seminal theoretical description, the excited state lifetime was thought to be an intrinsic property of a particular emitter. Now we know that this effect applies broadly to any oscillator interacting with an inhomogeneous medium: from Chinese gongs close to a sound reflecting surface[19], to the beta-decay mechanisms of Be inside C60[20].

Pioneering experimental results on the modification of spontaneous decay of optical emitters in the presence of inhomogeneities was demonstrated by Drexhage[21,22]. In these studies, an ensemble average of Eu^+ ions are placed at increasing distance away from an interface. The

values of the emission rates were found to oscillate as a function of distance to the interface. Intuitively, light emitted form the ions is reflected at the surface and interacts back on the same ions. Depending on the distance (normalized to the frequency or wavelength of the light emitted by the ions) there is a constructive or destructive interference with the original ion emission, which makes it radiate faster or slower. An interface is the simplest inhomogeneity. More advanced structures such as photonic crystal cavities were later introduced to enhance or inhibit the emission properties of optical emitters.

A complementary method to control electromagnetic fields at optical frequencies is the use of nano-antennas[1]. For radiowaves, an antenna is an interface between propagating radiation and currents. Its optical analogue interfaces optical radiation with the analogue of current generators: photon emitters. In other to study these interactions, we need to both be able to fabricate structures with feature sizes in the nanometer scale as well as control relative distances between the nanoantennas and the emitters with nanometer precision. In this chapter we will experimentally investigate how *optical antennas* modify the emission properties of single photon emitters.

Optical emitters have an additional property when compared to their classical analogs: single emitters cannot emit two photons at once from their excited state. Their emitted light presents *photon antibunching*, characterized by a second-order intensity correlation function at zero delay $g^{(2)}(0)$ smaller than one[2,3]. Such *single-photon* light fields can only be described within a quantum optical formalism and are central to a number of quantum information protocols. For generating a single photon, the emitter needs to undergo a full excitation/de-excitation cycle, introducing a time overhead and ultimately posing an upper bound on the brilliance of such photon sources. The use of nanoantennas to modify the excite state lifetime via the Purcell effect is a potential way to achieve brighter single photon sources. Additional potential increases in brightness come from an increase:

- in the emitter excitation rate. Nanoantennas funnel far-field excitation into the near-field, increasing substantially the local fields at the position of the emitters.

- in the emitter radiative efficiencies. Optical emitters always have two competing decay mechanisms: radiative, and non-radiative. By increasing the radiative rates we can improve the external quantum efficiency (emitter photon per excitation).

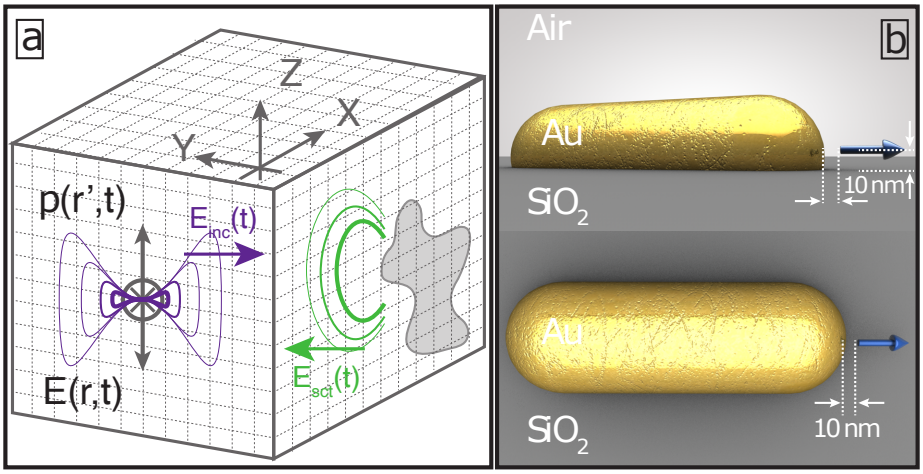

Figure 2.1: (a) Schematic illustration of the FDTD numerical method. The space containing the nanophotonic structure of choice is discretized into a numerical grid of points where fields generated by a dipole source are evaluated and propagated in time following Maxwell's equations. (b) Specific dipole-antenna arrangement for quantities shown in Figs.2.2 and Fig.2.3. The rod nanoantenna is tuned to show a dipolar resonance at 800nm. Dipole is oriented along the longitudinal resonance mode.

2.1 Optical antennas modify the excited state decay rates of single photon emitters

I will first describe a numerical method to compute the effect of arbitrary photonic environments on the radiative rates of single photon emitters. Having such a method allows us to reduce the experimental effort to study relevant structures as well as helping us interpret our experimental results.

2.1.1 Maxwell equations and numerical simulations

We are interested a method to compute the partial local density of optical states in Eq.2.1 which can be expressed as[3]:

$$\varrho_p(\mathrm{r_o},\omega) = \frac{6\omega}{\pi c^2}\left[\mathrm{n_p}\cdot Im\{\overleftrightarrow{G}(\mathrm{r_o},\mathrm{r_o},\omega)\}\mathrm{n_p}\right] \tag{2.2}$$

which tells us that the LDOS ϱ_p at the position $\mathrm{r_o}$ of a dipole emitting at a frequency ω is proportional to the projection of the imaginary part of the Green's function over the dipole orientation n_p. To calculate the Green's function, we make use of its definition as the propagator that relates the generated electric field $\mathrm{E(r)}$ by point dipole source p at $\mathrm{r'}$:

$$E(r) = \omega\mu\mu_o \overleftrightarrow{G}(r, r')p \tag{2.3}$$

where μ_o and μ are magnetic permeability constants.

Throughout this thesis we solve Eq.2.3 applying the *finite-differences in time-domain* method (FDTD). The FDTD method is a computational electrodynamics method which numerically discretizes spatial and temporal coordinates of an inhomogeneous environment of choice. Fields are evaluated in time steps at points within the numerical material *grid*[24]. The typical situation is depicted in Fig.2.1: an electric dipole source $p(r_o, t)$ excites the computational grid. The resulting fields are calculated according to Maxwell equations at the different points of the grid. By monitoring those fields at relevant positions, suitable quantities (such as the Green function in Eq.2.3) can be numerically computed. In our case, we are interested in the intermediate computation of the Green function. Once the Green function is determined we can extract experimentally measurable magnitudes such as the modification of the excited state lifetime in the presence of a nanophotonic environments. To illustrate the procedure, let us consider the emission of an electric dipole emitter in the presence of a nanorod antenna. In detail, I proceed as follows:

1. We record the amplitude of the electrical dipole $p(r_o, t)$, along with the electric field generated by it $E(r_o, t)$. Since the radiative rate modification is proportional to $\overleftrightarrow{G}(r_o, r_o)$ we record these two quantities at the same position(Fig. 2.2-left).

2. Next we perform a Fourier transform of the dipole and field amplitudes to obtain functions in the frequency (ω) domain (Fig. 2.2-right).

3. Based on the frequency domain quantities, we can express the Green function (Fig.2.3-left) as:

$$\overleftrightarrow{G}(r_o, r_o, \omega) = \varepsilon\varepsilon_o \frac{E(r_o, \omega)}{\omega^2 p(r_o, \omega)} \tag{2.4}$$

Once we determine the quantity $Im\{\overleftrightarrow{G}(r_o, r_o, \omega)\}$ (Fig.2.3) we can calculate observable magnitudes such as the change in the *radiative rate* as:

$$\Gamma_{inh} = \frac{\omega^3|\mu^2|}{2c^2\varepsilon_o\varepsilon}\left[n_p \cdot Im\{\overleftrightarrow{G}(r_o, r_o)\}n_p\right] \tag{2.5}$$

For the described emitter close to a rod nanoantenna showing a dipolar resonance at 800nm presented in Fig. 2.1-right the radiative rate enhancement has a Purcell factor $P \sim 280$ (Fig.2.3.

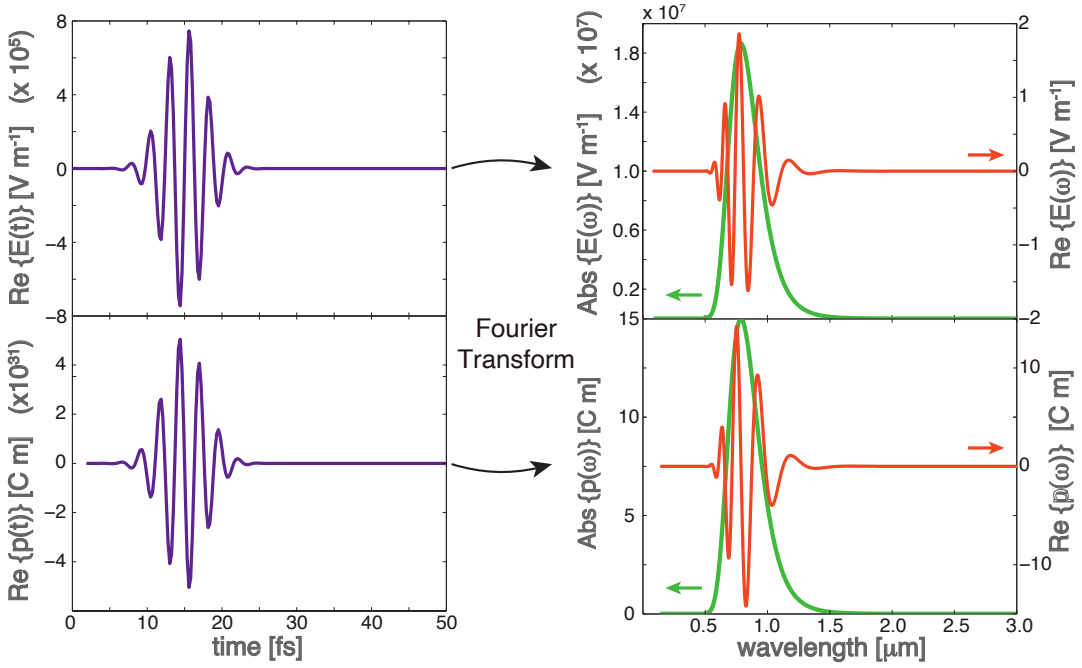

Figure 2.2: (Left) Dipole moment $\mathrm{p}(\mathrm{r_o}, t)$ (left-bottom) and field amplitudes $\mathrm{E}(\mathrm{r_o}, t)$ (left-top) recorded using the FDTD method. This corresponds to Step 1 in the algorithm. (Right) Fourier-transformed quantities $\mathrm{p}(\mathrm{r_o}, \omega)$ (right-bottom) and $\mathrm{E}(\mathrm{r_o}, \omega)$ (right-top) corresponding to Step 2 in the algorithm.

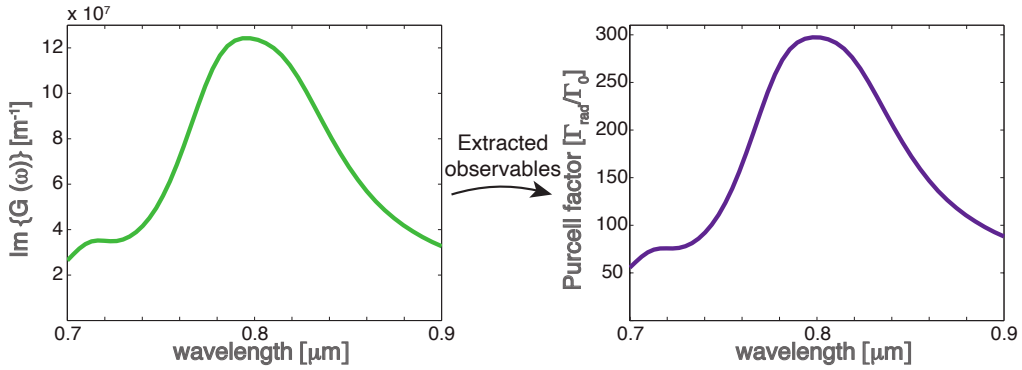

Figure 2.3: (Left) Imaginary part of the Green function for an emitter interacting with a dipolar antenna with a dipolar mode at 800nm. (Right) Purcell factor associated with the calculated Green function.

So far we performed a *one-point* calculation, but the procedure can be extended to make radiative rate change *maps* in the surrounding of a nanophotonic structure (cf. section 2.3). We should point out that performing one and only time-domain simulation gives us access to the extracted magnitudes over a wide rage of frequencies (wavelength). This is specially advantageous in the study of nano-antennas, since they typically present strong dispersive properties due to the presence of a resonance.

From Eq.2.5 we note that the decay rate in inhomogeneous environments depends *vectorially* on the Green function via its projection along the directions of the emitter orientation[17]. In order to measure the effect that this vectorial quantity has on the decay rate of emitters we cannot afford to measure ensembles, but to study them at the single emitter level. I will next describe how to build a set-up able to measure such quantities.

2.2 Experimental apparatus

2.2.1 Single molecule microscopy

Let me give some orders of magnitude numbers regarding the physical phenomena we are trying to measure, and how it relates to the field of single molecule microscopy.

In Drexhage's series experiments mentioned above, the Eu^{+} ions form part of a molecular complex with typical lifetimes reported to be between $80 - 533\mu s$[25], depending on the crystalline arrangements of the molecular films. Transition rates in the μs range are considered slow for emitters at optical frequencies. Remember also that in the original experiments there was an ensemble average of emitters, which imply higher signal levels than the those of single photon emitters. Under these circumstance of relatively slow transition rates and high signal levels, conventional detection techniques are sufficient to measure the transition rates. These conventional techniques combine a chopper (or an equivalent electro-optical modulator) and a detector with sufficient gain, such as an avalanche photodiode or a photomultiplier tube.

In this configuration, the power of the emitted signal impinging on the photodetector will be proportional to both the excitation intensity, the number of emitters in the focal spot N and their excitation cross section σ_{abs}, and weighted by the collection and detector efficiencies the $\eta_{collection}$. $P = \eta_{collection} N \sigma_{abs} I$. Assuming numbers similar to those in Eq.2.9, $\eta_{collection} \sim 1$ and $N \sim 10^6$, we get that the power impinging on the photodetector would be of the order of $\sim 4.4nW$. Typical photodiodes offer a responsivity $\sim 0.5A/W$, so there is a macroscopic current output on the order of $\sim 2.2nA$. A simple transimpedance amplifier suffices then to convert these currents into voltage signals with sufficiently low noise levels that can be traced in an oscilloscope. Note that lifetimes $\geq 10\mu s$ imply signals with frequencies $\leq 100kHz$. Since we are only considering signals featuring two time-dependent exponential functions,

a typical 50MHz bandwidth oscilloscope (widely available) is thus sufficient to sample the signals correctly.

The situation is completely different at the single emitter level. The need for microscopy techniques is imperative to study isolated emitters: high numerical aperture microscope objectives provide both the maximum achievable spatial resolution using far-field optical techniques and the high collection efficiency needed to detect signals at the few-photon level. This experimental framework derives from the field of single molecule detection in the solid state, first developed in the late 80s by W.E. Moerner and Lothar Kador[15] and in the early 90s by Michelle Orrit and Jacky Bernard[16]. These two pioneering works employed narrow-linewidth frequency-locked lasers much in the spirit of classical atomic and molecular spectroscopy to achieve single molecule detection of sufficiently diluted samples, despite the intrinsic noise of detectors configurations at the time. Early experiments, which in effect employ resonant spectroscopy techniques, needed to be performed at low temperatures, typically at the temperature of liquid He.

More specifically, single molecules in the solid state and under the right conditions at low temperature behave almost as ideal two-level system (TLS). The scattering cross-section of an ideal TLS under weak resonant excitation can be calculated to be[26]:

$$\sigma = \sigma_0 = \frac{3\lambda^2}{2\pi} \tag{2.6}$$

meaning that the scattering cross-section of a point-like two-level system is of the order of the area of a diffraction-limited spot $\pi(1.22\lambda/2NA)^2 \sim 3\pi\lambda^2/8NA^2$. Hence, we should be able to detect single molecules by monitoring the transmitted light of an incident laser tuned to the relevant resonance of this molecule impinging on a sample containing a sufficiently diluted amount of molecules. The visibility, or difference between the background and the relevant signal, can be roughly estimated:

$$T = 1 - \frac{\sigma}{\mathcal{A}_{diff}} = 1 - \frac{4}{\pi^2}NA^2 \sim 0.4 \tag{2.7}$$

That is, the transmitted signal is only $\sim 40\%$ of the incident light. Effectively, experimental visibilities tend to be smaller, since for sufficiently high numerical apertures light fields present a vectorial character[27,28,29]. Although we restricted ourselves so far to molecular systems, other emitters in the solid state behave as well as ideal TLS. Among them epitaxially-growth quantum dots[30,31,32], ion-vacancy centres in diamond[10,33,34] and rare-earth ions[35] have been investigated both as single photon sources and within in the context of cavity-QED due to the single photon non-linearities associated with their coherent properties[36]. Single-photon nonlinear properties can be used to make devices generating arbitrary *number*[37,38] or *squeezed*[39] states; used for entanglement swapping for quantum networks[40,41]; or employed to achieve quantum memories able to synchronise nodes of a network[42].

Further corrections can be made for more realistic systems. In particular, the scattering cross section of a molecule in a solid state environment can be expressed as:

$$\sigma = \sigma_0 \frac{\Gamma_1}{2\Gamma_2} \alpha_{FC} \alpha_{DW} cos^2\vartheta \tag{2.8}$$

where α_{FC},α_{DW} are the Frack-Condon and Debye-Wheeler factors that account for the branching ratio between the zero-phonon line and vibrational and phonon side-bands respectively; Γ_1 is the excited state decay rate, and Γ_2 is the coherence time of the excited state. Typical values of these factors are on the order of ~ 0.5, and $cos^2\vartheta$ is a geometrical factor that accounts for the alignment of the excitation field with the optical dipole associated with the molecule[43]. The ratio $\Gamma_1/2\Gamma_2$ further accounts for the presence of dephasing, and is important at room temperature since it takes values of the order of $10^{-5} - 10^{-6}$. For the sake of comparison, an ideal TLS at a wavelength of 600nm presents a cross-section of $1.7 \times 10^{-9} cm^2$ whereas a Rhodamine-6G molecule presents a cross section of $4.4 \times 10^{-16} cm^2$ at room temperature (and we are interested in room-temperature since we need to couple operate an NSOM on top of our molecules). This reduction on the scattering cross sections makes direct detection nearly impossible due to intrinsic detector noise. Although interferometric techniques can be applied to the detection of such emitters at room temperature[44,45], and are actively investigated since they could lead to novel label-free detection techniques[46], the more common approach is to resort to fluorescence excitation spectroscopy. Experimentally, a set of color filters of sufficient quality, typically made of dielectric multilayers, removes the background excitation laser to levels below the expected fluorescence signal. After the first room-temperature experiment performed by Betzig and Chichester[47], the technique has become widely employed in physics, chemistry, biology and materials science and has been awarded the Nobel Prize in Chemistry in the year 2014.

Let's give some numbers about order of magnitude in a typical room-temperature experiment. Let's assume we have a laser tuned to the absorption band of a molecule at room temperature, and our microscope objective allows to focus it down to a spot with a radius of $1/\sqrt{\pi}\mu m \sim 0.564 \mu m$. Let's assume we use a laser power of $1\mu W$. We can calculate the power absorbed by a typical Rhodamine-6G molecule at room temperature to be:

$$P_{abs} = \sigma_{abs} \cdot I = 4.4 \times 10^{-16} cm^2 \frac{1\mu W}{\pi \left(\frac{1}{\sqrt{\pi}\, m}\right)^2} = 4.4 \times 10^{-14} W \tag{2.9}$$

We can translate the calculated power in Eq. 2.9 into $photons \cdot s^{-1}$ using the Plank-Einstein relation $P = nh\nu$, to arrive to a number of ~ 130 $kphotons \cdot s^{-1}$ at a wavelength of 600 nm.

Improvements made to detector technology, in particular photomultiplier tubes (PMT) and silicon avalanche photo-diodes (APD) allow the detection of very low signals. In particular, when these devices are operated in so-called Geiger mode they are able to detect one

single photo-electron. This type of operation mode is achieved by setting a sufficient detector gain, and using electric current discriminators in order to discern dark counts from photon-generated current spikes after careful calibration. In effect, Geiger mode allows to detect "single photons". Assuming these molecules have a quantum efficiency 1 - that is, they emit 1 photon per absorption event - and a perfect collection efficiency, the above number is the expected count rate in our detectors. Realistic collection configurations decrease this number to typically 10%, after taking into account finite numerical aperture of microscope objectives and below unitary detector efficiency. We keep in mind that to be able to detect this signal we need to suppress the background excitation signal by a factor $P_{excitation}/P_{signal} = 1 \times 10^{-6}/4.4 \times 10^{-14} W \sim 2.3 \times 10^{-7}$, i.e., colour filters need to achieve a suppression of over 7 orders of magnitude. Further, taking into account that Geiger counters have typical dark-count rates $\lesssim 1000 counts \cdot s^{-1}$, we expect typical SNR ~ 10 or better for the mentioned excitation powers. We should mention that direct luminescence from metallic nanoantennas can also be detected using this experimental procedure. Although the luminescence efficiency of these systems is orders of magnitude smaller than molecular systems, they present much larger absorption cross-sections, effectively emitting signals comparable to those of single molecules.

In the rest of this chapter, we will describe first how to make a machine able to measure interactions between optical antennas and single quantum emitters interacting at subwavelength distances. This is one of the two main contributions I made to related NSOM (near-field optical microscopy) work within the Molecular Nanophotonics Group at ICFO. Then we will show preliminary results showing the capabilities the rig and compare them to FDTD numerical results. Methodologies related on how to simulate decay rates of emitters close to nanoantennas using the FDTD method the my second contribution related to this chapter. We will finalize with an outlook and point to the reader to other works within Niek van Hulst's group that expand on these findings[48].

2.2.2 Single emitter lifetime imaging using TCSPC

Before diving into how to how to make images, let me first discuss the capability of recording time-resolved signals coming from single emitters. Since we are detecting single-photon events, we need to resort to a *probabilistic* approach to determine study the dynamics according to the rules of quantum mechanics. Given an emitter in its excited state lifetime, it will *spontaneously decay* at *any* time with a given probability. To experimentally measure the averaged single emitter lifetimes, we need to repeat the *same* experiment over a probabilistically relevant *sample*. Only as the number of such measurements approaches infinity it will correspond to the expected value of the decay rate we are trying to measure. This approach is known as time correlated single photon counting (TCSPC).

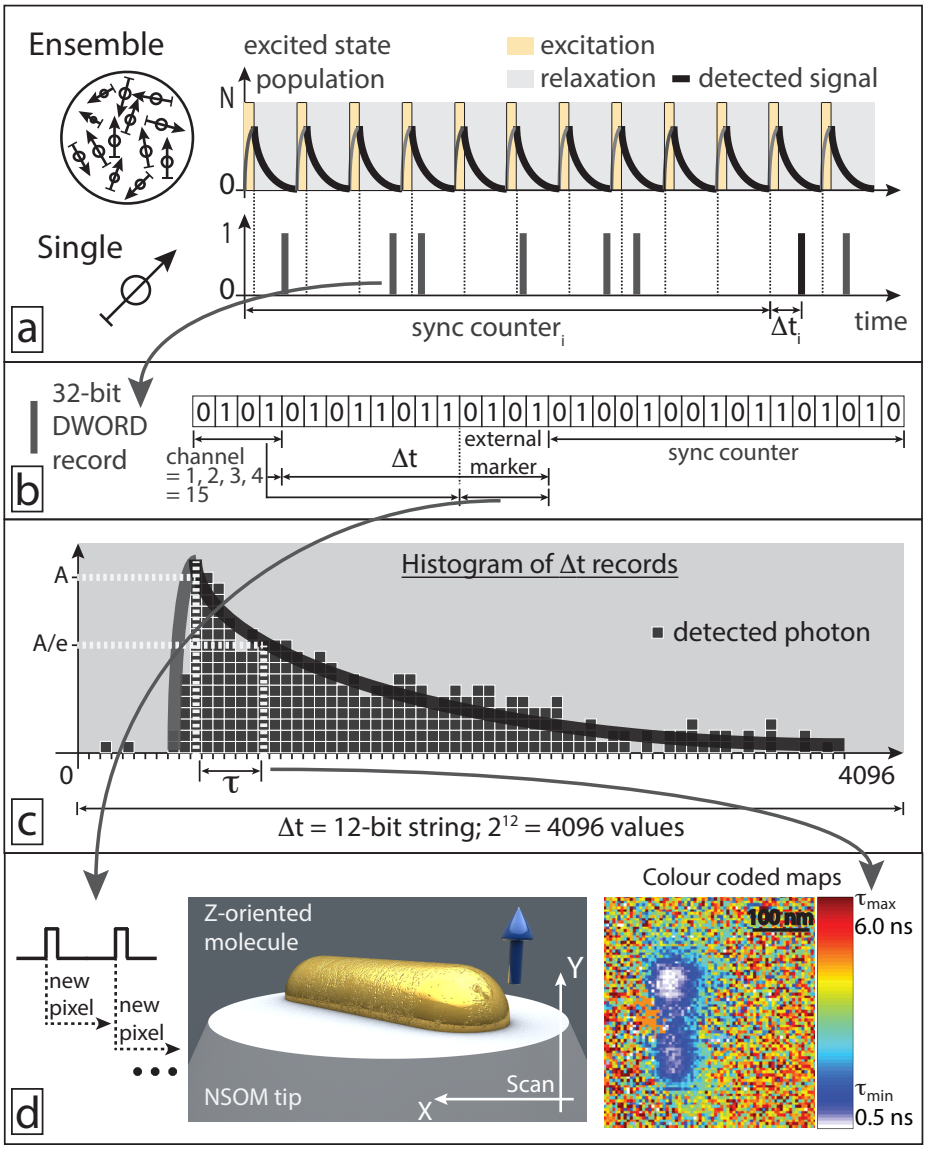

Figure 2.4: Lifetime imaging (see main text for further details). (a) Differences in signal between ensemble and single emitter: signals in ensemble measurements can be readily measured using high gain photodetectors and an oscilloscope; conversely, single emitter detection needs to make use of TCSPC tehniques. (b) 32-bit DWORD string containing the information of a single phtoon detection event using the Picoquant PH300 TCSPC card in time-tagging mode. (c) Scheme of histogram extraction from an ensemble of time-tagged records and lifetime extraction. (d) Lifetime imaging using external markets coupled to an NSOM tip. Lifetime maps can be obtained with a spatial accuracy of $\sim$ 10 nm and a time accuracy of $\sim$ 100 ps.

Single emitters radiate a single photon at a time, then we need to use APDs operating in Geiger mode (aka SPADs) to detect such low signal levels. These devices generate a macroscopic electrical currents pulses of the so-called Nuclear Instrumentation Module (NIM) standard. They can be seen as negative Vpp = -0.8 to -1.0 V, and between 15 ns - 25 ns pulses when connected to a 50Ω load oscilloscope. These signals are fed into a constant fraction discriminator (CFD).

This is 'an electrical circuit designed to mimic the mathematical operation of finding a maximum of a pulse by finding the zero of its slope'. Its purpose is to provide much better temporal resolution than what would be possible if a discriminator is set to an arbitrary signal level since different single pulses have slightly different peak heights. Subsequently, outputs of the CFD are fed into a time-to-digital converter (TDC): a high-frequency counter which operates on asynchronous signals. By measuring the number of periods of an internal reference *clock* between a *start* signal and the CFD output we get a *timestamp*. In effect the period of the clock determines the maximum temporal resolution we can achieve. To synchronise together all the single pulses over the many repetitions of the experiment, we use a pulsed laser with temporal pulse width typically of the order of (or smaller than) the temporal resolution of the electronics. In our experiment, a diode laser with pulse width $\sim$ 10*ps*. An electronic signal synchronous with the laser pulses acts as the start events of the TDC.

We use of a commercial device (PicoQuant PH300) acting both as CFD and TDC. It provides a 32-bit DWORD for each timestamp record (Fig. 2.4-b). We post-process all these timestamps to get a histogram of events (Fig. 2.4-c). As mentioned, this being a probabilistic measurement the more records we obtain, the closer the measurement will be to the true value. For simplicity the histograms are fit to single exponential functions to determine the lifetime, although this assumption may need further refinement as it could depend on the number of decay channels through which the emission can take place[49], where multiple decay channels lead to an average over multiple exponential functions.

2.2.3 Near-field optical microscope

Second part of the machine is a near-field scanning optical microscope (NSOM). Implementations of an NSOM are multiple, with the main categories divided by whether the illumination/detection is performed in the near/far-field.

In our implementation (Fig.2.5), both illumination and collection are performed in the far field, using an oil-immersion objective with high numerical aperture (NA = 1.3 - 1.4). An optical probe is then placed in close proximity to a fluorescent molecule, and the distance between the probe and the sample is maintained using closed-loop feedback electronics over the reading of the shear-force experienced by the tip[3]. In short, the optical tip is made to oscillate by a dither piezoelectric device, recording both amplitude and phase of the oscillation. Home developed dedicated circuits act on these signals to maintain them constant using a feedback

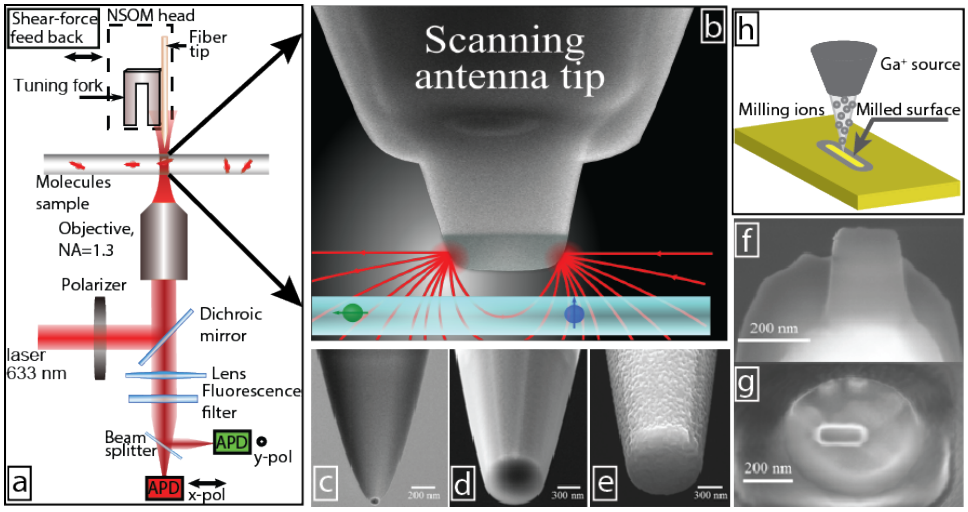

Figure 2.5: (a) Optical set-up for optical microscopy. (b) Depiction of a rod-antenna interacting with fluorescent molecules. To fabricate the optical probe we thin down an optical fiber using a puller(c), flatten this one out (d) and coat it with aluminium. FIB milling (h) allows us to carve nanostructures at the tip of the probe, like a resonant rod-like antenna (f) and (g).

loop, typically actively locking the phase of the readout[50]. The vibrating tip is then scanned around the sample using three piezo-electric aligned along the three cartesian coordinates. These piezo-electric modules (MadCityLabs Nano-LP) are in the same manner controlled by dedicated closed-loop feedback electronics (MadCityLabs Nano-Drive). Readouts from the dedicated piezo-drivers are externally driven by three 16-bit DAC outputs of an ADWin Gold II (Jäger computergesteuerte Messtechnik GmbH) while monitoring the output of the closed-loop driver by another set of three 16 bit-ADC inputs. We can drive the nanopositioners with a spatial resolution of $\sim$ 0.75nm over the 50μm movement range; whereas we can only record a nominal precision of $\sim$ 1.5nm due to the characteristics of the voltage levels of our electronics. In this way we can correlate spatial coordinates with detected photons to generate images. We generate 50ns-high TTL signals using pulse-width modulation within the ADWin, at the beginning of each pixel. These *markers* are feed to the PH300 module, allowing us to separate between different pixels by postprocesing 32-bit DWORD strings, thus generating lifetime images (Fig.2.4-d). The rig is operated using software I wrote in LabView.

In this NSOM configuration, the fluorescence molecule can be thought of as a probe itself of the local field generated by the nanoantenna (Fig.2.5-b). This allows us to we gather information about the electric field *projected* along the dipole moment of the molecule. We need then to fabricate optical probes which act as antennas at optical frequencies. The following procedure was performed by Dr. Anshuman Singh and is listed here for completeness[51]. We

proceed as follows:

- We thin down an optical fiber using a fiber-puller (Fig.2.5-c).
- The tip of the pulled optical fiber is made flat 2.5-d using an Auriga focused ion beam (FIB) milling machine (Carl Zeiss AG) (Fig.2.5-h).
- The flattened tip is coated by a film of metal, typically aluminium, using thermal and/or electron beam evaporation (Fig.2.5-d).
- We use FIB milling again to carve a dipolar antenna at the tip of the coated fiber (Fig.2.5-f and Fig.2.5-g).

By making use of molecules oriented along different directions, we can extract *vectorial* characteristics of the near-field of the antenna. Further details can be found in the works of Neumann et al[52] and Singh et al.[48].

2.2.4 Capabilities of the rig

Let us make some remarks about of our *machine* in terms of typical temporal resolution. The experimental maximum achievable temporal resolution of our TDC is $4ps$, limited by its internal clock. In effect, due to our laser pulse and electronic signals temporal width, the instrument response function is $\sim 50ps$. A *good* molecule in the solid state at room temperature will give at most $10^7 - 10^8$ photons before photobleaching. We typically take 100x100 pixels maps. That means we are left with less than 10^4 photons per histogram in each pixel, which are distributed along 4096 time-boxes (aka channels). One typically needs a 2 to 3 decades decay of an experimentally determined exponential function to make a *good fit*. Due to the limited availability of photons, we are forced to bin together adjacent channels, sacrificing on the maximum device resolution but gaining on the quality of the fit. In this manner *experimental error* is typically of the order of 100ps. Better temporal resolution can be obtained sacrificing spatial resolution.

Given a pixel dwell time in the $\sim$ 100 ms, sufficient for good time resolution, the typical image is collected and processed in about 15min. Assuming a molecule emitting 10^5 photons $\cdot\, s^{-1}$, the total pure binary information of the image amounts to $\sim$ 400 MB of data.

2.3 Results

We use spin coating to prepare 50nm-thin PMMA films on cover-slip substrates. Terrylene-diimide (TDI) molecules, a stable molecule widely used in single molecule experiments are

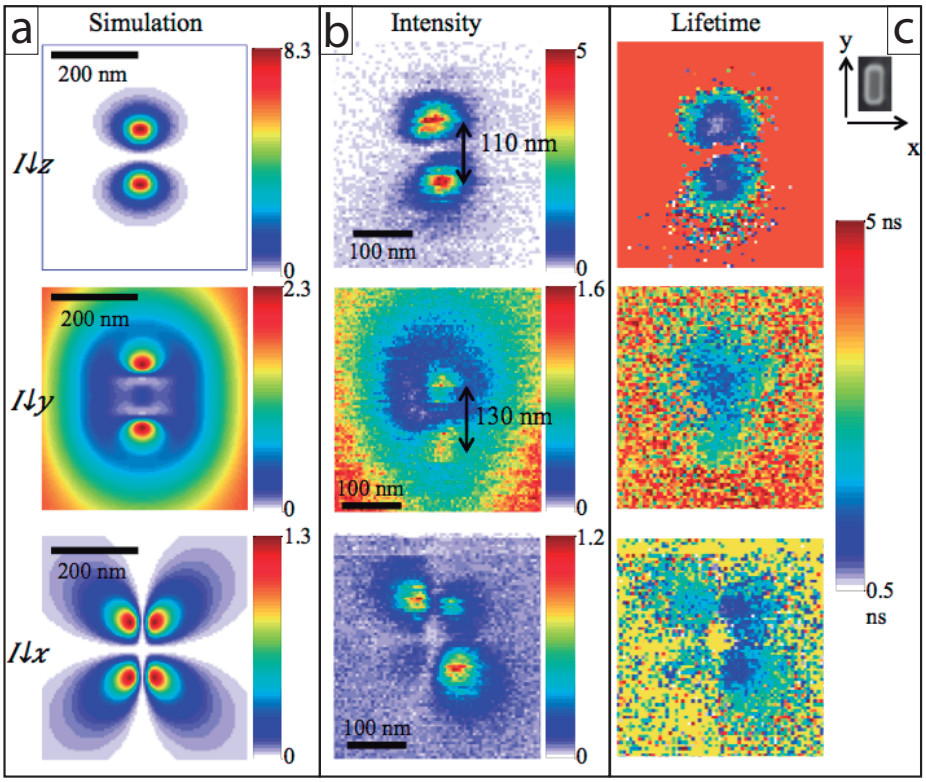

Figure 2.6: (a) Simulated electric field magnitude along the out of plane z-direction (top), y-direction (middle), and x-direction(bottom) after plane wave excitation along the longitudinal axis of the antenna. [b] Recorded photon intensities of three different TDI molecules oriented along the three different cartesian axis. [c] Lifetime images of the three molecules in [b].

diluted in the PMMA solution. Concentration is brought sufficiently down to be able to see individual fluorescent spots, typically 1 molecule $\cdot\, \mu m^{-2}$. These molecules present an absorption band centered at 650nm and a Stokes shifted emission at 680nm. Quantum efficiency of these molecules is around 90%[53,8] when embedded in a PMMA matrix. We design our dipolar optical antennas tuned to the molecules' Stokes shifted emission occuring at 680nm. Due to the broad characteristics of the dipolar resonance (Q factor $\sim 5 - 10$ is typical, translating in 150nm FWHM at the operating frequencies), the resonance overlaps the excitation band of the antenna, also providing excitation enhancement.

We present now the main result of this chapter: vectorially resolved lifetime maps of the dipolar resonance of a rod antenna. Fig.2.6-(a) shows simulated field enhancements of a rod-antenna tuned to show a dipolar resonance at 680nm. Excitation of the molecule is performed for all three molecule orientations along the long axis of the antenna. Field enhancements are presented along the out of plane direction (top), in plane and long axis (centre) and in plane short axis (bottom). Experimental measurements are presented in Fig.2.6-(b). Measured intensities correspond to a single molecule oriented out of plane (top), in-plane long-axis (centre) and in plane short axis (bottom). Experimental results are in accordance with numerical predictions. Fig.2.6-(c) shows lifetime maps for the same molecules as in (b), demonstrating the capability to vectorially map excited state decay rates. Intensity and decay rates are correlated, which implies a radiative Purcell effect, a necessary condition to generate efficient single photon sources. We refer the reader to Anshuman Singh's thesis for further details[51].

Before concluding, we should mention that previous experiments have been performed along the same ideas of measuring lifetime changes of emitters as a function of position[54,55]. However, due to the limited availability of photons emitted by molecules at room temperature, studies have been so far limited to one-dimensional scans, and never studied the full vectorial character of the LDOS. The twist in our work is that instead of starting a new measurement for every pixel, we acquire them continuously. This provides us with much better spatial resolution and higher collection efficiency.

2.4 Conclusions

Apart form the intrinsic interest of studying the vectorial interaction between single photon emitters and nanoantennas, I have motivated the potential for enhancing the brightness of single photon sources: brighter single photon sources have applications in quantum cryptography. In order to study these interactions I have *first* presented a numerical method to simulate the interaction and extract measurable changes. The numerical method presented here has benefits on itself, compared to the more widely used method in which the *power* radiated by dipolar emitters is monitored and compared to vacuum . Our method does not

require large field monitors in our computation grid. If the environment is arbitrarily complex, it might be difficult to set up such far-field monitors without overlapping with material interfaces, which would in turn introduce artifacts on the computed quantities. Furthermore, as we will see in Chapter 2 an extension of the method presented here can be used to calculate energy transfer between two dipoles in arbitrary environments. *Secondly*, I introduced an experimental device capable of measuring the near-field interaction between nanoantennas and single photon emitters. Our set-up presents higher collection efficiencies due to electronical triggering of pixel markers. This enables raster scanning the nanoantenna instead of the previously reported point-wise measurements. This allowed us to study the near-fields of the antennas vectorially. Our set-up is capable of experimentally determining LDOS-dependent radiative rates with $\sim$ 100 ps temporal resolution and 1.5nm nominal spatial resolution which is also considerably better than previously reported values.

3

Long-range energy transfer in nanophotonic environments

Place photons where they matters most. Energy transfer between an excited two level quantum emitter (donor) and an equivalent one in its ground state (acceptor) is a key process in many physical systems. It is found in naturally occurring living organisms which perform photosynthesis[56], and is widely exploited in man-made devices for lighting[57,58]. Due to its sharp inverse sixth-power distance dependence as predicted by Förster theory[59], it is also often used for bioimaging as an optical ruler to assess the co-presence of biomolecular probes[60,61]. Despite the wide range of applications profiting from it, energy transfer between two emitters is often an inefficient process, as it relies on both the spatial and spectral overlap of their radiation patterns, as well as mutual orientations. Efficient long range energy transfer could revolutionize the way we harvest solar energy[62,63], open new avenues for superresolution techniques[64], and provide new sensing[65] or lightning platforms[?]. Furthermore, it could allow efficient wireless energy transfer[66,67] and the implementation of quantum information protocols in realistic platforms[68].

In the previous chapter we have introduced an experimental TCSPC/NSOM rig which allowed us to demonstrate that by carefully placing (vectorially) single photon emitters with respect to dipole nanoantennas we could enhance the emission rates of those emitters. We could extend this vision to imagine optical circuits in which multiple single photon emitters interact within an optical circuit. This would remove the need to couple their signals by collecting and refocusing their signals in the far field. What would be the effect of complex nanophotonics environments in the energy transfer between emitters?

In this chapter I introduce a numerical method based on FDTD that allows us to quantify energy transfer in arbitrarily complex inhomogeneous environments. I then introduce

a hybrid optical circuit combining a waveguide and two dipolar antennas. This allows us to propose a novel scheme for long-range energy transfer based on near-field (via plasmonic antennas) and far-field (via dielectric waveguides) engineering. By long-range we mean distances of the order of the wavelength of the photons emitted by the donor, or equivalently $k \cdot R \sim 1$. This engineered environment can boost the energy transfer between two emitters at a distance of several wavelengths, far beyond the few-nm Förster radius, by 8 orders of magnitude. We will end the chapter by motivating why the increase is not due to an increase in emission rate from the donor, but an enhancement per donor emitted photon.

3.1 Relation between energy transfer and LDOS

Engineered nanophotonic materials largely modify the local density of optical modes (LDOS) available to an emitter and hence its spontaneous emission rate[18], as seen in the previous chapter. The LDOS varies with the emitter position in an inhomogeneous environment, and can be obtained from the dyadic Green's function, via its imaginary part $\mathrm{Im}[G(r, r)]$, at the emitter location r. Energy transfer, instead, is related to $G(r_D, r_A)$, function of both the donor (r_D) and acceptor position (r_A).

Beyond Förster theory, an equivalent of the Purcell effect for energy transfer in nanostructured media, i.e. a dependence of the energy transfer rate on the LDOS, has theoretically been expected to follow either a linear dependence[69], a quadratic dependence[70] or even to be independent of the LDOS[71]. This has fueled an ongoing experimental debate on the role of LDOS on energy transfer: energy transfer experiments in dielectrics and moderately small emission rate enhancements have shown energy transfer efficiencies which do not depend on the LDOS[72,73]. On the contrary, for the case of plasmonic nano-apertures or films, with larger donor-acceptor distances and stronger LDOS enhancements, energy-transfer efficiencies which depend on the LDOS of the photonic environment have been reported[74,75]. The role of large LDOS gradients on energy transfer in nanostructured materials is still unclear and a flexible and practical theoretical method embracing them has so far been lacking.

Here, using finite-difference time-domain (FDTD) modeling, a 3D vectorial numerical method including retardation effects and the full metal losses[24], we compute energy transfer in the presence of arbitrary inhomogeneous environments by calculating both the Green's function and induced polarizability of the acceptor.

3.2 Numerical method to calculate energy transfer using the FDTD

I employ a commercially available FDTD software (Lumerical FDTD solutions) to numerically solve Maxwell equations in arbitrarily complex nanophotonic environments. The technique described here after can be easily extended to other FDTD software such as MEEP[76].

In order to perform energy transfer calculations using the FDTD method we need to calculate two quantities in Eq.3.3: (1) The Green dyad function $G(r_A, r_D, \omega)$ and (2) The induced acceptor polarizability $\alpha_A(\omega)$. We calculate theses two quantities as follows:

1. $G(r_A, r_D, \omega)$: a dipole at the position of the donor $\mu_D(t)$ excites an electromagnetic field in the computational grid. We record the evolution of the electromagnetic field $E(r, t)$ as a function of time at the positions r_A for which we are interested in evaluating energy transfer. Fourier transforming the previous quantities to $\mu_D(\omega)$ and $E(r_A, \omega)$ allow us to calculate the sought quantity for a range of frequencies ω in just one simulation:

$$G(r_A, r_D, \omega) = \frac{E(r_A, \omega)c^2\varepsilon}{\omega^2 p_D(\omega)} \tag{3.1}$$

2. $\alpha_A(\omega)$: we perform a second simulation in which a dipole $mu_A(t)$ at r_A is recorded as a function of time. Simultaneously, we record the electric field generated $E(r_A, t)$ at its same position. After Fourier transforming both quantities, the induced polarisability is computed as:

$$\alpha(\omega) = \frac{p_A(\omega)}{E(r_A, \omega)} \tag{3.2}$$

The last step, meant to calculate the induced polarizabilities, should be performed at all the positions r_A at which we want to evaluate energy transfer. We note here that in the case in which donor and acceptor are placed at equivalent position (the system is invariant under particle exchange), only one simulation has to be performed, since the induced polarizability of donor is the same as the acceptor. For such cases both quantities can be computed in one simulation run. Furthermore, in the case in which all the positions are equivalent with respect to the inhomogeneous structure only one simulation would be required.

These two quantities, together with the LDOS-related $G(r_D, r_D, \omega)$ function introduced in Chapter 1, allow us to calculate the energy transfer rate between a donor (p_D) and an acceptor (p_A) as described in Fig. 1a, when normalized by the donor decay rate as:

$$f = \frac{\Gamma_{DA}}{\Gamma_D} = \frac{\varepsilon_o \mathrm{Im}[\alpha_A(\omega)]|p_D \cdot G(r_D, r_A, \omega)p_A|^2}{\mathrm{Im}[p_D \cdot G_D(r_D, r_D, \omega)p_D]}, \tag{3.3}$$

where ε_o is the vacuum permittivity, $G(r_D, r_A, \omega)$ is the dyadic Green's function describing the photonic environment, and $\alpha_A(\omega)$ is the polarizability of the donor electric field at a frequency ω[3].

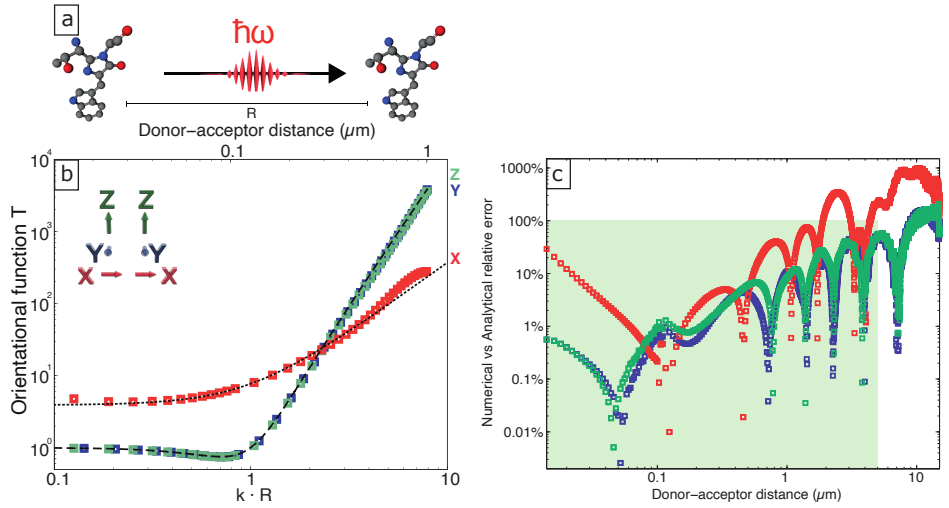

Figure 3.1: Lifetime. (a) Schematic illustration of energy transfer between two equivalent molecules. (b) Agreement between our numerical (symbols) and Förster theory (dashed line for parallel dipoles and dotted line for collinear dipoles) calculation of energy transfer for dipole pairs in vacuum separated by a distance R (λ = 800 nm). The orientational factor T(ω) between a donor and an acceptor oriented along each of the three cartesian axis, labelled as in the inset, is shown. [c] Distance dependence of the relative error between the numerical approximations and the exact analytical values expressed as percent error. The relative error increases with the donor-acceptor distance. All presented simulations were performed in an euclidean space. We use a simulation region meshed using cubes with a side of 8 nm. The three different donor-acceptor orientations presented (YD-YA (□), ZD-ZA (□) and XD-XA (□) squares) present slight differences of the error values. This is a result of the different efficiencies of energy injection into the simulation mesh from the differently oriented dipoles, as well as the evaluation of vectorial quantities at positions where these quantities are interpolated.

While the energy emitted by a dipole depends on the dipole's own scattered-field emitted at a former time, energy transferred from the donor to the acceptor instead depends on both the donor field $E(\mathrm{r}_A)$ that reaches the acceptor and the acceptor dipole moment that this field induces, which is $\mu_A = \alpha_A(\omega)E(\mathrm{r}_A)$. In homogenous optical media[77,78], simple inhomogeneous environments like multilayers[69] or spherical particles[79], radiative corrections to the electrostatic polarizability have been introduced analytically and the energy transfer can be calculated. Solutions to Eq.3.3 for lossy and more complex structures require more care and are often tackled by defining quasi-normal modes[80], or treated using the quasi-static approximation[81]. Instead the technique described in this chapter can be applied vectorially to arbitrarily complex inhomogeneous media while taking into account any retardation effects.

Eq.3.3 shows that energy transfer per emitted photon (normalized by Γ_D) can be boosted by either: increasing the polarizability at the acceptor position $\alpha(\omega)$ via near-field enhancement, or by engineering how the field emitted by the donor reaches the acceptor via $\mathrm{G}(\mathrm{r}_D, \mathrm{r}_A, \omega)$.

3.3 Validation of the numerical method

In vacuum (or homogenous media), Förster theory analytically computes the energy transfer by defining the *orientational* T factor as:

$$T(\omega) = 16\pi^2 k^4 R^6 |\mu_D \cdot \mathrm{G}(\mathrm{r}_D, \mathrm{r}_A, \omega)\mu_A|^2 \tag{3.4}$$

where k is the wavenumber at the frequency ω and $R = |\mathrm{r}_D - \mathrm{r}_A|^3$.

In Fig. 3.1(a) we compare the analytical values of Eq.3.4 with our numerical results for dipole pairs oriented along the three cartesian axis. There are three regimes characterizing the interaction:

1. Near field ($k \cdot R \leq 0.5$): Evaluation of $T(\omega)$ for values of $k \cdot R \leq 1$ shows an almost flat line. Since $\Gamma_{DA} \propto T(\omega)/R^6$, we recover the well known R^{-6} Förster analytical result.

2. Mid-to-far field ($0.5 < k \cdot R < 1$): energy transfer depends on the relative orientation between the two dipoles:

   - Non-collinear parallel dipoles (y-y and z-z) show a transfer rate that drops at intermediate distances decaying as R^{-4}, characteristic of an inductive intermediate field.
   - Collinear dipoles (x-x) show an energy transfer rate that decays monotonically as R^{-4}

3. Far field ($k \cdot R > 1$): energy transfer depends again on the relative orientation between the two dipoles:

   - Non-collinear parallel dipoles (y-y and z-z) show the usual R^{-2} energy transfer rate dependency characteristic of interactions mediated by transversal photons.
   - Collinear dipoles (x-x) still show an energy transfer rate that decays monotonically as R^{-4} in the far-field

Despite the usage of a numerical software, always prone to numerical approximation errors, the agreement between analytical and numerical values is remarkable. As any numerical technique, it is prone to show numerical errors due to the discrete representation of quantities in a binary computer. Besides, FDTD present a specific artifact, namely different positions in the grid store different field components for the method to be accurate to second-order. A particular structure is discretized into a grid of points, in our case we use a cubic mesh, at which the electromagnetic field is computed. Our sources of electromagnetic field (donors) are dipoles placed at different positions in the grid. The same applies to the positions at which we evaluate fields (acceptors). In order to extract the field components at these particular positions the software performs a linear interpolation between points in the discretization. In Fig.3.1[c] we show the relative error between the analytical solution and our numerical method for dipole-dipole energy transfer in vacuum. We note that different components present different behavior due to the different interpolation on the grid.

In the case of Fig.3.1[c], the relative error is always smaller than 100%, corresponding to a factor 2 deviation for distances as large as 5 μm. This distance interval represents over 6 wavelengths at the central wavelength (800 nm) of the present simulations. The distances over which our method is fairly accurate account for the near-field, intermediate-field and far-field regimes of energy transfer between donor and acceptor. This numerical error is responsible for the departure against the analytical result in the X_D-X_A (□ values in Fig.3.1[b] as we approach $k \cdot R \sim 10$. We note however that the error of the numerical approximations can be reduced using finer meshes at the cost of increased computational resources.

In the following figures on this chapter we will show error bars representing 100% relative error for all distances. The error bars should be then interpreted as an upper boundary overestimating the approximation errors.

3.4 Energy transfer in nanostructured media

Nanostructured media modifies the emission rate of an emitter by changing its coupling to the electromagnetic field modes as shown in Chapter 2. Using the method previously described we will show how a hybrid waveguide-antenna system can modify long-range energy transfer from one dipolar emitter to another.

We consider as a waveguide a free standing silicon nitride membrane, 200 nm thick and 400 nm wide, with refractive index $n = 2$. The electric field intensity generated by a y-oriented dipole placed 10nm above the surface couples well to the TE waveguide mode as shown in Fig.3.2[a]). Due to its dimensions, the waveguide only support one single TE mode[82]. This should help us remove complexity to the analysis that follows. To allow for fair comparison, we will consider three configurations for the energy transfer between two donor-acceptor dipoles oriented along the y direction: (1) in vacuum, (2) over the bare dielectric waveguide,

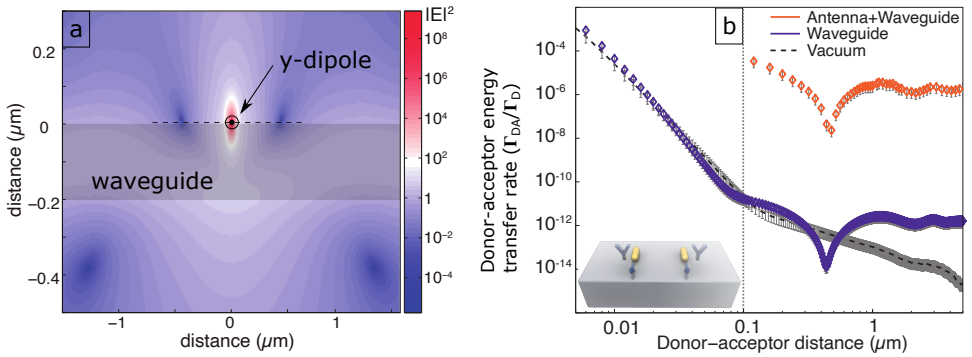

Figure 3.2: [a] Optical antennas increase donor emission rate as compared to vacuum. Donor orientation along the longitudinal direction of the antenna (blue diamonds) shows larger enhancement than dipolar orientations transversal to the optical antenna (orange and green diamonds) as a result of larger near-field coupling between the dipole emitter and the optical antenna. [b] An acceptor in vacuum (left) has same induced polarisabilities for all three perpendicular orientations, this comes as a consequence of the homogeneity of vacuum space. Induced polarisabilities increase when the emitter is close to a dielectric waveguide (middle) and it depends on the orientation of the dipole. Maximum induced polarisability occurs for acceptors coupled to the antenna tunned to its dipolar resonance (right), in particular for orientations matching the near field profile of the dipolar mode of the rod antenna.

and (3) over the dielectric waveguide and coupled to metallic antennas.

Fig.3.2[b] shows the frequently used parameter $f = \Gamma_{DA}/\Gamma_D$, which compares the energy transfer channel to other decay mechanisms. In the vacuum(1) and bare waveguide(2) configurations, energy transfer for distances shorter than 100 nm (vertical dotted line) decays as R^{-4}, characteristic of coupling mediated by the intermediate-field. For larger distances, the differences between vacuum and the waveguide become more evident. At a distance of roughly 1 μm from the donor position, a lossless waveguide mode has developed, which efficiently delivers the light to the acceptor with minimal propagation loss. As a consequence, the transfer rate stops decaying for increasing donor-acceptor distances and instead saturates at a value of $\sim 2.5 \cdot 10^{-12}$ transferred photons per donor-emitted photon. This corresponds to an energy transfer enhancement of around 25 times when compared to vacuum at a distance of 1 μm. The dip in Fig. 3.2[a](purple symbols), at roughly 400 nm distance, is due to the way the radiation of the dipole is fed into the waveguide modes, as the dipole emission peaks at the critical angle of the air-silicon nitride interface[3]. We note here that for a dipole oriented along the y-direction, only $\sim 20\%$ of the total radiation is coupled into the waveguide mode (at a wavelength of 800 nm), and only half of this ($\sim 10\%$) is coupled into the direction of the acceptor, similar to previous predictions[83]. Although the dielectric waveguide shows an increased long range energy transfer as compared to the vacuum case, the total rate is still limited to $\leq 10^{-11}$ transfer events per donor emission event (at distances $\geq 1\mu$m) which is far too

low for any potential application with real single photon emitters.

Efficient long-range energy transfer pathways must connect donor and acceptor near-fields. A waveguide mode is an excellent solution for large distances, but it is not effective in the near-field where its TE mode overlaps weakly with the dipolar emission pattern of emitters. Resonant plasmonic antennas can boost the emitter dipole moment and enhance both emission and absorption of light[1]. Moreover, they can redirect the radiation of the emitter into specific optical modes[13], leading to controlled scattering of the waveguide mode to match the dipole field. Our strategy is to place a plasmonic nano-antenna on the surface of the waveguide near the emitter, which we referred above as configuration (3). This hybrid system can out-perform the pure waveguide by (i) increasing near-field coupling of the donor with the waveguide, (ii) enhancing the donor decay rate by Purcell enhancement and (iii) boosting acceptor polarizability by local field engineering. We consider a configuration in which the donor and acceptors are placed 10 nm above the substrate and 10 nm away from the end of a 100 nm long 40 nm wide gold antenna (inset to Fig. 3b). In this antenna-mediated configuration, the absolute energy transfer rate reaches a value of $\sim 2.5 \cdot 10^{-6}$ transfer events per donor emission event for distances longer than 1 μm (Fig. 2b). This is an increase of 6 orders of magnitude when compared to the waveguide alone and over 8 orders of magnitude when compared to vacuum. We additionally explore the distance dependence of energy transfer, and show that its increase in the presence of our nanophotonic environments is due to both an increase in the donor emission rate as well as an increased number of optical modes connecting efficiently donor and acceptor.

In a realistic experiments, for example with two stable molecules or quantum dots which can emit up to 1-10 Mphoton s^{-1}, the rate of transferred photons in the presence of our waveguide-antenna structure would then be ~100-1000 photon s^{-1} (assuming 100% donor-acceptor spectral overlap).

3.5 Purcell effect and induced polizabilities

I will now discuss the terms in Eq.3.3 not related to $G(r_D, r_A, \omega)$.

For the waveguide geometry shown in Fig.3.2[a] we obtain Purcell factors $P_x \sim 2$, $P_y \sim 2$ and $P_z \sim 3$, for dipoles oriented along the three cartesian axis. The waveguide is mildly dispersive, yielding Purcell enhancement values that do not change considerably as a function of the wavelength. On the contrary, the radiative enhancement of the donor emission rate around the optical antenna, shown in Fig.3.3[a], is remarkably high and dispersive[1]: an emitter with transversal orientation along the antenna experiences a considerable emission rate modification ($P_y \sim 330$), since it couples efficiently to the near-field dipolar mode of the antenna. Transversally oriented emitters couple to the transversal modes of the antenna, which are not efficiently excited when the dipole is located at the end of the rod antenna, making

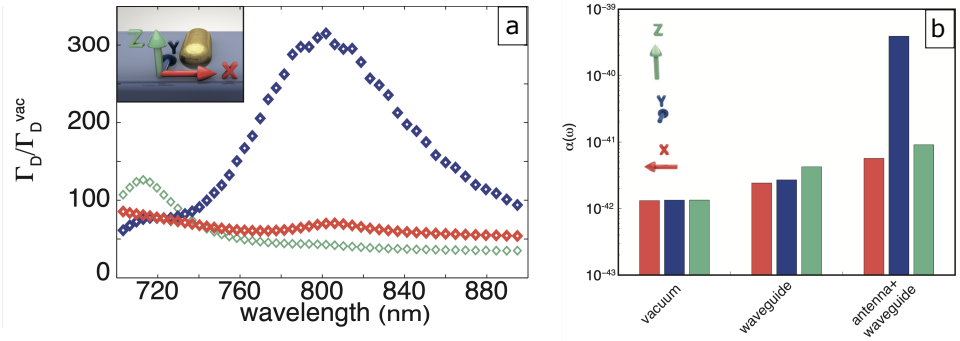

Figure 3.3: [a] Optical antennas increase donor emission rate as compared to vacuum. Donor orientation along the longitudinal direction of the antenna (blue diamonds) shows larger enhancement than dipolar orientations transversal to the optical antenna (orange and green diamonds) as a result of larger near-field coupling between the dipole emitter and the optical antenna. [b] An acceptor in vacuum (left) has same induced polarisabilities for all three perpendicular orientations, this comes as a consequence of the homogeneity of vacuum space. Induced polarisabilities increase when the emitter is close to a dielectric waveguide (middle) and it depends on the orientation of the dipole. Maximum induced polarisability occurs for acceptors coupled to the antenna tunned to its dipolar resonance (right), in particular for orientations matching the near field profile of the dipolar mode of the rod antenna.

their associated Purcell factors smaller than in the longitudinal case ($P_x \sim 6$, $P_z \sim 7$). We will use these values later when discussing the dependency of the energy transfer rate on the LDOS.

Fig.3.3 shows the induced polarizabilities in the three configurations. For the base waveguide case we achieve moderate increases, with the values by a factor 2-3 depending on the dipole orientations, with respect to the vacuum case. A more substantial increase is obtained when the nanoantennas is present, with values exceeding 2 orders of magnitude in the most favorable dipole orientation. This most favorable orientation corresponds to the energy transfer enhancement presented in Fig.3.2-b, were we reported an increase of the energy transfer rate per emitter photon of over 8 orders of magnitude against the vacuum case. Since this increase is the product of the induced polarizability times the $G_D(r_D, r_D, \omega)$ part, we can conclude that the Green function mediated transfer is boosted by 6 orders of magnitude in the hybrid-structure case.

3.6 Energy transfer between perpendicular dipoles

In homogeneous environments, long-range energy transfer is mediated by transversal photons parallel to the orientation of the emitters. Perpendicular donor-acceptor pairs have far-field radiation patterns with orthogonal polarization to the dipole moments, so long-range energy transfer is forbidden in those configurations. Fig.3.4-left shows the energy transfer be-

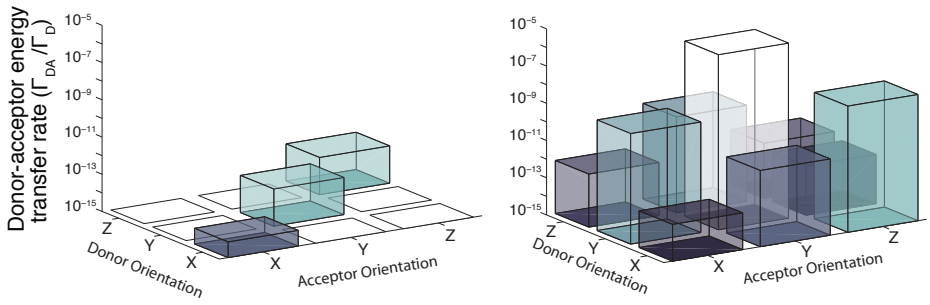

Figure 3.4: Energy transfer rate for donor and acceptor separated by $1\mu m$. Different relative dipole-dipole orientations along the cartesian axis for dipoles in vacuum [a] and mediated by the hybrid photonic structure described in the text [b].

tween two dipoles oriented along the three cartesian axis. Collinear dipoles (X_D-X_A) show reduced energy transfer than the parallel configurations. This a result of the smaller overlap of their radiation patterns.

The case of our waveguide+antenna hybrid structure is shown in Fig.3.4-right. Not only the absolute values for the parallel dipoles are increased by several orders of magnitude, but we see energy transfer for perpendicular dipoles that are orders of magnitude higher than the most favorable configurations in the vacuum case. This result has practical implications: hybrid optical circuits remove the need to perfectly orient emitters.

3.7 Dependence of energy transfer on LDOS

In order to highlight the energy transfer spatial dependence, we define a new figure of merit $\xi(r_D, r_A)$, which represents the enhancement of the normalized-to-donor-emission energy transfer rate in the presence of inhomogeneous environments compared to vacuum:

$$\xi(r_D, r_A) \equiv \frac{f^{inh}}{f^{vac}} = \frac{\Gamma^{inh}_{DA}/\Gamma^{inh}_{D}}{\Gamma^{vac}_{DA}/\Gamma^{vac}_{D}} = \frac{\Gamma^{inh}_{DA}}{\Gamma^{vac}_{DA}} \frac{1}{P_D}, \tag{3.5}$$

where the term $P_D = \Gamma^{inh}_D/\Gamma^{vac}_D$, accounts for the Purcell enhancement at the donor location.

Let me describe the distance dependence of $\xi(r_D, r_A)$:

- Interaction between donor and acceptor on a dielectric waveguide (Fig.3.5[a]):
  - Short range: at short donor-acceptor distances below $\sim$ 10 nm (dotted line Fig.3.5[a]) $\xi(r_D, r_A)$ is close to unity within our numerical errors for the waveguide-only case

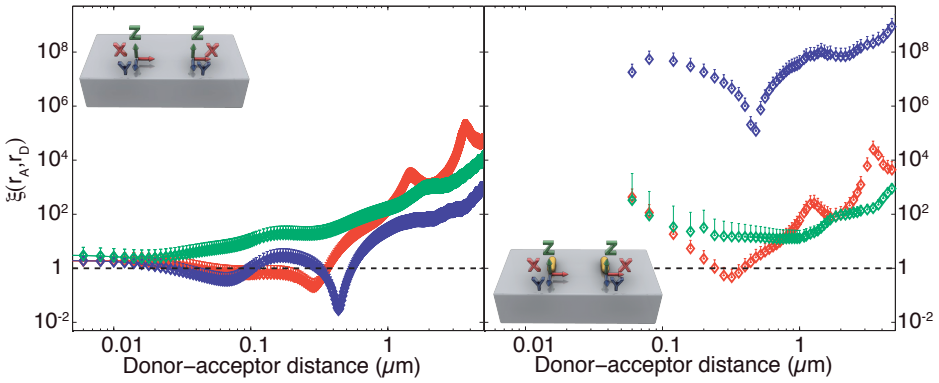

Figure 3.5: Distance dependence of $\xi(\mathrm{r}_D, \mathrm{r}_A)$ for dipole orientations along $X_D - X_A$ (orange), $Y_D - Y_A$ (violet) and $Z_D - Z_A$ (green). The graph plots $\xi(r_D, r_A)$ for the case of energy transfer mediated by a dielectric waveguide (a) and by optical antennas on a dielectric waveguide (b). The efficiency of energy transfer is maximised for y-oriented dipoles in a hybrid antenna-waveguide geometry. A deviation from unity is clear in both cases, starting from around 10 nm for the waveguide only case.

for all different dipole orientations, with only an offset related to their different Purcell factors. We checked that when normalised by the Purcell factor the three curves are identically equal to unity for very short distances (flat dashed line in Fig.3.5a).

– Deviations are instead visible for larger donor-acceptor separations, of the order of $R \gtrsim 10$ nm. As already pointed out by Blum et al.[72], energy transfer would not depend on the LDOS if one can assume that $\mathrm{Im}[\mathrm{G}(\mathrm{r}_D, \mathrm{r}_A, \omega)]$ can be approximated by the zero-order Taylor term $\mathrm{Im}[\mathrm{G}(\mathrm{r}_D, \mathrm{r}_D, \omega)]$, with both donor and acceptor experiencing the same Purcell effect. For inhomogeneous environments with LDOS values rapidly changing over the donor-acceptor distances, further terms of this Taylor expansion would be needed to accurately describe the problem, leading to terms depending on spatial derivatives (gradients) of the LDOS. These higher order terms become more important with increasing distance between donor and acceptor. In our particular case of a waveguide mediated energy transfer, deviations from $\xi = P$ start occurring for donor-acceptor distances of ~ 10 nm. Deviation for similar distances have been found in recent experimental studies of plasmonic nano-apertures[74]. As shown in Fig.3.5, at even longer

distances ($R > 100$ nm) $\xi(r_D, r_A)$ presents an even larger increase. The waveguide in our calculations sustains a propagating mode, therefore the enhancement parameter $\xi(r_D, r_A)$ is expected to increase quadratically with distance as the energy transfer saturates, because the transfer rate in vacuum decreases as R^{-2}. The modulations of $\xi(r_D, r_A)$ are due to interference of the light coupled into the waveguide, similar to what was described in Fig.3.2[a].

- Interaction between donor and acceptor for the hybrid photonic structure (Fig.3.5[a]):
  - In this case, the energy transfer enhancement at a donor-acceptor distance of 1 μm is increased by 6 orders of magnitude for dipoles orientated along the long axis of the antennas (blue diamonds) when compared to the waveguide-only case. For dipole orientations transversal to the long antenna axis, there is a $\sim$ 10-fold decrease of the energy transfer at the same distance (1 μm), as compared to the waveguide-only case. This decrease is due to the near-field mismatch between the longitudinal dipolar field of the optical antenna and that of the emitter, which is oriented perpendicular to the antenna; this mismatch can be easily compensated by changing the position of the dipoles.

3.8 Conclusions

Energy transfer between two optical emitters is a physical phenomenon with broad applications: from fluorescence microscopy techniques to quantum information protocols. In this chapter I have introduced a numerical method to quantify energy transfer rates in arbitrarily complex nanophotonic environments. Numerical errors of the method were quantified against analytical results and can be reduced by increasing computational resources. Based on the numerical method, we proposed a hybrid optical circuit for long-range energy transfer, in which donor and acceptor are coupled to metallic antennas linked by a dielectric waveguide. We report $2 \cdot 10^{-6}$ absolute energy transfer to donor decay rate at distances comparable to the wavelength of transmitted photons, an increase of 6 orders of magnitude per emitted photon

(and over 8 orders of magnitude overall when accounting Purcell enhancements at the donor position) against the vacuum case at a distance of $1\mu m$. I concluded the chapter contributing to the ongoing debate on the role the LDOS on the description of energy transfer and generalizing the interpretation to distances comparable to the wavelength of the transferred photons.

4

Non-linear effects in nanoantennas with deeply subwavelength features

Previous chapters dealt with linear interactions between nanoantennas and optical emitters. We have discussed that when the shape of these nanoantennas is tuned to their localized surface plasmon resonance (LSPR) their linear response to optical fields is enhanced. As the intensity of optical fields increase, interactions cease to be properly described in a linearly, and nonlinear effects become more important.

Noble metals present nonlinear susceptibilities comparable or larger than commonly used dielectrics and semiconductor crystals employed in nonlinear optical applications[84]. However, the use of metals as materials for non-linear optics is limited for several reasons. Firstly, metals are opaque at optical frequencies, which hampers the use of phase matching techniques to achieve highly efficient frequency-conversion of optical fields. Secondly, metals are centrosymmetric materials, which suppresses non-linear effects of even-order in the Taylor expansion, when in the common dipole-approximation only transversal fields are considered[85].

These limitations are overcome when tailoring the shape of metals in the form of small particles of the order of the wavelength of the electromagnetic fields interacting with them. Firstly, light generated in the nanoantennas can be radiated without being absorbed. Secondly, discontinuity between the metallic and its surrounding relaxes the centrosymmetric condition by allowing certain dipole-allowed contributions[86]. Additionally, nanoantennas presenting a LSPR enhance the intensity of near-fields in their surroundings. Since nonlinear effects, such as second harmonic generation (SHG), are described by products of electric fields (E) (e.g. $E \cdot E$)[87] the total nonlinear signals benefit from this increase of the near-fields.

For these reasons, nonlinear effects mediated by nanoantennas have been explored in a number variety of shape variations. From colloids[88,89,90,91,92] to nanofabricated structures[93,94,95,96,97].

Even particles with non-centrosymmetric shapes had been studied, which allow sources of nonlinear polarizability to radiate more efficiently into the far-field[98,99,100,101].

In this chapter I explore the nonlinear response of nanoantennas presenting deep-subwavelength features. I start by presenting a model to numerically calculate second harmonic generation (SHG) response of nanoantennas of different shapes using the FDTD method. I then experimentally measure the SHG response of rod shape antennas of varying length. Their SHG signals are compared to equivalent nanoantennas presenting deep-subwavelength features. As the local-fields are focused to smaller volumes we can expect the local fields to be further increased when compared to rod shape antennas, thus enhancing the nonlinear response. Their increased response is found to be in line with the model introduced at the beginning of the chapter.

4.1 Model of SHG: volume and surface contributions

SHG is a process in which two-photons of an incident field at a frequency ω interact with a nonlinear medium and combine to generate one photon at twice the original frequency. When considering macroscopic proceses it can be describe by the equation:

$$\mathrm{E}(2\omega) = \chi^{(2)}\mathrm{E}(\omega)\mathrm{E}(\omega) \tag{4.1}$$

where $\chi^{(2)}$ nonlinear susceptibility tensor and acts as proportionality factor. To extract a measurable signal, critical phase matching needs to be present such that the signal build up in the macroscopic media.

The description of SHG in the presence of nanoantennas is slightly more feature-rich. We follow the theory described by Reichenbach et al.[102]. I start considering SHG from single rod-shaped particles excited by a laser field. The incident electric field induces a dipole moment in the metallic particles both at the fundamental, as well as at twice the frequency of the incoming light field acting as the source of SHG. Although we are dealing with centrosymmetric materials, a dipole-allowed contribution to SHG will radiate: electrons located at the metal surface experience broken symmetry due to the different electric fields at the interface. These local field contributions to SHG can be divided between surface and volume (or bulk). The surface contributions can be further divided in parallel and perpendicular to the interface:

$$\begin{aligned} \Pi_\perp &= \chi^{(2)}_{\perp\perp\perp} E_\perp E_\perp \mathrm{e}_\perp \\ \Pi_\parallel &= \chi^{(2)}_{\parallel\perp\parallel} E_\perp E_\parallel \mathrm{e}_\parallel \end{aligned} \tag{4.2}$$

where, for a fixed frequency, χ_{ijk} represents components of the effective second order susceptibility tensor of a particular material and E_i the local electromagnetic field at the particles surface.

At the same time, a plane wave traveling through an isotropic centrosymmetric medium induces a longitudinal source of polarization in the *bulk* of the material. This non-local source of polarization is due to strongly varying fields within the material and can be shown to be analogous to higher-multipole contributions to the SHG polarizability[103,104,105,106]. We express the bulk contribution as:

$$\Pi_{bulk} = \frac{1}{2ik}\chi^{(2)}_{bulk}\nabla[\mathrm{E}\cdot\mathrm{E}] \tag{4.3}$$

with k representing the wave vector of an incoming field E with angular frequency ω, and $\chi^{(2)}_{bulk}$ is bulk component of the second order susceptibility tensor. In perspective with previous reports on SHG response from metallic objects, we note that our bulk contribution contains both the so-called pure-bulk contributions, as well as contributions which can be mapped into surface contributions[107].

We also assume $\chi^{(2)}_{bulk}$ to be two order of magnitude smaller than $\chi^{(2)}_{\perp\perp\perp}$ and $\chi^{(2)}_{\parallel\perp\parallel}$ in line with previous reports[108]. This gradient is typically negligibly small for spherical particles with $l \ll \lambda$ but can increase significantly for larger elongated objects such as NRs and more complex structures[109].

4.2 Numerical simulations of SHG mediated by nanorod antennas

In our numerical analysis I evaluate the local electric fields using a finite-difference method in time domain (FDTD) electromagnetic solver. A plane wave at a wavelength $\lambda = 800$ nm, and polarized along the long axis of the nanorod (NR) antenna, excites a surface plasmon oscillation (Fig.4.1-a) and generates a SHG response. The particle's total nonlinear response is then given by the integral over all surface and volume contributions. As discussed before, both surface and bulk contributions have the same units, since the inverse wavevector dependence of the bulk contribution cancels the inverse distance dependence introduced by the gradient operation. In this way, all units in the text are arbitrary, but mutually equivalent.

Numerical results of the SHG responses as a function of the NRs length for the different SHG contributions given by Eq.4.2 and Eq.4.3 are shown in Fig.4.1-b. Solid lines represent 50nm-wide NRs whereas dashed-lines correspond to 75nm-wide NRs. We can see that the nonlinear responses increase for the $\lambda/2$ and $3\lambda/2$ resonance conditions. At resonance, the field at the fundamental wavelength is increased as shown in Fig. 4.1c-d. The figure displays both the electric fields and electric field gradients of two NRs with 75 nm and 50 nm widths matching the $\lambda/2$ and $3\lambda/2$ resonances. Different geometries of the NRs affect the nonlinear response of both surface and bulk contributions. Narrower NRs present larger field gradients within its volume which increases the bulk contribution to SHG, and makes them show higher SHG response despite consisting of less material.

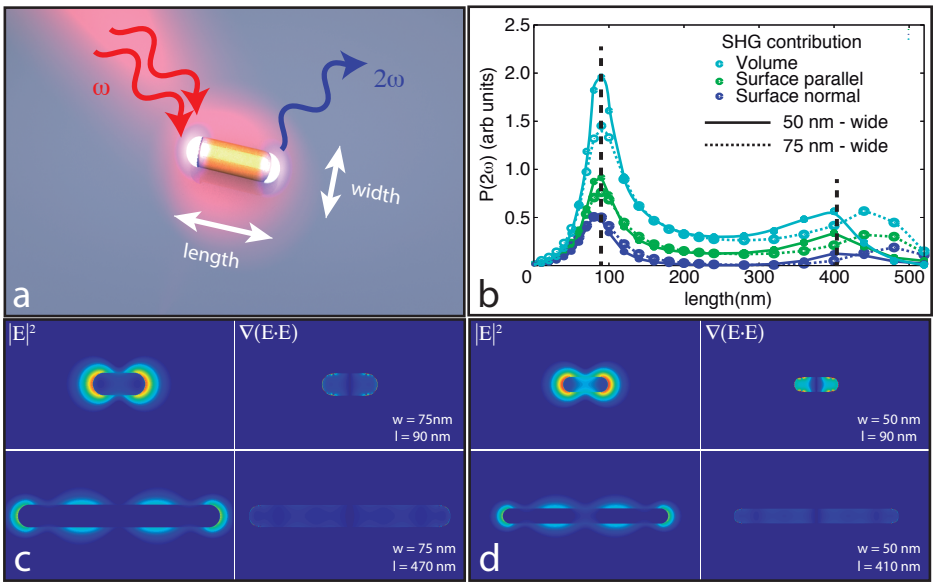

Figure 4.1: SHG dependence on cross section: numerical evaluation of the SHG response of NRs made of gold on a glass substrate. (a) cartoon sketch of gold NR as used for modelling. (b) $\Pi_{\perp}$, $\Pi_{\parallel}$ and Π_{bulk} contributions of NR with different lengths illuminated by $\lambda = 800$ nm. Continuous line represent values for narrower rods of 50 nm, and dashed lines represent values of a 75 nm-wide NRs. Surface and bulk contributions have arbitrary but equivalent units (see main text). The bulk contribution is increased for narrower NRs, especially at the $\lambda/2$ and $3\lambda/2$ resonant conditions (black dashed lines). (c-d): Local field enhancements and field gradients of resonant NRs: 75 nm-width (c) and 50 nm-width (d). The smaller cross section of the NRs in panel (d) causes enhanced fields and gradients inside the NR which results in stronger nonlinear response for the $\lambda/2$-mode.

4.3 Bottlenecks in NR increase SHG response

Bulk contributions can be increased in more complex geometries, for instance by adding a bottleneck along the NR. We achieve this by locally reducing the NR's geometrical cross as depicted in Fig. 4.2-a for a 75-nm-wide NR having a length fulfilling the $3\lambda/2$ resonance condition at 800 nm. Figure 4.2b-c show the volume and surface contributions to the SH response for different bottleneck positions.

NRs presenting a $3\lambda/2$ resonance have a maximum of the longitudinal electric field at its central position as shown in Fig.4.1-c. At this central point, the field gradient is minimal within the metal. We increase the field gradient by introducing a bottleneck in the NR. As shown in in Fig.4.2-c. This central position is the most favorable position for placing the bottleneck since it generates the largest bulk contribution, while also increasing the surface contributions; with both contributions rapidly decreasing for bottlenecks placed off-center.

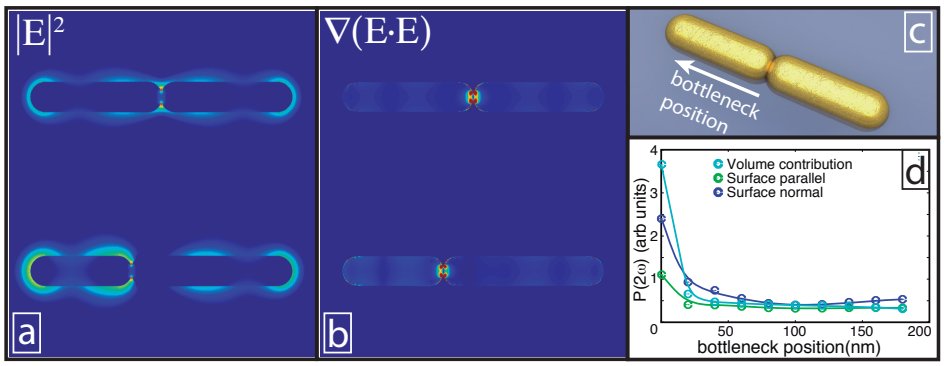

Figure 4.2: Calculated SHG response of NR made of gold presenting a bottleneck. Panel a: cartoon sketch of gold NRs with a bottleneck. Panel (b): Local field enhancements and field gradients of NRs at $3\lambda/2$ resonant condition with a bottleneck at its central position (top) and displaced 120 nm from the centre (bottom). Panel (c): Surface and bulk contributions to the SHG as a function of the bottleneck position for NR at $3\lambda/2$ resonant condition. Units are the same as the ones used in Fig.4.1

Two remarks can be made at this point. First, besides the well known surface contributions to the SH signal generated by nanoparticles, bulk contributions are important and have to be taken into account in nanoparticles due to their antenna-like behavior. Second, the bulk contribution can be maximally exploited by enhancing field gradients inside nano structures.

4.4 Dispersion of the SHG contributions

Our numerical simulations allow not only to understand a particular geometry, but they can be employed to predict the dependence on the fundamental wavelength. The dispersion of the surface and bulk contributions shows distinctly different behavior (Fig.4.3).

The surface contributions are still present for longer NRs having LSPRs in the near-infrared spectral range, whereas the bulk contribution diminishes for resonances at longer wavelengths. This behavior is caused by the dielectric properties of the metal. Since the resonant wavelengths are further away from the Au plasma frequency, they inhibit strong field gradients inside the particle. This effectively screens the inner part from the incident field. As a consequence, bulk contributions can not be neglected for shorter incident field wavelengths. At longer wavelengths the surface contributions will dominate the nonlinear response.

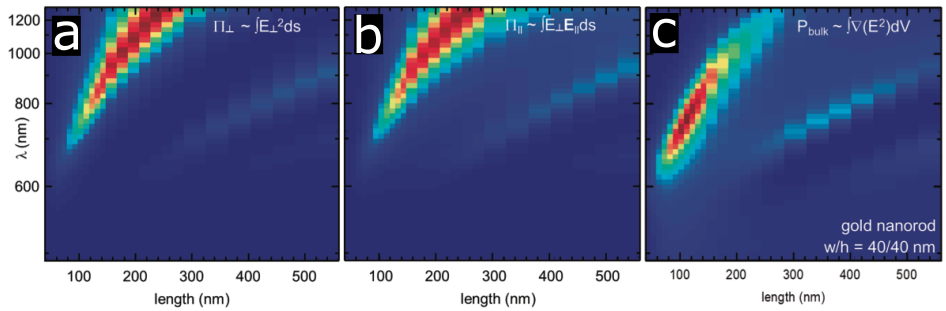

Figure 4.3: Dispersive character of the SHG components in NRs antennas. The surface contributions (a, b) follow the mode dispersion with the NR length resulting in strong contribution at NIR-wavelengths. (c) The bulk contribution originating from the intensity gradient inside the NR is strongest in the visible spectral range.

4.5 Experimental SHG signal of NR antennas

To verify our theoretical findings, we measured the SHG response of NR antennas similar to those described in Fig.4.1. We fabricated matrices of NR antennas made of Au using standard electron beam lithography techniques. A typical NR antenna is shown in the inset to Fig.4.4.

Experiments were performed using an Octavius Ti:Saph laser, which was sent through a microscope objective (NA=1.4). The excitation laser was filtered by a 10-nm-wide dielectric bandpass filter centered at 800 nm. It delivers $\leq$ 250 fs pulses at 85 MHz repetition rate with an average power of 125μW at the focal volume. We collect the SHG signals generated by the nanoantennas through the same objective. The SHG signal is filtered from reflected and scattered light at the excitation wavelength by set of dielectric short pass filters. The generated SHG signal is sent to an avalanche photodiode in single photon counting mode (PerkinElmer APQR16). A piezoelectric stage was used to move single particles in the confocal detection volume allowing us to map the nonlinear response from particle sweeps with lengths $l = 80 \cdots 550$ nm as shown in the insets to Fig.4.4.

Fig.4.4 displays the SHG signals for two sets of NRs having a width of 50 nm and 75 nm, respectively. The recorded intensities for each antenna length are summed up from the image and are normalized by the number contributing antennas to average small differences in fabrication. The SHG signal in Fig.4.4 increases for lengths which allow for resonant excitation of the LSPR mode at the fundamental wavelength. These resonance conditions are met for the $\lambda/2$ and the $3\lambda/2$ for antennas of length $\sim$ 120 nm and $\sim$ 430 nm. We see as well an increase in the signal present for antennas having a length matching the λ resonance condition. We attribute this to the inhomogeneous illumination of the NR with our tightly focused excitation beam, which can excite even-modes. This even-mode excitation situation is in contrast to our numerical calculations performed assuming a plane wave excitation that

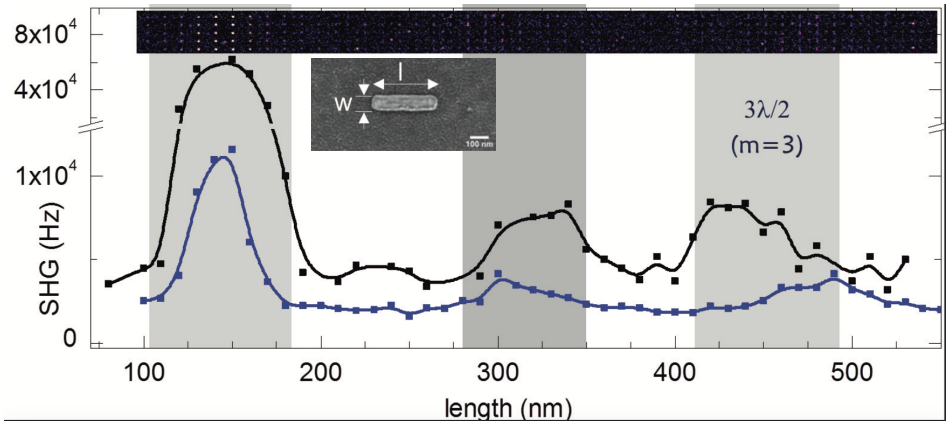

Figure 4.4: SHG signal generated by NR antennas of width 50 nm and 75 nm and varying length. Top inset shows single antenna NLO responses on an array of antennas with increasing length using the scanning confocal microscope described in the text. Signals are integrated over several equivalent antennas to produce the main figure, smoothing signal differences due to fabrication.

cannot excite even-modes due to symmetry considerations. Furthermore, we see that NR antennas of smaller width (50 nm black lines) generate more nonlinear signal than wider ones (75 nm blue lines). This increase, up to a factor 4 in the SHG signal for the $\lambda/2$ resonant case, coincides with the predictions of the model presented in this chapter.

To finalize with the NR results, we note that NR oriented perpendicularly to the laser polarization were also present in the NR sweeps. No appreciable change of SHG/TPPL was observed for the different lengths, indicative of absence of resonance along that particular direction.

4.6 Experimental validation of the bottleneck effect

In this section I will present experimental validation of the previously introduced concept of engineering the intensity gradients of our nanostructures. This is done by placing bottlenecks at locations of high current density.

Before, let us remark that fabricating indentations along NR is a challenging task, since one would need to use nanofabrication techniques with position accuracy and feature size precision of better than 10 nm. Trials to mill our nanostructures using a focused beam of Ga^+ ions were unsatisfactory. First, the feature size of the machine is $\sim$ 20 nm, not sufficient for our purposes. Second, fabricating a full array of particles is a time consuming task (more than 8 hours for matrices studied in this paper).

We then opted for electron beam lithography (EBL) and fabricated two separated NRs

terminated by spheres as sketched in the inset of Fig.??. In this nano bottlenecked antenna (NBA) configuration, we can vary the separation between two dumbbells until they just touch. Hence, we are only limited by position accuracy of the EBL machine and the resist's minimal resolution (typically 5 nm).

We must ensure that these NBA structures do not present significantly different resonances from that of the NR ones, so a direct comparison can be made. We measured the linear extinction of the structures using white light from a halogen lamp and a low NA objective (NA $\leq$ 0.05) onto a matrix of equally fabricated nanoparticles. The matrices are made of repetitions of particles separated 1x1 μm^2 for particles shorter than $l \leq$ 640 nm, and separated $2 \times 0.5\,\mu m^2$ for longer particles. This ensures there is no coupling between the nanoantennas.

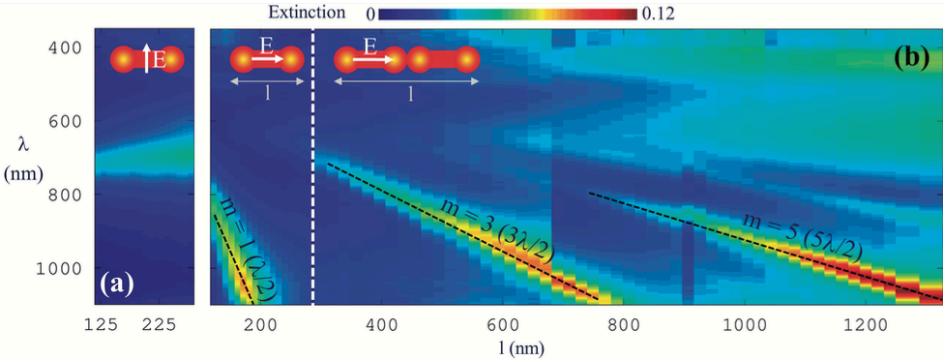

Figure 4.5: Far-field extinction measured at matrices of nanostructures reveals the odd-mode resonances only. The length of the nanostructures is varied between consecutive measurements in steps of 10 nm (NDB) or 20 nm (NBA), respectively. (a) Extinction of NDB arrays for light polarized along the short axis of the nano structures. (b) Extinction coefficients for light polarized along the long axis of the nanostructures. Lengths between 100 nm and 300 nm show the result for NDB structures, while lengths between 300 nm and 1400 nm correspond to the NBA structures.

Fig.4.5a shows extinction values of single nano-dumbbells (NDBs) for transversally polarized light (along the short axis of NDB) for matrices of NDBs having a length between 120 nm and 300 nm, varying in steps of 10 nm. In the transversal case, we see no spectral shift of the LSPR, and only a monotonic increase with length. From this results, we do not expect our structures to present transversal resonances at either the fundamental laser wavelength (λ = 800 nm) or at the SHG wavelength (λ = 400 nm). The longitudinal case displayed in Fig.4.5b, corresponds to an incident electric field aligned along the long particle axis and the extinction shows pronounced resonances which are very similar to the case of NRs. The impossibility to further reduce the overall structure length while maintaining the dumbbell shape at the ends sets limits to the lower range of NBA's length.

Nonlinear measurements of NRs, NDBs and NBAs were performed using the same experimental conditions used for measuring NRs (Fig.4.6). The nonlinear response of NDBs

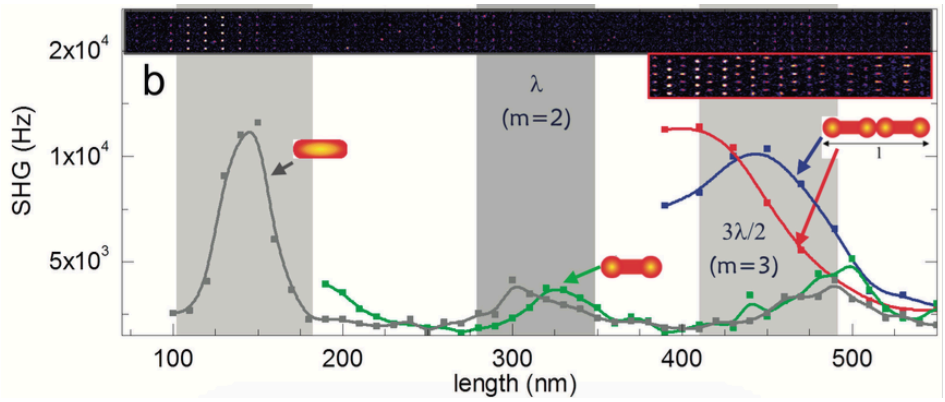

Figure 4.6: Comparison of the SHG signal generated by matrices of nanoantennas of different shapes (NR, NDB and NBA) and varying length. NBA antennas presenting bottlenecks tuned to their $3\lambda/2$ resonance show enhanced SHG response when compared to equivalent nanoantennas tunned to an equivalent resonance.

(green curve) is analogous to the one of NRs (grey curve), apart from a shift in length due to the extra spherical termination at the end of the NDBs. This equivalent behavior takes place both, for the SHG and the TPPL responses. Contrary, NBAs presenting $3\lambda/2$ resonances in the range $l = 400 \ldots 450$ nm show enhanced nonlinear response. The red and blue lines in Fig.4.6 show NBAs structures of different width and with different bottleneck diameter sections. As mentioned before, changing the fabrication parameters allows us to fine tune the width as well as the separation between antenna parts in NBAs, and thus the bottleneck diameters. Due to the different width and bottleneck diameter of the NBAs shown in red and blue, the lengths satisfying the $3\lambda/2$ resonance condition are slightly shifted. We attribute this to different length indexing and to the different effective refractive indices of the NRs modes for different diameters. The nonlinear signals in NBAs are enhanced by a factor 2-3, reaching counting rates comparable to the case of NRs tuned to its dipolar resonance. We also note that, although small, there is a statistically significant increase in the nonlinear response from NBAs with narrower bottlenecks, consistent with the model presented in this paper.

4.7 Conclusions

I presented how to model the SHG nonlinear response of nanoantennas using FDTD method, with both surface and volume (or bulk) contributions taken into account. Using this method we are able to show how introducing bottlenecks in resonant nanoantennas increases their SHG response. These bottle necks need to be present at points of maximum near-fields. I then experimentally validated our numerical results in Au nanoantennas tunned to their

$3\lambda/2$ resonance. The bottleneck increases the SHG response by a factor 2. This increase is partially attributed an enhanced SHG bulk contribution, which is generally overlooked. This concept of increasing nonlinear optical bulk contribution by tailoring intensity gradients in nanostructures can readily be applied and opens up new flexibility in tailoring the nonlinear response.

5

Closed-loop coherent control of single quantum dots

Time and spectral phase. Previous chapters deal with the control of optical fields in space and their interaction with matter, both linearly (Chapters 2 and 3) and nonlinearly (Chapter 4). In this chapter we turn our attention to the control of optical fields in time, and how the interference of the different spectral phases of an excitation laser can maximize the excitation probability of optical emitters.

Coherent control actively manipulates the transition probability between two states in quantum systems driven by laser fields with customized spectral phases. This technique provides spectroscopic information about the dynamics of quantum systems unreachable using conventional techniques[110,111]. Boosted by the progress in broadband femtosecond laser technology and pulse shaping (the technique to control the time and spectral phase properties of the pulse), coherent control has been demonstrated over a wide range of experimental applications: from the study of coherences in atoms, molecules, quantum dots (QDs) and plasmonic systems[112,113,114,115,116,117,118], to the manipulation of chemical reactions[119,120], and the maximization and control of non-linear light-matter interactions[121,122,123].

For complex systems like emitters in the solid state at room temperature, a priori calculations of the optimal solution, i.e. the best laser pulse for inducing a certain desired effect, cannot be calculated from the systems Hamiltonian using quantum optimal control theory[124,125]. Instead, following the seminal paper by Judson and Rabitz[126], the preferred approach for coherent control experiments in complex environments has been to adapt the spectral phase of a broadband laser pulse to the systems under study, by using an adaptive closed-loop feedback optimization. In this latter case, a specific experimental observable (e.g. one-photon or multi-photon induced fluorescence in molecules or SHG in crystals) guides a learning algo-

rithm that varies the spectral phase and time profile of the laser pulses. This approach was successfully applied to many different systems[112,115,119,122,127,128,129], yet its fundamental limits of signal to noise and stability so far remained unexplored.

As one moves from ensemble measurements to the investigation of single systems, the observable signal reduces dramatically to the single photon level. To overcome this difficulty one needs to increase the integration time for every step in the optimization process, even when using avalanche detectors. This practically extends the experimental time prohibitively. Furthermore, the signal from faint emitters is intrinsically unstable over time, since the shot-noise can be of the order of few percents for ideal single quantum emitters[130]. Additionally, quantum emitters like molecules and QDs at room temperature are known to undergo photoinduced processes such as blinking and photobleaching[131]. These constraints make practical implementation of closed loop control schemes burdensome.

I this chapter I show that it is possible to use the two-photon induced photoluminescence (TPPL) from single QDs at room temperature as a feedback variable for a closed loop phase control experiment. The chapter starts by describing the QDs used in the experiment. It then continues by briefly describing the phase-shaping experimental set-up. Maximization of the TPPL is achieved by optimizing the two-photon absorption (TPA) process and monitoring the TPPL from the excited state on single QDs. The algorithm performing the optimization is then described. Our MODS algorithm converges faster than brute force approaches without prior knowledge of the optimization landscape. We then compare the found solutions to the standard MIPS algorithm which typically used in phase shaping experiments.

5.1 Rod-in-rod quantum dots

The first ingredient for our experiment are robust emitters that allow us to push the sensitivity of our optimization algorithm to the single QD level. For this reason we chose colloidal CdSe/CdS core/shell (QDs). They are characterized by a 4.8x15 nm CdSe core rod embedded in a CdS shell that yields an overall QD size of 9.8 nm by 44 nm.

Due to the large volume of the CdS shell, they are known to be very efficient two-photon absorbers[132,133,134], a condition ideal for our efforts. In these systems, the total volume determines the cross section for TPA and is mostly given by the CdS shell volume. The exciton confinement determining their emission spectrum, can be tuned independently by changing the dimensions of the CdSe core. Our QDs have an absorption spectrum that is dominated by the CdS shell absorption with a cutoff at 515 nm, and a Stokes shifted luminescence emission centered at 670nm.

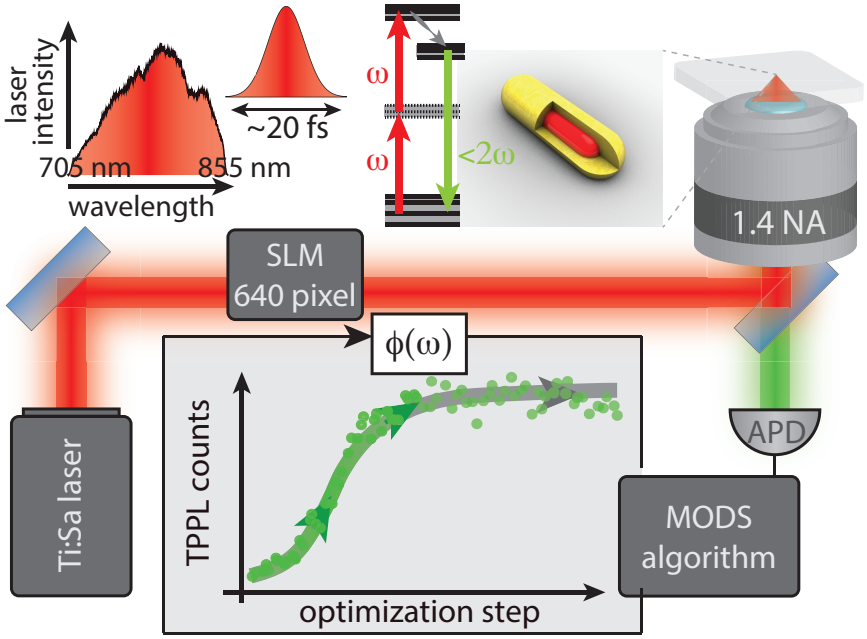

Figure 5.1: Schematic of the experiment. Laser pulses from a broadband femtosecond laser induce TPA in rod-shaped CdSe/CdS QDs, after passing through a phase-only pulse shaper. TPPL signal collected using an oil-immersion objective is spectrally filtered and sent to an APD. Light emitted by QDs shows non-classical character, demonstrated by photon antibunching. For each optimization step, the MODS optimization algorithm searches for the spectral phase on the SLM pixels that maximizes the TPPL signal using it as feedback variable.

5.2 Experimental set-up

A schematic of the experimental procedure is shown in Fig.5.1. In short, a femtosecond broadband-laser pulse enters a phase-only (no spectral intensity modulation) pulse shaper. Inside the pulse shaper, a spatial light modulator (SLM) controls the spectral phase components of the laser pulse. The laser beam is then sent through an oil-immersion microscope objective where it gets focused on the sample plane inducing TPA in the QDs. Propagation through lenses introduces chromatic dispersion, which limits the temporal duration of our laser pulses if not compensated. Our laser pulses are 20 fs-long when transform-limited.

After excitation, the QDs emit TPPL which is collected through the same microscope objective. We detected this signal with avalanche photodiodes (APD) after spectrally filtering the signal form the excitation laser. The MODS algorithm changes the spectral phase on the SLM pixels. Each pixel in the SLM corresponds to different wavelength components. The algorithm searches for the phase mask that maximizes the TPPL signal used as the feedback variable.

Essentially, the algorithm searches for the best-suited spectral phase, and hence the time profile of the laser pulse, that maximizes the TPPL.

5.3 Optimization of the TPPL signal of single QDs

In this section I present our main result, shows the realization of a phase-only-controlled closed loop optimization of the TPPL emitted by single QDs at room temperature (Fig.5.2-c)

To perform such optimization, we make first a confocal image by raster scanning a PMMA film with embedded QDs while recording the TTPL signal (Fig.5.2-a). The concentration of QDs is brought to a sufficiently low concentration in a PMMA film, so we can spatially resolve isolated bright spots. These spots correspond to either single QDs or clusters with a few QDs.

We perform second order intensity correlation measurements on the bright spots of the confocal image. A beam splitter splits the signal equally between two APDs. We record the arrival time of each photon and use this information to construct an intensity correlation measurement. We ensure that we are dealing with single quantum emitters by looking at the dip at zero time delay. The dip at zero time-delay in Fig.5.2-b is known as photon antibunching and is characteristic of quantum emitters that (on average) emit at most only one photon per excitation pulse.

We note that second order photon autocorrelation traces were not corrected for accidental coincidences arising from detector dark counts, neither for the presence of biexcitons in QDs. Thick-shell QDs, like the ones we used, present high biexciton photoluminescence quantum yields. This has the effect of increasing the normalized coincidences at zero-time delay up to $1/2$ for high excitation powers, as the ones used in these experiments[135,136].

After selecting suitable QDs behaving as single emitters, the MODS optimization algorithm (explained below) performs TPPL optimization on the chosen QDs. Optimization routines are presented in Fig.5.2-c. We can see the TPPL optimization runs for three different QDs. The figure contains the signals obtained at each step of the optimization algorithm. As the phase on the SLM is varied in a deterministic way, the TPPL increases until reaching a maximum. For all the investigated QDs, and after two cycles of the optimization routine, the TPPL increased by a factor between 4 and 6.

This demonstrates that it is possible to perform closed loop coherent control optimization experiments even on single QDs at room temperature, pushing this technique to its limits of sensitivity.

The success of the experiment is due to three important factors. First, the microscopy setup is maximized for detection of single molecules radiating at the single photon level[116], therefore allowing to easily detect light from single quantum emitters. Second, we used QDs

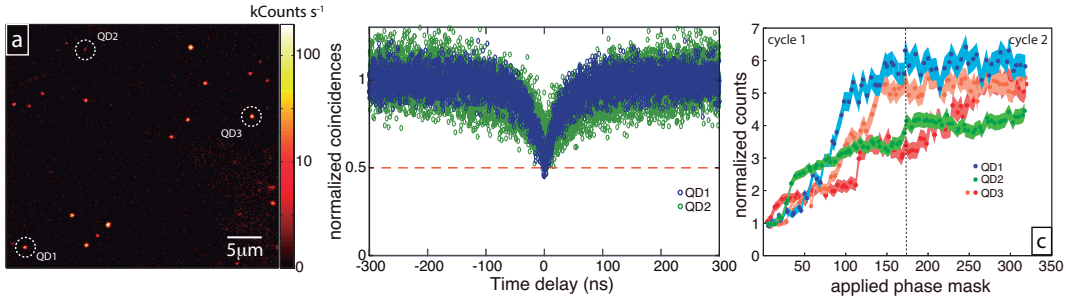

Figure 5.2: (a) TPPL confocal image of the sample the QDs sample. Isolated bright spots corresponding to TPPL emitted by individual QDs is clearly resolved. (b) Second order intensity correlation function showing photon anti-bunching. The non-classical characteristics of the photon statistics confirms that the experiment is carried out on single quantum emitters. (c) Closed-loop optimization of the TPPL signal emitted from designated single QDs.

characterized by very high quantum yields and considerable stability even at room temperature. Blinking and bleaching events are almost absent, even after hours of continuous excitation, with the only the downside of a decrease of the total amount of detected signal over time under continuous excitation of the QDs. This can be explained by minor photo-damage of the QDs together with the fact that it is almost impossible to maintain a single QD precisely in the focus of the microscope objective for a very long time, due to slight drift of the sample. Third, given these difficulties, we need a fast-acting algorithm for the maximization to be effective.

5.4 MODS Optimization Algorithm

In general, the objective of experimental closed-loop coherent control experiments is to find the optimal set of control 'knob' variables that maximize the signal of a particular observable of the system under study. In our particular case, our control variables are the spectral phases of a broadband femtosecond laser pulse, and the observable is the TPPL signal of the QDs.

Non-resonant multiphoton transitions involve many routes through a continuum of virtual levels. The interference conditions of the multiple frequency components of the control pulse can enhance or diminish the total transition probability. Therefore, the interference effect depends on the spectral phase distribution of the laser pulse.

We remark that we are dealing with QDs that emit discrete number of photons. Their intrinsic signal to noise ratio is of the order of 1% (SNR $\sim N/\sqrt{N}$). Additional noise comes from the drift of laser power over time, also of the order of few per cents. For our algorithm to optimize, different trials of control variable sets need to generate output observables whose difference is bigger than the intrinsic measurement noise of the quantum system under study.

Our femtosecond-laser pulse shaper incorporates a SLM with 640 pixels (control dimen-

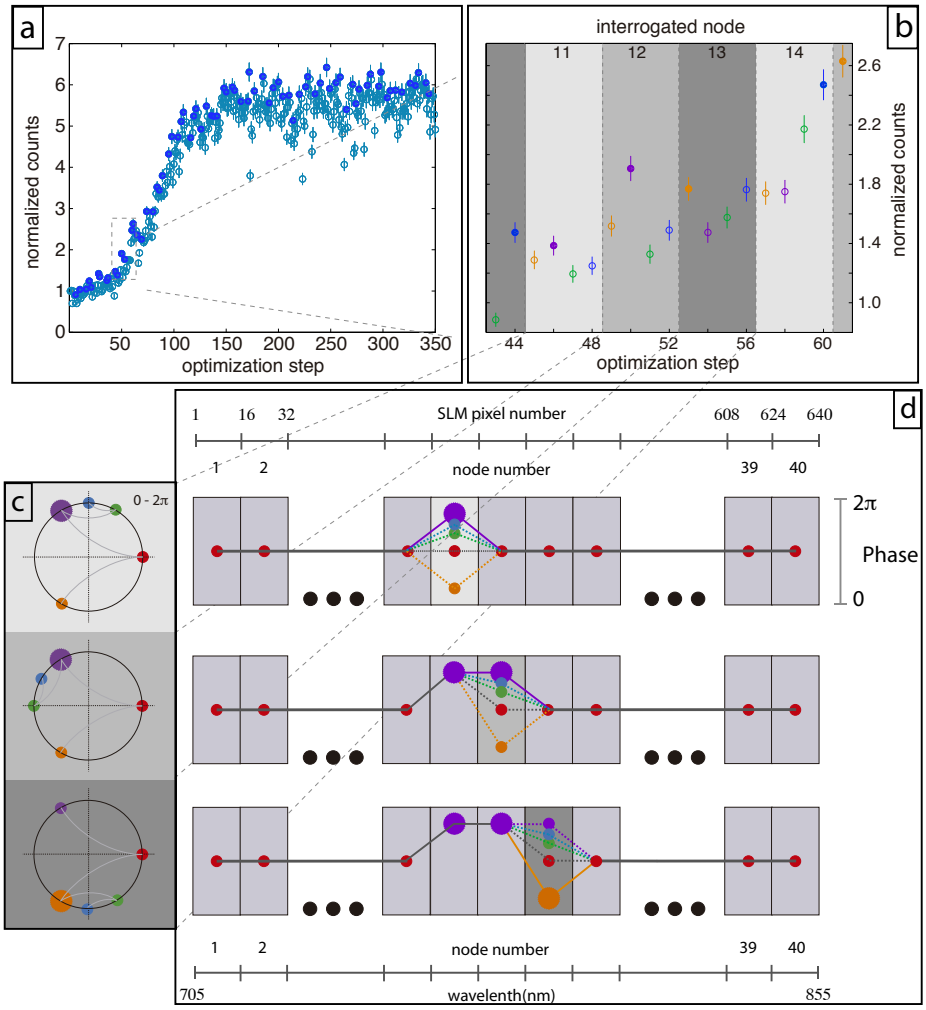

Figure 5.3: Schematic of the optimization algorithm. (a) Trace of TPPL signal (observable) evolution in a typical deterministic closed-loop optimization run on a single quantum emitter. Full symbols represent optima for each individual interrogated node, with empty symbols representing discarded phase masks. (b) Close up look of the optimization trace, with observable output color codes to fit the applied phases (c) at each particular node. (d) Represents the total phase mask at each run of the optimization algorithm.

sion), with 4096 (12 bit) different phase delay values at each pixel. It is obvious that performing a brute-force global search over such a vast solution landscape is unrealistic, due to the long time required to perform such an experiment and the constraints of our particular QDs sample. We thus proceed by reducing the control variable dimensionality and by using an efficient search algorithm.

In order to reduce the total amount of control variables, we group together several SLM pixels into control nodes (40 nodes in the experiment presented in Fig.5.3). We then apply interpolation in the complex plane adjacent nodes to obtain a phase mask trial. Despite this big reduction of the control variable domain the optimization is still non trivial. The traditional way to perform the optimization is to employ evolutionary strategies or genetic algorithms. Even though these approaches are robust to noise, they are based on stochastic methods and typically need thousands of trials to find a global optimum. Instead, the MODS algorithm exploits the properties of quantum control landscapes, capitalizing on the absence of local traps in the control landscapes and the existence of multiple global optima, to implement a fast deterministic search [111,137,138].

Furthermore, since we are shaping the temporal profile of the laser pulse in the frequency domain, MODS exploits the fact that individual frequency components affect the overall laser pulse, allowing the decomposition of the optimization process in one-dimensional searches. For each node we search the phase in the 0-2π domain that maximizes the TPPL signal while keeping the rest of the nodes fixed. This exploits the equivalence of phase masks under phase wrapping transfomations. On each node search, we perform a progressive segmentation of the phase space. We start with an equally spaced trisection of the phase space for each particular node. Based on the TPPL observable signal for the three applied phase masks, we can select the phase interval that produces highest signal. We further bisect this phase segment comparing the outcomes of the observable (Fig.5.3-c). This refinement procedure can be iteratively applied at discretion in each node.

In practice we make two refinement measurements at each node, since the intrinsic observable noise prevents us from finding arbitrarily refined solutions (Fig.5.3-a). Once the optimum phase value for a node has been found, we fix its phase value in the mask and repeat the same procedure in the next node (Fig.5.3-d). Fig.5.3-a shows a particular full optimization experiment, with solid symbols in the normalized count representing maximum values for a particular node optimization. A zoom-in into the optimization trace (Fig.3-b) shows consecutive interrogated nodes and signal values within them, corresponding to the particular phase mask configuration (Fig.5.3-bottom-right).

We have shown that our optimization algorithm is capable of finding the spectral phase, i.e. the time profile of the laser pulse that optimizes TPA in single QDs. The algorithm starts with an initial phase mask on the SLM and produces a final phase mask that optimizes the TPA. Looking at the difference between initial and final phases we can get more insight both on the way the algorithm operates and the way the TPA process works in QDs. Such phase difference, in the case of the experiments illustrated in Fig.5.2-c, is plotted as a blue curve (called the Algorithm Phase) in Fig.5.4-a.

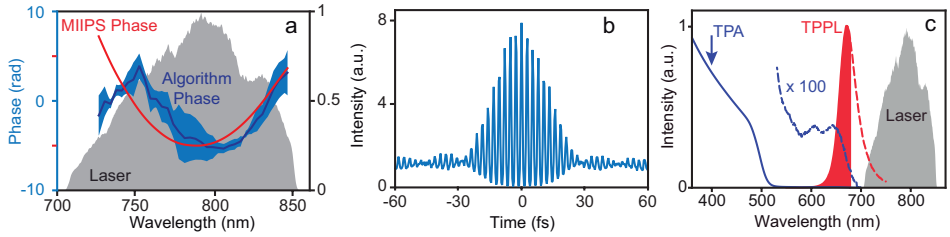

Figure 5.4: (a) Laser spectrum (shaded grey curve), initial spectral phase measured with MIIPS (red curve) and the inverse phase mask obtained with the closed loop optimization on QDs (blue curve). The light blue shaded region represents the uncertainty on the determination of the phase mask, corresponding to the standard deviation calculated repeating the maximization process several times. (b) Autocorrelation of the final laser pulse, corresponding to a pulse duration of 20fs. (c) Laser spectrum (shaded grey curve), absorption (blue solid curve) and TPPL (red curve) spectrum of the QDs. The red coloured region is the portion of the TPPL we detected in the experiment using a 680nm short pass filter to block the laser. The blue dashed curve is the magnified (100x) absorption spectrum in the 700nm range.

The light blue colored region represents the standard deviation obtained over several repetitions of the same experiment on different QDs. It is evident that the obtained Algorithm Phase has a well-defined shape. Understanding this shape is at the basis of every coherent control experiment. In order to do that we separately measured the initial spectral phase of the laser pulse with the multiphoton intrapulse interference phase scan (MIIPS) using SHG from small nano-particles[139], shown as a red curve in Fig.5.4-b. This curve represents the spectral phase of the laser pulse when the phase mask on the SLM is applied. The red and the blue curves present a clear similarity, which tells us that the algorithm is mainly trying to correct for the initial phase distortions of the laser pulse. As previously described[140], a non flat spectral phase, as the red curve of Fig.5.4-b, corresponds to a distorted pulse, which is not the shortest possible for the laser spectrum plotted as a grey coloured region, i.e. it is not a transform-limited (TL) pulse.

The optimization can therefore be thought as follows: the starting phase mask on the SLM produces a distorted pulse characterized by the spectral phase plotted as a red curve in Fig.5.4-a. After two cycles of the closed loop optimization, the TPPL from single QDs is increased

by a factor of 6 and a final phase mask is applied onto the SLM. Since the difference between the final and the starting phase masks applied to the SLM looks similar to the initial spectral phase measured with MIIPS, we can conclude that the main effect of the optimization is to compensate for the phase distortions and hence to compress the laser pulse in time at the diffraction limited spot at which the QDs sit. This is confirmed by the pulse autocorrelation reported in Fig.5.4-b, measured with the final phase mask applied on the SLM, which corresponds to a pulse as short as 20fs, close to the TL pulse for the laser spectrum reported in Fig.5.4-c.

5.6 Discussion

To understand why the closed-loop optimization in QDs leads to TL pulses, one needs to consider the absorption spectrum of the QDs at the fundamental laser (around 800nm) as well as at the SHG wavelength (around 400nm). Such absorption spectrum is plotted in Fig.4c (solid blue curve) together with the laser spectrum (grey coloured region) and the TPPL spectrum (red curve). The blue arrow at 400nm indicates the spectral region where the TPA takes place, whereas the coloured red region in the TPPL spectrum represents the amount of TPPL that we effectively detected (a short pulse spectral filter at 680nm was used to cut the laser light). The absorption spectrum is dominated by the CdS absorption, having an onset around 515nm and growing bigger for smaller wavelengths. The blue dashed line shows a zoom (100x) of the absorption spectrum near 700nm. As one can see there is no overlap between the laser spectrum and the tail of the QDs absorption, meaning that the fundamental laser cannot induce any single photon transition in these systems. Therefore, only pure two-photon transitions at 400nm, not mediated by any real state are possible. Moreover, at the SHG wavelength, the absorption spectrum of the QDs is very broad, and no discrete state is expected to be resolved at room temperature even in a single QD. In other words, the QDs absorb all the wavelengths within the SHG spectrum of the laser with a similar efficiency. For such systems, namely very broad absorbers at the SHG wavelength with no real intermediate state, it can be demonstrated that the TL pulse is the unique solution that maximizes the TPA[141,142].

We can therefore conclude that the performed closed loop phase optimization, even when acting on single quantum emitters producing limited amount of signal and subject to instability, is able to find the right solution that theory predicts for these systems, i.e. the TL pulse. In this way, we can also look at this experiment as a new pulse compression method on a deeply subwavelength spatial scale. In the last few years, there has been a lot of interest in characterizing, controlling and compressing laser pulses with high spatial resolution for microscopy applications[143,144,145,146].

Pulse compression as presented in this chapter has two main advantages compared to the

previous work. First, it does not rely on SHG measurements. Laser wavelengths shorter than 700 nm produce SHG shorter than 350 nm. Refractive components, specially microscope objectives, present considerable absorption at these wavelengths, introducing artifacts. Second, we use excitation powers 20 to 300 times smaller than the ones used for pulse compresssion using single SHG nanoparticles. This laser power is comparable to those reported for previous single molecule experiments[147]. This is favorable for bio-labelling and in vivo imaging experiments[148,149] since the same QDs present in the sample can be used to perform pulse compression.

5.7 Conclusions

In this chapter I presented an optimization algorithm that maximizes the TPPL from single QDs at room temperature. The optimization performs pulse compression at the focal volume of a focused laser beam. In effect, we are controlling the time profile of laser pulses at the focal spot of tighly focused laser beams.

Our findings demonstrate that closed loop phase control experiments are not only limited to ensembles, but may be applied under the appropriate experimental conditions, to single quantum emitters.

6

A plasmonic quantum eraser experiment

Photons playing the quantum version of *hide and seek*. The control of optical quantum states by nanometre-sized structures, in particular plasmon-supporting metallic structures, is a current active field of research. As shown in the previous chapters, metallic particles of carefully tuned dimensions can act as antenna equivalents at optical frequencies, controlling both near and far-fields. I in the present chapter extend this ability to control quantum bipartite photon states entangled in polarization. Correlations between the two parties in these kind of states cannot be explained by using any kind of classical state belonging to a whole class of locally-realistic theories[150,151]. In particular I will present a nanophotonic version of the *quantum eraser experiment* in the Young's double slit configuration.

Perhaps the most fundamental quantum state is that of a single-mode Fock state with occupation of one photon $|n_k\rangle = |1_k\rangle$. This state describes the state of the electromagnetic field after emission of a photon by an ideal excited two-level system (TLS), and produces the characteristic antibunching behavior introduced in chapter 2. Spatial control of the propagation of these non-classical photon states on the nanoscale was demonstrated by Akimov et al.[152]. In their paper, the light emitted by a single artificial atom (quantum dot) was coupled to a metallic nanowire. Single photons polarize the free electron cloud of the metal, generating a coherent oscillation (plasmon). The paper demonstrated that the single photon character was maintained after coupling with the intermediate plasmonic state by measuring the second-order autocorrelation function of the light uncoupled at the ends of the nanowire. Further studies by Kolesov et al.[153] showed that light out-coupled at two ends of a nanowire coming from single photon excitations of the electron wave (a.k.a. single plasmons) presented interference. This property is analogous to the wave-particle duality of single quantum mechanical entities, the subtlety being that single photon excitations are encoded in collective electron oscillations for some time, then subject to dephasing, while yet maintaining quantum

mechanical character. Direct electrical detection of single plasmons has as well been reported. First, using traditional semiconductor germanium detectors by Falk et al[154], and shortly after using superconducting detectors by Heeres et al.[155], the alternative would be direct electrical detection of plasmon-plasmon interference.

Interference between two indistinguishable photons at the nanophotonic equivalent of a 50:50 beam splitter has as well been reported. In a different paper by Heeres et al.[156], Hong-Ou-Mandel interference of two plasmons excited using the output of an heralded photon source based on spontaneous parametric down-conversion (SPDC) was demonstrated. Remarkably, the 'clicks' (plasmon/photons) at the two outputs of the plasmonic-circuit equivalent of a beam splitter were detected using superconducting detectors attached to metallic transmission lines, before correlations between them were calculated using external electronic circuitry. Later on, the same effect was independently confirmed by Fakonas et al.[157], achieving higher visibility values of the two photon interference. This was done at the expense of shortening the length of the plasmon-supporting transmission line. In other words, single photons were coupled to integrated polymer waveguides, and later interfered at integrated 50:50 splitters composed of both polymer and metals. Arguably, only at the beam splitters the plasmonic character of the single photon excitations was present, thus presenting less overall losses and increasing the visibility of the interference.

Both polarization and time-bin entangled bipartite photon states have also been coupled to plasmonic structures. Altewischer et al.[158] studied the entanglement properties of maximally entangled Bell states after one of the arms passed through an array of holes made in an optically opaque metallic surface. This kind of hole arrays manifest a phenomenon called *extraordinary optical transmission*. In essence it means that the transmission of light through the structure is higher than what would be expected from the geometrical size of the holes. The reason for this increment in the transmission is attributed to surface plasmons excited by the scattering of incident photons at the holes. The excited plasmon can then *tunnel* to the other face of the metallic film and out-couple, hence increasing the overall observed transmission. In the paper, the entanglement was shown to persist after coupling to plasmonic modes, although the visibility was observed to decrease, especially for certain chosen measurement bases. This decrease in the expected correlations for specific basis sets was later theoretically attributed to the presence of modes coupling the holes, which were acting as polarization projectors, by Moreno et al.[159]. Using energy-time entanglement, Fasel et al.[160] showed that entanglement is robust after passing through similar hole-structures in metals, as well as studying correlation after propagation through long metallic ribbons. This is due to the absence of projector-like modes for energy-time entanglement in the structures, confirming the theory above described. Later on, the same group extended the study to cm-long metallic stripes and to single plasmons in temporal superposition states[161]. Further theoretical studies predict that entanglement might be present between coupled plasmonic modes

sustained by adjacent nanoparticles if the coupling strength between them surpasses the individual ohmic and radiative losses[162]. The authors claim that an entanglement witness, a metric that can tell apart entangled states from separable ones, can be experimentally determined making far-field measurements of the field quadratures.

All the references cited above studied *passive* properties of the entanglement between particles supported by plasmonic structures, i.e., whether entanglement survives coupling to mesoscopic coherent free-electron oscillations in metals. In this chapter I show that plasmonic based metamaterials, i.e., materials whose properties are based on structural rather than intrinsic properties, perform phase operations over maximally entangled Bell pairs. To this end we perform a Young's double-slit type quantum eraser experiment as first shown by Walborn et al.[163], which is an optical analog of the experiment first proposed by Scully, Englert, and Walther[164] in the context of atoms. In this context, the *which-path markers* (WPM) are implemented using elliptical bullseye apertures tuned to act as quarter-waveplates.

I start this chapter introducing the quantum eraser effect and its relation to the concepts of complementarity in quantum mechanics. Next, I provide explicit calculations of the expected results both for single photon as well as coincidences detection, showing the need for the presence of quarter waveplates as a key component in the Young interferometer to observe the effect. I then present our efforts to reproduce a previously reported elliptical bullseye plasmonic structure that behaves as a quarter waveplate. Since the total transmission rates of our structures is less than 10^{-3}, we need a bright state-of-the-art entangled photon source. I finish the chapter by characterizing such a source and demonstrating the the quantum eraser effect mediated by plasmons.

6.1 Complementarity, which-path markers and quantum eraser

A quantum eraser experiment is an interferometry experiment that demonstrates several key aspects of quantum mechanics, including quantum superposition, entanglement and complementarity.

In the optical form, the first component of the experiment is a single photon double-slit experiment, first demonstrated by Taylor using a faint light beam[165]. In the modern version (Fig. 6.1), a stream of single photons can be obtained using a heralded photon source based on spontaneous parametric downconversion (SPDC). We can use photon post-selection to only consider photons ('clicks' in the single photon detector after the double-slit[166]) matching those of the heralding arm. By lowering the rate at which photons are generated, we can ensure that *on average* - it is an asynchronous source - we only have *one* photon in the path between the SPDC crystal and the detector after the double-slit. After passing the double-slit a solid state detector records an interference pattern, indicating that the photon existed as a *superposition*, going through *both* slits[167]. If the measurement is performed scanning a

single-photon detector the result is equivalent: single photons interfere as waves, despite being detected by 'click' detectors. This experimental fact reveals other quantum mechanical concepts, that of wave-particle duality, associated with the concept of complementarity.

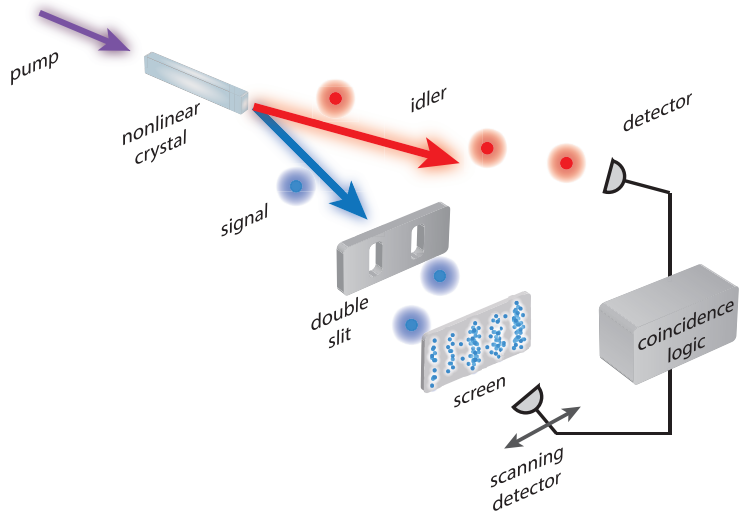

Figure 6.1: Schematic of the single photon Young's double-slit experiment using an heralded photon source. The detector in the idler arm heralds photon detection events in the signal source. It provides a convenient way of performing post-selection, discarding all photon detections (counts) that are not preceded by heralding photons.

Wave-particle duality is one of the ways in which the complementarity principle manifests. That is, measuring (or preparing) two conjugated magnitudes of a quantum mechanical state cannot be performed with arbitrary accuracy. This property of quantum mechanical systems can be thought of as an analog of Heinsenberg's uncertainty principle*[169].

In our single-photon double-slit experiment, we could try to figure out a way in which we could measure through which slit a photon passed †. Imagine we were allowed to determine with full accuracy through which slit the photon passed, perhaps by looking with a clever instrument into the slits when a photon passed through it. Since 'particles' have a definite location, and we would know the particular slit the photon has passed through, we could say the photon has *behaved* as a particle. In this case the *distinguishability* between the different paths the photon has taken would be $\mathcal{D} = 1$. The consequence of this complete knowledge

*Performing weak measurements, one can gather information on the complementarity principle and its link to the position-momentum Heisenberg uncertainty principle[168]. However, weak measurement followed by post-selection do not allow simultaneous position and momentum measurements for each individual particle, but rather allow measurement of the average trajectory of the particles that arrive at different positions.

†This kind of Gedanken experiment to determine through which slit the photon has passed dates back to the Bohr-Einstein debates on the foundations of quantum mechanics.

on the particle position is complete ignorance of the 'wave' phase (momentum), in order to satisfy Heisenberg's uncertainty principle. As a consequence, the *visibility* of the interference pattern would be negligible ($\mathcal{V} = 0$). For intermediate values on the information between the conjugated magnitudes, the distinguishability $\mathcal{D}$ and visibility $\mathcal{V}$ are related by the Englert-Greenberger-Yasin duality relation[170,171,172]:

$$\mathcal{D}^2 + \mathcal{V}^2 \leq 1 \tag{6.1}$$

The quantum eraser experiment is a clever way to obtain information about which path a photon has taken. Combining a source of polarization-entangled photons[‡] - instead of only heralded photons - with two orthogonal quarter-waveplates at the slits, we can implement an efficient *which-path marker* (WPM). As a consequence of the gathered knowledge, the interference pattern would disappear. The WPM information can be *erased* at will, hence the name of the experiment.

6.1.1 Single photon interference after the slits

Let me introduce the topic by considering single photon detection after the slits. We assume our entangled photon source produces Bell states $|\Phi^+\rangle$ of the form expressed in Eq. 6.7. We put the signal arm through the double slit. Since photons can take any of the two path the total state needs to be represented as the coherent superposition of photons in this arm going through both slits. Mathematically, this is expressed as:

$$|\psi\rangle = \frac{1}{\sqrt{2}}\left[\left|\Phi_1^+\right\rangle + \left|\Phi_2^+\right\rangle\right] \tag{6.2}$$

1. In the case in which no *which path marker* (WPM) is present, each of the paths can be casted as:

$$\begin{aligned}\left|\Phi_1^+\right\rangle &= \frac{1}{\sqrt{2}}\left[|H\rangle_{s1}|H\rangle_p + |V\rangle_{s1}|V\rangle_p\right] \\ \left|\Phi_2^+\right\rangle &= \frac{1}{\sqrt{2}}\left[|H\rangle_{s2}|H\rangle_p + |V\rangle_{s2}|V\rangle_p\right]\end{aligned} \tag{6.3}$$

where the indices s1, s2 indicate the slits 1, 2 in the signal arm, and p indicates photons in the idler arm. That is, the 'signal' part of the total state can take *any* of both paths through the different slits. A density matrix representation ($\hat{\varrho} = |\Psi\rangle\langle\Psi|$) of such state in the $\{H, V\}$

[‡]Polarization is a discrete degree of freedom, which makes algebra considerably simpler.

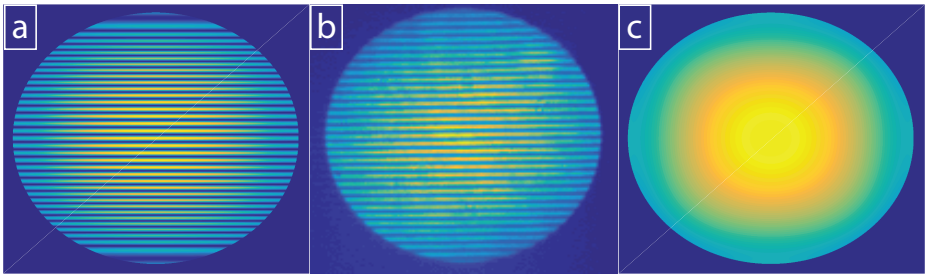

Figure 6.2: Detected light intensity corresponding to the single photon detection probability. (a) Numerical result based on Eq.6.4 for the case in which no WPM is present. (b) Experimental result, in accordance which numerical estimations. (c) Numerical result in the case in which a WPM is present.

basis is shown Fig.6.3-a . Since we are interested in single photon detection after the slits, we need to take the partial trace with respect with the redundant degrees of freedom. We start by taking the partial trace with respect to the polarization degrees of freedom in the idler arm. That is, detection after the slits is not conditional to a particular degree of freedom in the idler arm. After this operation we are left with a density matrix (Fig.6.3-b) in which no phases are present. Since we are only interested in intensity after the slits, the last step is to trace out over the polarization degrees of freedom in the signal arm. We are left with the density matrix in Fig.6.3-c. This matrix representation correspond to a *coherent superposition* of both slit states, meaning that single photons in the signal arm go through *both* slits.

In the typical quantum eraser experiments, the experimenter normally looks at the far-field after the slits. We opt for a different approach in which we make use of a high numerical aperture microscope objective to collect the transmitted photons. Furthermore, we image the collected photons in the k-vector space by imaging the back focal plane of the microscope objective into a EMCCD camera. Under these conditions the intensity collected can be expressed as:

$$I(\vartheta) = cos^2\left[\frac{\pi d sin(\vartheta)}{\lambda}\right] sinc^2\left[\frac{\pi l sin(\vartheta)}{\lambda}\right] \tag{6.4}$$

Where I represents the transmitted intensity along an angle ϑ, d is the distance between the slits, l is the width of the holes and λ is the wavelength of the light illuminating the structure.

Numerical results based on Eq.6.4 are presented in Fig.6.2-a, for which we have considered a hole diameter $l = 300nm$ and a distance between the slits $d = 12\mu m$ to match the characteristics of the structures used in our experiment. We see that the numerically calculated image coincides to a high degree with the experimental results for our structure, presented in Fig.6.2-b. We note that marginal differences appear as the angle increases due to the fact that we have not made a correct projection of the collection in the calculated image. Eq.6.4

provides a function of angles ϑ, whereas detection in the back focal plane makes a projection of the sphere over a plane.

2. Let me now consider the case in which a WPM is present.

We consider the first quarter waveplate to have a rotation angle of 0 degrees with respect to the angle defined by the $|H\rangle$ polarization, and the second waveplate to have an angle of 90 degrees which respect to to it (i.e. aligned with the $|V\rangle$ polarization). The transformations can be expressed as:

$$\begin{aligned} \hat{QWP}_1(0)\,|H\rangle &= \exp(i\pi/4)\,|H\rangle\,; \qquad \hat{QWP}_1(90)\,|H\rangle = \exp(-i\pi/4)\,|H\rangle \\ \hat{QWP}_2(0)\,|V\rangle &= \exp(-i\pi/4)\,|V\rangle\,; \qquad \hat{QWP}_2(90)\,|V\rangle = \exp(i\pi/4)\,|V\rangle \end{aligned} \tag{6.5}$$

These operations act *globally* on the total state. A matrix representation of the total state is shown in Fig.6.3-d, which differs from the case in which no WPMs are present in terms of phase. These phases are however important. We follow the same procedure as in the case with no WPM. First we take the partial trace over polarization degrees of freedom in the idler arm (Fig.6.3-e). Next, we project over the polarization degrees of freedom over the signal arm. We are left with the *statistical mixture* state in Fig.6.3-f, in which the single photon *either* passes through one or the other slit with 50% probability. In this situation, there is no interference pattern, since the quarter waveplates introduce a perfect WPM.

Given the presence of *perfect* WPM, the intensity collected can be expressed as:

$$I(\vartheta) = sinc^2\left[\frac{\pi l sin(\vartheta)}{\lambda}\right] \tag{6.6}$$

The equation does not depend this time on the separation between slits. A numerically generated image based on Eq.6.6 is provided in Fig.6.2-c.

6.1.2 Coincidence detection and quantum eraser

I now discuss the case of coincidence detection. In this case, we ask ourselves for the probability of detecting a photon in the signal arm (after the slits) *conditional* to detecting a photon in the idler arm of a certain polarization. In the previous section we have seen how the introduction of the quarter waveplates allows to introduce WPMs which removes the interference pattern. We will now show how we can *erase* this information, in other words we perform the quantum eraser effect.

We start considering the total state, represented in Fig.6.3-d. We are interested in detection coincidences *after projection* with a polarizer in the idler arm. Projection over different polarization basis produce distinct results:

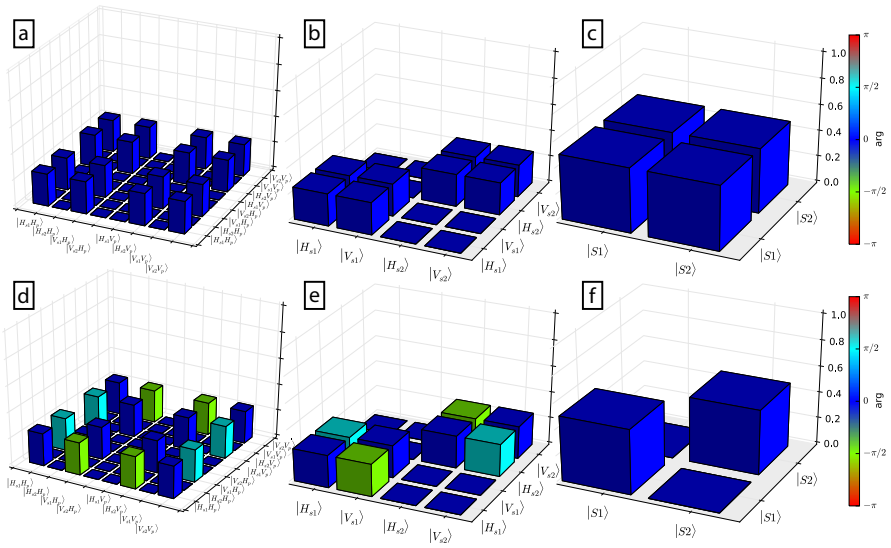

Figure 6.3: Density matrix representation for a Bell state Φ^+ passing through a double slit, without QWP at the slits (a), and with QWP (d). Corresponding reduced density matrix, after tracing out the polarization degree of freedom in the idler arm (b) and (e). Single photon density matrix after the slit (c)-(e). Note that (f) corresponds to a *superposition* state leading to interference, whereas (c) is a *statistical mixture* that does not lead to interference. When detecting coincidences, the QWP is necessary to observe interference.

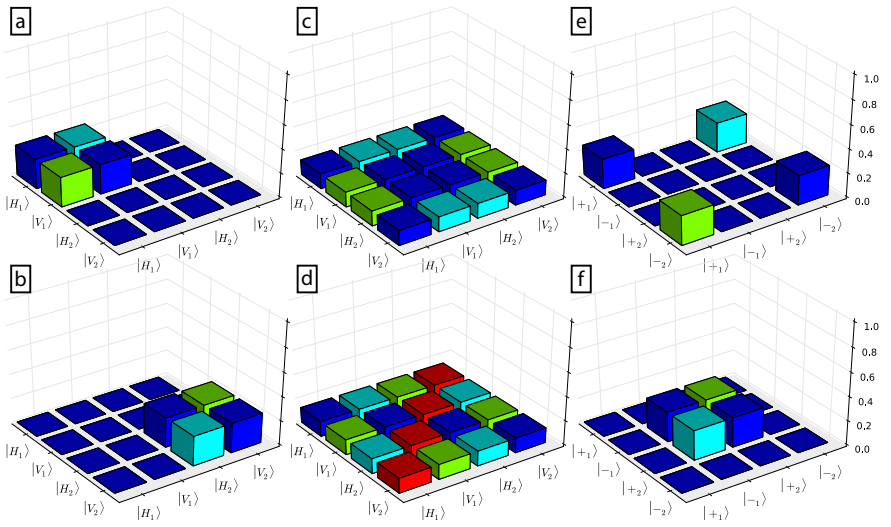

Figure 6.4: Reduced density matrix representation for a Bell state Φ^+ passing through a double slit, after performing different projections over $\left|H_p\right\rangle$ (a), $\left|V_p\right\rangle$ (b), $\left|D_p\right\rangle$(c) and $\left|A_p\right\rangle$(d) over the idler arm. (e)-(f) show the same projections as in (c)-(d) expressed in a different basis.

a. Reduced density matrix after projection over $\left|H_p\right\rangle$ in the {H,V} basis.

Since we started with a maximally entangled Bell state, knowledge of the polarization of one of the photons in one arm determines properties of the polarization in the other arm. In this case we see that we are left with a state that is a coherent superposition of photons with horizontal and vertical polarizations, *both passing through slit 1*. We are not further projecting over any polarization after the double slit, and horizontal and vertical polarizations are orthogonal, so these two degrees of freedom cannot interfere in our detection, simply adding up when photodetection is performed. Hence in this case there is no interference in the coincidence detection.

b. Reduced density matrix after projection over $\left|V_p\right\rangle$ in the {H,V} basis.

We are here in the same situation as in the previous point, but now the superposition state passes through the second slit. Again, no interference.

These previous two projections indicate that a *non-local* operation on the state allows us to determine through which slit the photon passes, i.e. we are able to introduce a non-local WPM. We well see now how projection over different bases erases the knowledge about through which slit the photon transmitted:

c. Reduced density matrix after projection over $\left|D_p\right\rangle \propto \left|H_p\right\rangle + \left|V_p\right\rangle$ ($\left|D_p\right\rangle \propto \left|H_p\right\rangle - \left|V_p\right\rangle$) in the {H,V} basis.

In this case we project with a polarizer set at 45/-45 degrees over the idler arm. A priori, we cannot see whether we can tell something about through which slit the photon in the idler arm might go. We solve this by performing a change of basis into the diagonal/antidiagonal vectors.

e. Reduced density matrix after projection over $\left|A_p\right\rangle \propto \left|H_p\right\rangle + \left|V_p\right\rangle$ ($\left|A_p\right\rangle \propto \left|H_p\right\rangle - \left|V_p\right\rangle$) in the {D,V} basis.

Now we clearly see that the state is a coherent superposition of photons passing though $|+_1\rangle + |-_2\rangle(|-_1\rangle + |+_2\rangle)$. Again, $|+\rangle$ and $|-\rangle$ are orthogonal and they do not interfere in this basis, however when decomposed back into the {H,V} basis we see that the horizontal(vertical) component survive, whereas the vertical(horizontal) does not. We have successfully *erased* the which path marker information by performing a non-local projection, recovering interference proportional to the horizontal(vertical) component.

6.2 Elliptical bullseye antennas. Optical antennas as micron-sized waveplates

I have previously shown that the quarter waveplate (QWP) is a key component of the quantum eraser experiment. In this section I show how elliptical plasmonic bullseye antennas (BEA) act as quarter-wavelength polarization retarders.

BEA are a range of plasmonic nanostructures in which a hole of subwavelength dimensions is combined with a concentric periodical grating[173]. Incident light scatters on the grooves and couples to surface plasmons (SPP), which propagate and tunnel through the whole. The period of the grating determines the conditions for constructive interference between the scattered surface wave and the incident light[174]. As explained previously, this constructive interference creates the so-called extraordinary optical transmission (EOT) effect, in which the transmission of the structure is higher than the expected from the physical size of the hole.

Drezet et al. first demonstrated how *elliptical* BEA induce linear birefringence on incident light[175]. By stretching the long axis of the ellipse by one quarter of the period with respect to the short axis, SPP along the long and short axes are shifted by $\pi/2$. Their results were further improved to achieve a perfect waveplate by both tuning the relation of distances between the last groove and the hole, and the length of the holes along both axis[176].

I now detail our efforts to reproduce these results. We used electron beam lithography (EBL) to pattern the elliptical grooves of the BEAs on 300nm-thick Au thin films. These films are optically thick, ensuring no light is transmitted through them. We next use focused ion beam (FIB) milling to make the central holes. A typical sample is shown in Fig.6.5-a.

Next, we measured light transmission over a set of samples with varying nominal groove pitch. Fig.6.5-b shows the EOT effect on our BEA, with the peak of optical transmission being a function of the groove period in line with previous results[174]. By tuning the groove pitch, we ensure the maximum transmission wavelength of the BEA to overlap the wavelength of one of the arms of our entangled photon source. We fine tune the wavelength of the entangled photon source by carefully controlling the temperature of the crystal to match the wavelength at which maximum transmission is achieved in our samples.

Once the period of the grating has been chosen, we focus on the polarization properties of our elliptical BEA. We use a linearly polarized light beam incident at 45 degrees with respect to our elliptical BEA. Transmitted light is collected and passed through a linear polarization analyzer. When the BEA acts as a QWP, it produces circularly polarized light, which has constant transmission for all the angles in the analyzer. Fig.6.5-inset shows such a measurement. Perfectly polarized light would have exactly 50% transmission for all angles. Our best result, shown in the figure, show some variability with respect to the benchmark. This implies our elliptical BEA deviate slightly from a perfect QWP, affecting the expected interference visibil-

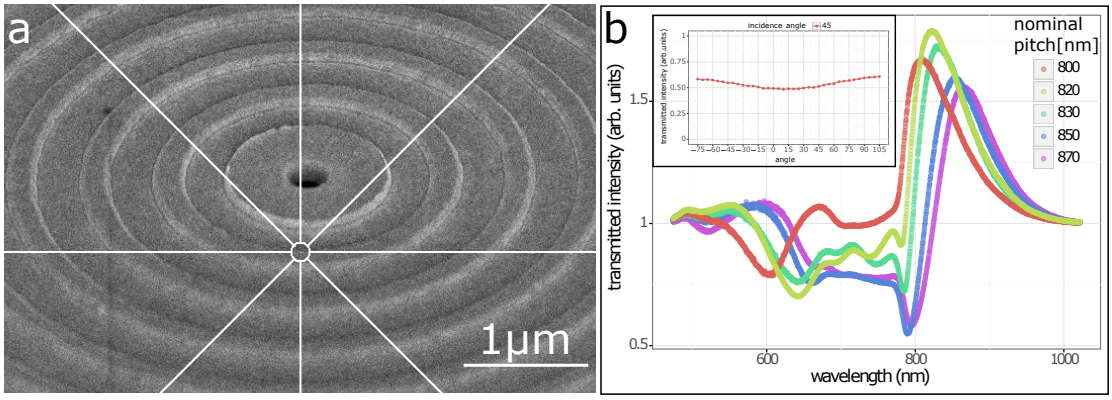

Figure 6.5: (a) Scanning electron microscope image of BEA. (b) Transmission of BEA of different nominal pitch. The inset shows the transmission after a linear analyzer at different angles. Incident light is linearly polarized at 45 degrees respect the fast axis of the BEA.

ity in the quantum eraser experiment we will present at the end of this chapter.

6.3 Source of photon pairs maximally entangled in polarization

Elliptical BEA aperture are ideal candidates to reproduce the quantum eraser experiment mediated by plasmons. However, the transmission of one such nanoaperture is typically 10^{-3}–10^{-4} (cf. section 6.2). This means only one photon in several thousands will go through the aperture. It is obvious then that we need a *bright* entangled photon source to perform such an experiment.

Such a bright source was built by Fabian Steinlechner and co-workers from the Optoelectronics Group at ICFO lead by Prof. Valerio Pruneri[177]. After some modifications[§] the source provided a detected pair rate over 1 million pairs s^{-1} per nm per mW of pump power, combined with high quantum entanglement quality (fidelity with the ideal Bell state of $98.3\% \pm 0.4\%$ and violation of CHSH's inequality by more than 85 standard deviations in only 10 seconds for 10 μW of pump power). A full characterization of the source was performed by Carlos Abellan for his master thesis[2], we refer the reader to this reference for further details on the entanglement properties of the photon pairs emitted by the source. Here, I reproduce some of their previous reports describing the source for completeness.

[§]The ppKTP crystal was swapped for a longer one, and the pump laser beam waist was modified to match the crystal

6.3.1 Principle of operation of the entangled photon sources

The source is sketched in Figure 6.7 (Box S). A grating-stabilized UV diode laser delivers more than 20 mW of continuous-wave radiation at 405.9 nm within a typical bandwidth of $\sim$ 0.1 nm. Such a large bandwidth is not sufficient for interfacing with atomic transitions, but is good enough for our applications. The laser is attenuated by a neutral density filter and coupled into a single mode fibre for mode filtering. After outcoupling, a set of lenses is used to focus the pump laser along the length of the crystal, matching the Rayleigh range of the quasi-TEM_{00} mode to the length of the crystal. A variable retarder matches the polarization of the mode to the one in which the most efficient parametric down-conversion (SPDC) is generated in the periodically-poled KTP (Potassium titanyl phosphate or $KTiOPO_4$) crystal. The crystal is grown such that, for each UV photon, two nearly degenerated photons with the same polarization are created at 785 nm and 840 nm. The two infrared photons have the same polarization as the incoming UV one, a process often called Type-0 SPDC.

In a probabilistic manner, two IR photons are generated in the crystal with a typical efficiency of $10^{-6} - 10^{-7}$. They pass through a QWP, designed for 800nm and oriented at 45 deg, and are reflected back by a parabolic mirror matching focal length of the focusing lenses. In this way, the IR photons undergo a total phase retardation of $2 \times \pi/2 = \pi$ before passing again through the KTP crystal. Since the pump laser has roughly twice the frequency as the SPDC photons, it will see the QWP as a HWP, and undergoes a total polarization flip of $2 \times \pi = 2\pi$, leaving it in the same polarization state. This pump beam passes again through the crystal generating again two SPDC photons. The variable retarder at the entrance of the source is used to compensate for the non-perfect behavior of the rest of the retarders due to wavelength mismatch. The generated SPDC photons are color filtered by a dichroic mirror to remove the pump beam, and coupled into a single mode fibre with NA = 0.13 for spatial-mode filtering.

Assuming the pump laser has horizontal polarization, the two photons generated in the first pass through the crystal will have vertical polarization (after double pass through the QWP), while the photons generated in the second pass will remain horizontally polarized. If we decrease sufficiently the pump power, we can only probabilistically say the photon pairs where generated in the first *or* the second pass, since the probability of generating photons in both passes through the crystal is quadratically smaller. Hence the state should be described as a superposition according to the rules of quantum mechanics. However, one could make a time-tagged measurement, and know whether photons where generated in the first or the second pass. We note here that due to the phase matching condition, UV and IR photons travel at the same speed along the crystal. However, photons generated in the first path will travel in their way back along a different crystal axis, which has different refractive index. We remove this information using a YVO (yttrium orthovanadate or YVO_4) crystal oriented perpendicularly, which has the same refractive indexes along the propagation axis of the crystal

as the KTP (see Ref.[3] for full details). In this manner we remove the which path information and photons exiting the source can described as:

$$\left|\Phi^{+}\right\rangle = \frac{1}{\sqrt{2}}\left[\left|H_s H_p\right\rangle + e^{i} \quad \left|V_s V_p\right\rangle\right] \tag{6.7}$$

Two (or more) particles (or degrees of freedom) are entangled when the state describing them cannot be factorized (separated) into independent states for each particle. A necessary condition for particles to be entangled is that they are in a superposition state. The simplest example of a bipartite entangled state is a Bell state, which for polarization degrees of freedom is described by Eq.6.7, and where $|H\rangle$, $|V\rangle$ represent single photon states in the horizontal and vertical polarization, in the two arms signal and idler.

The nonlinear crystals are temperature stabilized, to within 0.1 C, using crystal ovens controlled using closed-loop feedback based on temperature readings given by thermo-couples. The ppKTP is typically set to 46 C; varying the temperature of the crystal 10 C allows tuning the wavelength over the $790 - 770$ nm range in the signal arm with corresponding idler photons. The phase φ of the source is fixed for a fixed temperature of the YVO crystal, typically set to 28C.

6.3.2 Properties of the entangled photon source

After out-coupling from the single mode fiber, a set of waveplates fixes the polarization basis, and compensates for polarization rotations generated by the fiber. One of the arms is further filtered using a 3 nm-broad dielectric filter centered at 825 nm, to remove unwanted single-photon detection events and any remaining light from the pump.

We perform the coincidence measurements in the different polarization bases combining a QWP and a polarizer (see Figure 6.7 Box 1). The counts detected by single photon avalanche diodes (SPAD) are fed to a correlator (coincidence detector) with a 1.2 ns detection window, which performs an electronic AND operation on the TTL (or NIM) pulses generated by the detectors.

At low pump powers (tens of μW before the ppKTP crystal), the heralding efficiency, defined as the ratio to two-fold coincidence counts divided by the individual counts is roughly 20%. This value is fairly large, although significantly smaller that the one recently reported[178]. Without any projective measurement, the brightness of the source is found to be 1 Mpairs s^{-1} mW^{-1} nm^{-1}. Equivalent to the maximum sustainable count rate if measurements were performed with four detectors in the set of maximally correlated bases. In other words, after setting the phase of our state to $\varphi = 0$ (Φ^{+}), and considering a measurement set in both the horizontal and diagonal basis, the obtained coincidences per second (within the 3nm bandwidth) would be:

$$\mathcal{C} = C_{HH} + C_{VV} = C_{DD} + C_{AA} = C_{RR} + C_{LL} = 10^6 s^{-1} \tag{6.8}$$

per mW of pump power; where H, V, D, A, R, L, stand for projectors in the horizontal, vertical, diagonal (+45 deg), anti-diagonal (-45 deg), right circular and left circular projector orientations. We note that this conditions are mutually exclusive, i.e., no *simultaneous* detection of two-horizontal and two vertical coincidences are present: *on average* half of the coincidences will be of one kind or the other, with a total coincidence detection of 1Mpairs per mW of pump power within the source bandwidth of 3nm. This values is one of the highest ever reported for such an entangled photon source[3].

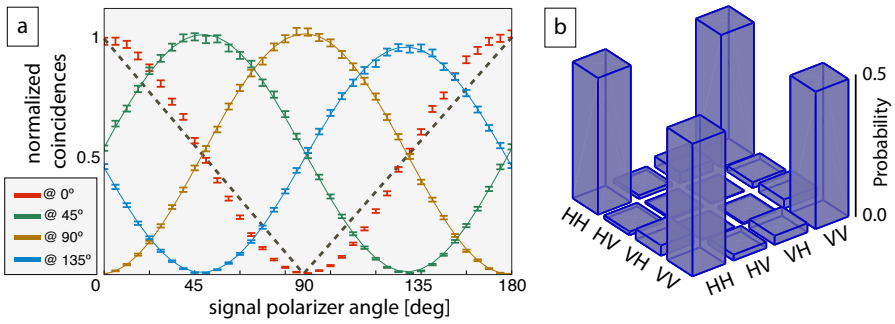

Figure 6.6: (a) Normalized coincidences detected for different settings of the signal and idler projectors (polarizers). The average visibility over the idler angle settings is $< \mathcal{V} >= 0.984 \pm 0.006$. Pump power was set to 20 μW for these emasurements. The dashed line represents the limit of the Bell-CHSH inequality for classical states. (b) The reconstructed density matrix of the source using a maximum-likelihood reconstruction algorithm. Pump power was set to 10 Î¼W.

Approximating our state as the Bell state described above, we can estimate the visibility of our source as a fit to the detected coincidences[3]:

$$\mathcal{C} \quad = N(1 - \mathcal{V}\sin(\alpha(insert_here)\beta)) \tag{6.9}$$

where N is a normalization constant indicated the total number of photons and realted to the pump power of the source and α, β are the angle setting of our projectors (Figure 6.6a). We found $< \mathcal{V} >= 0.984 \pm 0.006$, without substraction of any dark coincidences. From these measurements we obtained a CHSH parameter[††] $S \sim 2.81$, with over 85 standard deviations above the classical limit S(C) = 2 at 10 μW pumping power. The parameter decreases to $S \sim 2.74$ at a pumping power of 100 μW, with an increased confidence margin of over

[††]A version of the Bell inequality given by Clauser, Horne, Shimony, and Holt, for sets of angles that result in normalized coincidences differing the most from any classical state

500 standard deviations above any classical correlation. This clearly indicates that the source provides bi-partite states of light incompatible with any classical field. Further information about the entangled state generated by the source was gathered by performing a maximum-likelihood estimation of the (physical) density matrix (Figure 6.6b). The fidelity, based on the trace distance, between the reconstructed density matrix and the ideal Φ^+ state was found to be $\mathcal{F}(\varrho_{MLE}, |\Phi^+\rangle\langle\Phi^+|) = 0.9830 \pm 0.004$. This means, from a probabilistic perspective, that the entangled pairs generated by our source behave as the ideal Φ^+ state $96.6\% \pm 0.7\%$ of the time. We encourage the reader to consult the references[3] and[3] for a more detailed description of the source as well as the details of its characterization.

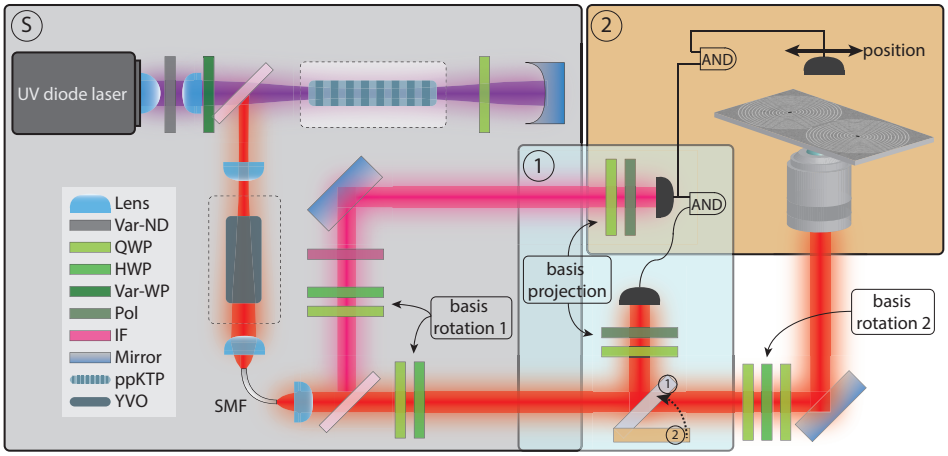

Figure 6.7: Sketch of the quantum eraser experiment. (S) Source of polarization entangled photon pairs based on a double-pass sandwich configuration (see text for details). (1) Bell test measurements. (2) Quantum eraser measurements.

6.4 Quantum eraser effect mediated by plasmons

In this section I show the main result of this chapter, the measurement of the coincidence counts demonstrating the quantum eraser effect mediated by a plasmonic double-slit with integrated micron-sized QWP.

A sketch of the experimental set-up is shown in Fig.6.7. We perform single photon detection in the idler arm after projecting on a linear polarizer using single photon avalanche diodes (SPAD). A similar SPAD is mounted on a linear translation stage actuated by a DC servo motor. This SPAD is placed at a conjugated plane to the back focal plane aperture of the collection microscope objective after the slits. Electronic signals, either in the form of NIM are fed into an electronic circuit performs the AND operation ??, equivalent to perform a

coincidence detection. The discriminator's is set such that a coincidence is registered if both electronic signal arrive at the coincidence card within 1.2ns time difference or less.

Despite the high brightness of our entangled photon source, the typical transmission of a *single* BEA is of the order of 10^{-3}. We focus our excitation beam to cover a $20\mu m x 20\mu m$ area, in which two elliptical bullseye aperture exist (Fig.6.8-inset). Under this experimental conditions, single photon detection rate in the idler arm is $5 Mphotons \cdot s^{-1}$, whereas detected photons in the signal arm after the slits are only $50 photons \cdot s^{-1}$. This low count rate is due to the spread in space of the transmitted photons, which we are only collecting with a "point-like detector".

It is worth noting that due to the low detected photons we had to make use of SPAD with typical dark-count rates of $5-7 Counts \cdot s^{-1}$ (Tau-SPAD, Picoquant). Under these conditions, accidental coincidences amount to less than $0.3 s^{-1}$ and are show as error bars in Fig.6.8, where we demonstrate the quantum eraser effect, which is the main result of this chapter.

The figure shows coincidences over an integration time of 120 s per spatial point. Inspection of the figure shows a coincidence detection rate $1 Coincidence \cdot s^{-1}$. This constitutes a $SNR > 2$ even for the projection basis providing the lowest coincidence rate, good enough (but just enough) to be able to perform the experiment. We detect almost *no interference*, as expected from the algebraic calculations provided in the previous section 6.1. In essence, a which path marker is present allowing us to determine through which slit the photon has passed. Since our elliptical BEA deviate slightly from perfect waveplates, the interference is not completely suppressed, and some residual fringes are present within the accidental count error bars.

The WPM information is erased after projecting with a polarizer set at an angle of 45 degrees over the idler arm. In this case the interference pattern is recovered (purple dots). As previously discussed, we need the presence of the QWPs at each slit to be able to measure interferences in the coincidence count. In this case we cannot tell through which slit the single photon has passed and the state needs to be described as a coherent superposition of states passing through both holes.

Two subtleties are present in this experiment. First, the presence of EOT in our BEA ensures the presence of surface plasmons. Bell states, in which at most 2 photons are present in the arms at once, couple to these surface plasmons oscillations which are typically represented using many-body quantum formalisms. The manybody oscillations maintain the quantum character of the original entangled state for the experiment to work, but still there is at mosts a single such oscillation at once in the structure, while maintaining the quantum character of the state. Second, our elliptical BEA acts as QWP as shown by the presence of interference in the coincidence detection. This action is performed via the single SPP oscillations.

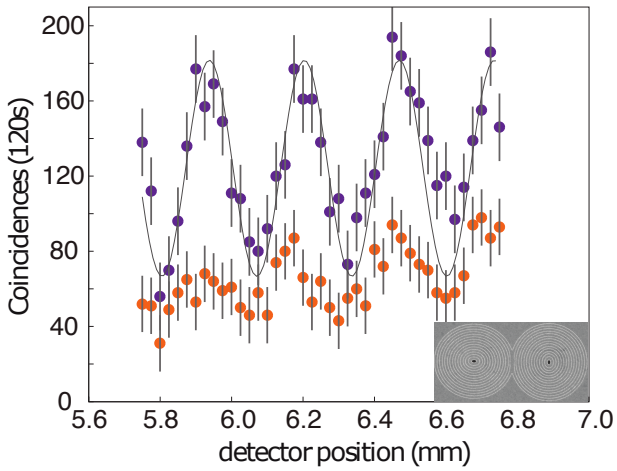

Figure 6.8: Detected coincidences after the Young's double-slit and projecting over $|H\rangle$ (orange) and $|D\rangle$ (purple). Vertical grey lines represent the accidental coincidences expected given the single photon detection rates and the time window used in the experiment.

6.5 Conclusions

I performed a Young's double-slit type quantum eraser experiment using plasmonic structures that present subwavelength features. Our structures, elliptical BEA suporting SPP, act as controlled gates for Bell states, rather than behaving as projectors. The action of the gates depends crucially on a transfer between single propagating photon and bound plasmon degrees of freedom. Apart from its basic research interests, the quantum eraser experiment has practical applications. A quantum key cryptography protocol with inherent security against detector attacks can be implemented using the effect[179]. The present work is an addition to the reports in which SPP successfully mediate quantum interactions[180], and strengthens the potential role of SPP-supporting structures as candidates for practical applications in both quantum computation and quantum cryptography.

References

[1] Lukas Novotny and Niek Van Hulst. Antennas for light. *Nature Photonics 2011 5:2*, 5:83–90, 2 2011.

[2] Markus Pfeiffer, Klas Lindfors, Christian Wolpert, Paola Atkinson, Mohamed Benyoucef, Armando Rastelli, Oliver G. Schmidt, Harald Giessen, and Markus Lippitz. Enhancing the optical excitation efficiency of a single self-assembled quantum dot with a plasmonic nanoantenna. *Nano Letters*, 10:4555–4558, 11 2010.

[3] Lukas Novotny and Bert Hecht. *Principles of Nano-Optics*. Cambridge University Press, 2012.

[4] Lucca Kühner, Mario Hentschel, Ute Zschieschang, Hagen Klauk, Jochen Vogt, Christian Huck, Harald Giessen, and Frank Neubrech. Nanoantenna-enhanced infrared spectroscopic chemical imaging. *ACS Sensors*, 2:655–662, 5 2017.

[5] H. J. Levene, J. Korlach, S. W. Turner, M. Foquet, H. G. Craighead, and W. W. Webb. Zero-mode waveguides for single-molecule analysis at high concentrations. *Science (New York, N.Y.)*, 299:682–686, 1 2003.

[6] Hongxing Xu, Javier Aizpurua, Mikael Käll, and Peter Apell. Electromagnetic contributions to single-molecule sensitivity in surface-enhanced raman scattering. *Physical Review E*, 62:4318, 9 2000.

[7] Nahla A. Hatab, Chun Hway Hsueh, Abigail L. Gaddis, Scott T. Retterer, Jia Han Li, Gyula Eres, Zhenyu Zhang, and Baohua Gu. Free-standing optical gold bowtie nanoantenna with variable gap size for enhanced raman spectroscopy. *Nano Letters*, 10:4952–4955, 12 2010.

[8] Mathias Haase, Christian G. Hübner, Fabian Nolde, Klaus Müllen, and Thomas Basché. Photoblinking and photobleaching of rylene diimide dyes. *Physical Chemistry Chemical Physics*, 13, 2011.

[9] Pascale Senellart, Glenn Solomon, and Andrew White. High-performance semiconductor quantum-dot single-photon sources. *Nature Nanotechnology 2017 12:11*, 12:1026–1039, 11 2017.

[10] Christian Kurtsiefer, Sonja Mayer, Patrick Zarda, and Harald Weinfurter. Stable solid-state source of single photons. *Physical Review Letters*, 85:290, 7 2000.

[11] Paolo Biagioni, Jer Shing Huang, and Bert Hecht. Nanoantennas for visible and infrared radiation. *Reports on Progress in Physics*, 75:024402, 1 2012.

[12] O. L. Muskens, V. Giannini, J. A. Sánchez-Gil, and J. Gómez Rivas. Strong enhancement of the radiative decay rate of emitters by single plasmonic nanoantennas. *Nano Letters*, 7:2871–2875, 9 2007.

[13] Alberto G. Curto, Giorgio Volpe, Tim H. Taminiau, Mark P. Kreuzer, Romain Quidant, and Niek F. Van Hulst. Unidirectional emission of a quantum dot coupled to a nanoantenna. *Science*, 329:930–933, 8 2010.

[14] J. D. Joannopoulos, Pierre R. Villeneuve, and Shanhui Fan. Photonic crystals: putting a new twist on light. *Nature 1997 386:6621*, 386:143–149, 3 1997.

[15] W. E. Moerner and L. Kador. Optical detection and spectroscopy of single molecules in a solid. *Physical Review Letters*, 62:2535–2538, 5 1989.

[16] M. Orrit and J. Bernard. Single pentacene molecules detected by fluorescence excitation in a p -terphenyl crystal. *Physical Review Letters*, 65:2716–2719, 11 1990.

[17] William L Barnes, Simon A R Horsley, and Willem L Vos. Classical antennas, quantum emitters, and densities of optical states. *Journal of Optics*, 22:073501, 7 2020.

[18] E M Purcell. Spontaneous emission probabilities at radio frequencies. *Phys Rev*, 69:681, 1946.

[19] Lutz Langguth, Romain Fleury, Andrea Alù, and A. Femius Koenderink. Drexhage's experiment for sound. *Physical Review Letters*, 116:224301, 6 2016.

[20] T. Ohtsuki, H. Yuki, M. Muto, J. Kasagi, and K. Ohno. Enhanced electron-capture decay rate of b 7 e encapsulated in c 60 cages. *Physical Review Letters*, 93:112501, 9 2004.

[21] K H Drexhage, H Kuhn, and F P Schäfer. Variation of the fluorescence decay time of a molecule in front of a mirror. *Berichte der Bunsengesellschaft fur physikalische Chemie*, 72, 1968.

[22] K. H. Drexhage. Influence of a dielectric interface on fluorescence decay time. *Journal of Luminescence*, 1-2, 1970.

[23] H. Paul. Photon antibunching. *Reviews of Modern Physics*, 54:1061–1102, 10 1982.

[24] S. C. Hagness A. Taflove. Computational electrodynamics: the finite-difference time-method. *Sencond edition. Artech house Publishers: Norwood.*, ISBN, 2000.

[25] Max Metlay. Fluorescence lifetime of the europium dibenzoylmethides, 1963.

[26] L. Allen and J.H. Eberly. *Optical Resonance and Two-level Atoms*. Courier Corporation, 1987.

[27] I. Gerhardt, G. Wrigge, P. Bushev, G. Zumofen, M. Agio, R. Pfab, and V. Sandoghdar. Strong extinction of a laser beam by a single molecule. *Physical Review Letters*, 98:033601, 1 2007.

[28] J. Hwang, M. Pototschnig, R. Lettow, G. Zumofen, A. Renn, S. Götzinger, and V. Sandoghdar. A single-molecule optical transistor. *Nature*, 460, 2009.

[29] Michele Celebrano, Philipp Kukura, Alois Renn, and Vahid Sandoghdar. Single-molecule imaging by optical absorption. *Nature Photonics 2010 5:2*, 5:95–98, 1 2011.

[30] P. Michler, A. Imamoğlu, M. D. Mason, P. J. Carson, G. F. Strouse, and S. K. Buratto. Quantum correlation among photons from a single quantum dot at room temperature. *Nature 2000 406:6799*, 406:968–970, 8 2000.

[31] Antonio Badolato, Kevin Hennessy, Mete Atatüre, Jan Dreiser, Evelyn Hu, Pierre M. Petroff, and Atac Imamoğlu. Deterministic coupling of single quantum dots to single nanocavity modes. *Science*, 308:1158–1161, 5 2005.

[32] Peter Lodahl, A. Floris Van Driel, Ivan S. Nikolaev, Arie Irman, Karin Overgaag, Daniël Vanmaekelbergh, and Willem L. Vos. Controlling the dynamics of spontaneous emission from quantum dots by photonic crystals. *Nature 2004 430:7000*, 430:654–657, 8 2004.

[33] F. Jelezko, C. Tietz, A. Gruber, I. Popa, A. Nizovtsev, S. Kilin, and J. Wrachtrup. Spectroscopy of single n-v centers in diamond, 2001.

[34] A. Sipahigil, K. D. Jahnke, L. J. Rogers, T. Teraji, J. Isoya, A. S. Zibrov, F. Jelezko, and M. D. Lukin. Indistinguishable photons from separated silicon-vacancy centers in diamond. *Physical Review Letters*, 113:113602, 9 2014.

[35] P. Siyushev, K. Xia, R. Reuter, M. Jamali, N. Zhao, N. Yang, C. Duan, N. Kukharchyk, A. D. Wieck, R. Kolesov, and J. Wrachtrup. Coherent properties of single rare-earth spin qubits. *Nature Communications 2014 5:1*, 5:1–6, 5 2014.

[36] Samuele Grandi, Kyle D. Major, Claudio Polisseni, Sebastien Boissier, Alex S. Clark, and E. A. Hinds. Quantum dynamics of a driven two-level molecule with variable dephasing. *Physical Review A*, 94:063839, 12 2016.

[37] Sen Yang, Ya Wang, D. D.Bhaktavatsala Rao, Thai Hien Tran, Ali S. Momenzadeh, M. Markham, D. J. Twitchen, Ping Wang, Wen Yang, Rainer Stöhr, Philipp Neumann, Hideo Kosaka, and Jörg Wrachtrup. High-fidelity transfer and storage of photon states in a single nuclear spin. *Nature Photonics 2016 10:8*, 10:507–511, 6 2016.

[38] Andrei Faraon, Ilya Fushman, Dirk Englund, Nick Stoltz, Pierre Petroff, and Jelena Vučković. Coherent generation of non-classical light on a chip via photon-induced tunnelling and blockade. *Nature Physics 2008 4:11*, 4:859–863, 9 2008.

[39] Carsten H.H. Schulte, Jack Hansom, Alex E. Jones, Clemens Matthiesen, Claire Le Gall, and Mete Atature. Quadrature squeezed photons from a two-level system. *Nature 2015 525:7568*, 525:222–225, 8 2015.

[40] W. B. Gao, P. Fallahi, E. Togan, A. Delteil, Y. S. Chin, J. Miguel-Sanchez, and A. Imamoğlu. Quantum teleportation from a propagating photon to a solid-state spin qubit. *Nature Communications 2013 4:1*, 4:1–8, 11 2013.

[41] B. Hensen, H. Bernien, A. E. Dreaú, A. Reiserer, N. Kalb, M. S. Blok, J. Ruitenberg, R. F.L. Vermeulen, R. N. Schouten, C. Abellán, W. Amaya, V. Pruneri, M. W. Mitchell, M. Markham, D. J. Twitchen, D. Elkouss, S. Wehner, T. H. Taminiau, and R. Hanson. Loophole-free bell inequality violation using electron spins separated by 1.3 kilometres. *Nature 2015 526:7575*, 526:682–686, 10 2015.

[42] F. Jelezko, T. Gaebel, I. Popa, M. Domhan, A. Gruber, and J. Wrachtrup. Observation of coherent oscillation of a single nuclear spin and realization of a two-qubit conditional quantum gate. *Physical Review Letters*, 93:130501, 9 2004.

[43] Mario Agio. Molecular scattering and fluorescence in strongly confined optical fields. 2012.

[44] J. Hwang, M. M. Fejer, and W. E. Moerner. Scanning interferometric microscopy for the detection of ultrasmall phase shifts in condensed matter. *Physical Review A - Atomic, Molecular, and Optical Physics*, 73:021802, 2 2006.

[45] P. Kukura, M. Celebrano, A. Renn, and V. Sandoghdar. Imaging a single quantum dot when it is dark. *Nano Letters*, 9:926–929, 3 2008.

[46] Frank Vollmer and Stephen Arnold. Whispering-gallery-mode biosensing: label-free detection down to single molecules. *Nature Methods 2008 5:7*, 5:591–596, 6 2008.

[47] Eric Betzig and Robert J. Chichester. Single molecules observed by near-field scanning optical microscopy. *Science (New York, N.Y.)*, 262:1422–1425, 1993.

[48] Anshuman Singh, Gaëtan Calbris, and Niek F. Van Hulst. Vectorial nanoscale mapping of optical antenna fields by single molecule dipoles. *Nano Letters*, 14, 2014.

[49] A. F. Van Driel, I. S. Nikolaev, P. Vergeer, P. Lodahl, D. Vanmaekelbergh, and W. L. Vos. Statistical analysis of time-resolved emission from ensembles of semiconductor quantum dots: Interpretation of exponential decay models. *Physical Review B - Condensed Matter and Materials Physics*, 75:035329, 1 2007.

[50] N. F. van Hulst, N. P. de Boer, and B. Bölger. An evanescent-field optical microscope. *Journal of Microscopy*, 163:117–130, 8 1991.

[51] Anshuman Singh. Optical nanoantennas as cavities : nanoscale control of couplings strength and single photon emission. *TDX (Tesis Doctorals en Xarxa)*, 11 2017.

[52] Lars Neumann, Yuanjie Pang, Amel Houyou, Mathieu L. Juan, Reuven Gordon, and Niek F. Van Hulst. Extraordinary optical transmission brightens near-field fiber probe. *Nano Letters*, 11:355–360, 2 2010.

[53] Christophe Jung, Barbara K. Müller, Don C. Lamb, Fabian Nolde, Klaus Müllen, and Christoph Bräuchle. A new photostable terrylene diimide dye for applications in single molecule studies and membrane labeling. *Journal of the American Chemical Society*, 128:5283–5291, 4 2006.

[54] Martin Frimmer, Yuntian Chen, and A. Femius Koenderink. Scanning emitter lifetime imaging microscopy for spontaneous emission control. *Physical Review Letters*, 107:123602, 9 2011.

[55] Randy X. Bian, Robert C. Dunn, X. Sunney Xie, and P. T. Leung. Single molecule emission characteristics in near-field microscopy. *Physical Review Letters*, 75:4772, 12 1995.

[56] Robert E. Blankenship. *Molecular Mechanisms of Photosynthesis*. 2008.

[57] Vivian W.W. Yam. Woleds and organic photovoltaics: Recent advances and applications. *Green Energy and Technology*, 43, 2010.

[58] R. Smith, B. Liu, J. Bai, and T. Wang. Hybrid iii-nitride/organic semiconductor nanostructure with high efficiency nonradiative energy transfer for white light emitters. *Nano Letters*, 13, 2013.

[59] T. Förster. Zwischenmolekulare energiewanderung und fluoreszenz (intermolecular energy migration and fluorescence). *Annalen der Physik*, 2, 1948.

[60] Joseph R. Lakowicz. *Principles of fluorescence spectroscopy*. 2006.

[61] Rahul Roy, Sungchul Hohng, and Taekjip Ha. A practical guide to single-molecule fret, 2008.

[62] Cathy Y. Wong, Richard M. Alvey, Daniel B. Turner, Krystyna E. Wilk, Donald A. Bryant, Paul M.G. Curmi, Robert J. Silbey, and Gregory D. Scholes. Electronic coherence lineshapes reveal hidden excitonic correlations in photosynthetic light harvesting. *Nature Chemistry*, 4, 2012.

[63] Jing Shun Huang, Tenghooi Goh, Xiaokai Li, Matthew Y. Sfeir, Elizabeth A. Bielinski, Stephanie Tomasulo, Minjoo L. Lee, Nilay Hazari, and André D. Taylor. Polymer bulk heterojunction solar cells employing förster resonance energy transfer. *Nature Photonics*, 7, 2013.

[64] Stephan Uphoff, Seamus J. Holden, Ludovic Le Reste, Javier Periz, Sebastian Van De Linde, Mike Heilemann, and Achillefs N. Kapanidis. Monitoring multiple distances within a single molecule using switchable fret. *Nature Methods*, 7, 2010.

[65] Igor L. Medintz, Aaron R. Clapp, Hedi Mattoussi, Ellen R. Goldman, Brent Fisher, and J. Matthew Mauro. Self-assembled nanoscale biosensors based on quantum dot fret donors. *Nature Materials*, 2, 2003.

[66] André Kurs, Aristeidis Karalis, Robert Moffatt, J. D. Joannopoulos, Peter Fisher, and Marin Soljačić. Wireless power transfer via strongly coupled magnetic resonances. *Science*, 317:83–86, 7 2007.

[67] Aristeidis Karalis, J. D. Joannopoulos, and Marin Soljačić. Efficient wireless non-radiative mid-range energy transfer. *Annals of Physics*, 323:34–48, 1 2008.

[68] Adriano Barenco, David Deutsch, Artur Ekert, and Richard Jozsa. Conditional quantum dynamics and logic gates. *Physical Review Letters*, 74:4083, 5 1995.

[69] Ho Trung Dung, Ludwig Knoöll, and Dirk Gunnar Welsch. Intermolecular energy transfer in the presence of dispersing and absorbing media. *Physical Review A*, 65:043813, 4 2002.

[70] Toshihiro Nakamura, Minoru Fujii, Satoru Miura, Masaki Inui, and Shinji Hayashi. Enhancement and suppression of energy transfer from si nanocrystals to er ions through a control of the photonic mode density. *Physical Review B - Condensed Matter and Materials Physics*, 74:045302, 7 2006.

[71] M. J.A. De Dood, J. Knoester, A. Tip, and A. Polman. Förster transfer and the local optical density of states in erbium-doped silica. *Physical Review B - Condensed Matter and Materials Physics*, 71:115102, 3 2005.

[72] Christian Blum, Niels Zijlstra, Ad Lagendijk, Martijn Wubs, Allard P. Mosk, Vinod Subramaniam, and Willem L. Vos. Nanophotonic control of the förster resonance energy transfer efficiency. *Physical Review Letters*, 109:203601, 11 2012.

[73] Freddy T. Rabouw, Stephan A. Den Hartog, Tim Senden, and Andries Meijerink. Photonic effects on the förster resonance energy transfer efficiency. *Nature Communications 2014 5:1*, 5:1–6, 4 2014.

[74] Petru Ghenuche, Juan De Torres, Satish Babu Moparthi, Victor Grigoriev, and Jérôme Wenger. Nanophotonic enhancement of the förster resonance energy-transfer rate with single nanoapertures. *Nano Letters*, 14:4707–4714, 8 2014.

[75] P. Andrew and W. L. Barnes. Energy transfer across a metal film mediated by surface plasmon polaritons. *Science (New York, N.Y.)*, 306:1002–1005, 11 2004.

[76] Ardavan F. Oskooi, David Roundy, Mihai Ibanescu, Peter Bermel, J. D. Joannopoulos, and Steven G. Johnson. Meep: A flexible free-software package for electromagnetic simulations by the fdtd method. *Computer Physics Communications*, 181, 2010.

[77] S Albaladejo, R Gómez-Medina, L S Froufe-Pérez, H Marinchio, R Carminati, J F Torrado, G Armelles, A García-Martín, J J Sáenz, J Gómez Rivas, M Kuttge, P Haring Bolivar, H Kurz, and J A Sánchez. Radiative corrections to the polarizability tensor of an electrically small anisotropic dielectric particle. *Optics Express, Vol. 18, Issue 4, pp. 3556-3567*, 18:3556–3567, 2 2010.

[78] Pedro De Vries, David V. Van Coevorden, and Ad Lagendijk. Point scatterers for classical waves. *Reviews of Modern Physics*, 70:447, 4 1998.

[79] R. Vincent and R. Carminati. Magneto-optical control of förster energy transfer. *Physical Review B - Condensed Matter and Materials Physics*, 83:165426, 4 2011.

[80] Philip Trøst Kristensen and Stephen Hughes. Modes and mode volumes of leaky optical cavities and plasmonic nanoresonators. *ACS Photonics*, 1:2–10, 1 2013.

[81] A. Cazé, R. Pierrat, and R. Carminati. Spatial coherence in complex photonic and plasmonic systems. *Physical Review Letters*, 110:063903, 2 2013.

[82] Amnon Yariv and Pochi Yeh. *Photonics: optical electronics in modern communications (the oxford series in electrical and computer engineering)*. 2006.

[83] J. Hwang and E. A. Hinds. Dye molecules as single-photon sources and large optical nonlinearities on a chip. *New Journal of Physics*, 13:085009, 8 2011.

[84] J. E. Sipe, Robert W. Boyd, Ryan S. Bennink, and Young-Kwon Yoon. Accessing the optical nonlinearity of metals with metal–dielectric photonic bandgap structures. *Optics Letters, Vol. 24, Issue 20, pp. 1416-1418*, 24:1416–1418, 10 1999.

[85] Robert W. Boyd. Nonlinear optics. *Nonlinear Optics*, 2008.

[86] H. J. Simon, D. E. Mitchell, and J. G. Watson. Optical second-harmonic generation with surface plasmons in silver films. *Physical Review Letters*, 33:1531, 12 1974.

[87] Martti Kauranen and Anatoly V. Zayats. Nonlinear plasmonics. *Nature Photonics 2012 6:11*, 6:737–748, 11 2012.

[88] H. Wang, E. C.Y. Yan, E. Borguet, and K. B. Eisenthal. Second harmonic generation from the surface of centrosymmetric particles in bulk solution. *Chemical Physics Letters*, 259:15–20, 8 1996.

[89] P. Galletto, P. F. Brevet, H. H. Girault, R. Antoine, and M. Broyer. Enhancement of the second harmonic response by adsorbates on gold colloids: The effect of aggregation. *Journal of Physical Chemistry B*, 103:8706–8710, 10 1999.

[90] Markus Lippitz, Meindert A. Van Dijk, and Michel Orrit. Third-harmonic generation from single gold nanoparticles. *Nano Letters*, 5:799–802, 4 2005.

[91] Jérémy Butet, Julien Duboisset, Guillaume Bachelier, Isabelle Russier-Antoine, Emmanuel Benichou, Christian Jonin, and Pierre François Brevet. Optical second harmonic generation of single metallic nanoparticles embedded in a homogeneous medium. *Nano Letters*, 10:1717–1721, 5 2010.

[92] Yu Zhang, Nathaniel K. Grady, Ciceron Ayala-Orozco, and Naomi J. Halas. Three-dimensional nanostructures as highly efficient generators of second harmonic light. *Nano Letters*, 11:5519–5523, 12 2011.

[93] Wenjun Fan, Shuang Zhang, N. C. Panoiu, A. Abdenour, S. Krishna, R. M. Osgood, K. J. Malloy, and S. R.J. Brueck. Second harmonic generation from a nanopatterned isotropic nonlinear material. *Nano Letters*, 6:1027–1030, 5 2006.

[94] Kaspar D. Ko, Anil Kumar, Kin Hung Fung, Raghu Ambekar, Gang Logan Liu, Nicholas X. Fang, and Kimani C. Toussaint. Nonlinear optical response from arrays of au bowtie nanoantennas. *Nano Letters*, 11:61–65, 1 2010.

[95] Marta Castro-Lopez, Daan Brinks, Riccardo Sapienza, and Niek F. Van Hulst. Aluminum for nonlinear plasmonics: Resonance-driven polarized luminescence of al, ag, and au nanoantennas. *Nano Letters*, 11:4674–4678, 11 2011.

[96] Alain Dereux, Alexandre Bouhelier, Gérard Colas des Francs, Guillaume Bachelier, Johann Berthelot, Mingxia Song, and Padmnabh Rai. Silencing and enhancement of second-harmonic generation in optical gap antennas. *Optics Express, Vol. 20, Issue 10, pp. 10498-10508*, 20:10498–10508, 5 2012.

[97] Krishnan Thyagarajan, Jérémy Butet, and Olivier J.F. Martin. Augmenting second harmonic generation using fano resonances in plasmonic systems. *Nano Letters*, 13:1847–1851, 4 2013.

[98] Marie L. Sandrock, Charles D. Pibel, Franz M. Geiger, and Colby A. Foss. Synthesis and second-harmonic generation studies of noncentrosymmetric gold nanostructures. *Journal of Physical Chemistry B*, 103:2668–2673, 4 1999.

[99] Michele Celebrano, Xiaofei Wu, Milena Baselli, Swen Großmann, Paolo Biagioni, Andrea Locatelli, Costantino De Angelis, Giulio Cerullo, Roberto Osellame, Bert Hecht, Lamberto Duò, Franco Ciccacci, and Marco Finazzi. Mode matching in multiresonant plasmonic nanoantennas for enhanced second harmonic generation. *Nature Nanotechnology 2015 10:5*, 10:412–417, 4 2015.

[100] Brian K. Canfield, Hannu Husu, Janne Laukkanen, Benfeng Bai, Markku Kuittinen, Jari Turunen, and Martti Kauranen. Local field asymmetry drives second-harmonic generation in noncentrosymmetric nanodimers. *Nano Letters*, 7:1251–1255, 5 2007.

[101] Robert Czaplicki, Jouni Mäkitalo, Roope Siikanen, Hannu Husu, Joonas Lehtolahti, Markku Kuittinen, and Martti Kauranen. Second-harmonic generation from metal nanoparticles: Resonance enhancement versus particle geometry. *Nano Letters*, 15:530–534, 1 2015.

[102] P. Reichenbach, L. M. Eng, U. Georgi, and B. Voit. 3d-steering and superfocusing of second-harmonic radiation through plasmonic nano antenna arrays. *Journal of Laser Applications*, 24:042005, 7 2012.

[103] T. F. Heinz and D. P. Divincenzo. Comment on "forbidden nature of multipolar contributions to second-harmonic generation in isotropic fluids". *Physical Review A*, 42:6249, 11 1990.

[104] P. Guyot-Sionnest, W. Chen, and Y. R. Shen. General considerations on optical second-harmonic generation from surfaces and interfaces. *Physical Review B*, 33:8254, 6 1986.

[105] J. E. Sipe and Victor Mizrahi. Phenomenological treatment of surface second-harmonic generation. *JOSA B, Vol. 5, Issue 3, pp. 660-667*, 5:660–667, 3 1988.

[106] Sami Kujala, Brian K. Canfield, Martti Kauranen, Yuri Svirko, and Jari Turunen. Multipole interference in the second-harmonic optical radiation from gold nanoparticles. *Physical Review Letters*, 98:167403, 4 2007.

[107] Fu Xiang Wang, Francisco J. Rodríguez, Willem M. Albers, Risto Ahorinta, J. E. Sipe, and Martti Kauranen. Surface and bulk contributions to the second-order nonlinear optical response of a gold film. *Physical Review B - Condensed Matter and Materials Physics*, 80:233402, 12 2009.

[108] Debra Krause, Chartes W. Teplin, and Charles T. Rogers. Optical surface second harmonic measurements of isotropic thin-film metals: Gold, silver, copper, aluminum, and tantalum. *Journal of Applied Physics*, 96:3626, 9 2004.

[109] Christian Jonin, Emmanuel Benichou, Guillaume Bachelier, Isabelle Russier-Antoine, and Pierre-François Brevet. Multipolar second-harmonic generation in noble metal nanoparticles. *JOSA B, Vol. 25, Issue 6, pp. 955-960*, 25:955–960, 6 2008.

[110] Warren S. Warren, Herschel Rabitz, and Mohammed Dahleh. Coherent control of quantum dynamics: The dream is alive. *Science*, 259:1581–1589, 1993.

[111] Constantin Brif, Raj Chakrabarti, and Herschel Rabitz. Control of quantum phenomena: past, present and future. *New Journal of Physics*, 12:075008, 7 2010.

[112] Christopher J. Bardeen, Vladislav V. Yakovlev, Kent R. Wilson, Scott D. Carpenter, Peter M. Weber, and Warren S. Warren. Feedback quantum control of molecular electronic population transfer. *Chemical Physics Letters*, 280:151–158, 11 1997.

[113] N. H. Bonadeo, J. Erland, D. Gammon, D. Park, D. S. Katzer, and D. G. Steel. Coherent optical control of the quantum state of a single quantum dot. *Science*, 282:1473–1476, 11 1998.

[114] Jennifer L. Herek, Wendel Wohlleben, Richard J. Cogdell, Dirk Zeidler, and Marcus Motzkus. Quantum control of energy flow in light harvesting. *Nature 2002 417:6888*, 417:533–535, 2002.

[115] Patrick Nuernberger, Gerhard Vogt, Tobias Brixner, and Gustav Gerber. Femtosecond quantum control of molecular dynamics in the condensed phase. *Physical Chemistry Chemical Physics*, 9:2470–2497, 5 2007.

[116] Richard Hildner, Daan Brinks, Jana B. Nieder, Richard J. Cogdell, and Niek F. Van Hulst. Quantum coherent energy transfer over varying pathways in single light-harvesting complexes. *Science*, 340:1448–1451, 6 2013.

[117] Mark I. Stockman, Sergey V. Faleev, and David J. Bergman. Coherent control of femtosecond energy localization in nanosystems. *Physical Review Letters*, 88:067402, 1 2002.

[118] Martin Aeschlimann, Michael Bauer, Daniela Bayer, Tobias Brixner, F. Javier García De Abajo, Walter Pfeiffer, Martin Rohmer, Christian Spindler, and Felix Steeb. Adaptive subwavelength control of nano-optical fields. *Nature 2007 446:7133*, 446:301–304, 3 2007.

[119] A. Assion, T. Baumert, M. Bergt, T. Brixner, B. Kiefer, V. Seyfried, M. Strehle, and G. Gerber. Control of chemical reactions by feedback-optimized phase-shaped femtosecond laser pulses. *Science*, 282:919–922, 10 1998.

[120] R. J. Levis, G. M. Menkir, and H. Rabitz. Selective bond dissociation and rearrangement with optimally tailored, strong-field laser pulses. *Science*, 292:709–713, 4 2001.

[121] Doron Meshulach and Yaron Silberberg. Coherent quantum control of two-photon transitions by a femtosecond laser pulse. *Nature 1998 396:6708*, 396:239–242, 11 1998.

[122] T. Brixner, F. J.García De Abajo, C. Spindler, and W. Pfeiffer. Adaptive ultrafast nano-optics in a tight focus. *Applied Physics B 2006 84:1*, 84:89–95, 4 2006.

[123] T. Brixner, N. H. Damrauer, P. Niklaus, and G. Gerber. Photoselective adaptive femtosecond quantum control in the liquid phase. *Nature 2001 414:6859*, 414:57–60, 11 2001.

[124] Anthony P. Peirce, Mohammed A. Dahleh, and Herschel Rabitz. Optimal control of quantum-mechanical systems: Existence, numerical approximation, and applications. *Physical Review A*, 37:4950, 6 1988.

[125] Moshe. Shapiro and Paul. Brumer. Principles of the quantum control of molecular processes. page 354, 2003.

[126] Richard S. Judson and Herschel Rabitz. Teaching lasers to control molecules. *Physical Review Letters*, 68:1500, 3 1992.

[127] D. Meshulach, D. Yelin, and Y. Silberberg. Adaptive femtosecond pulse compression. *Optics Letters, Vol. 22, Issue 23, pp. 1793-1795*, 22:1793–1795, 12 1997.

[128] J. Kunde, M. Haiml, U. Keller, and U. Siegner. Adaptive pulse compression by two-photon absorption in semiconductors. *Optics Letters, Vol. 27, Issue 5, pp. 315-317*, 27:315–317, 3 2002.

[129] M. Galvan-Sosa, J. Portilla, J. Hernandez-Rueda, J. Siegel, L. Moreno, A. Ruiz De La Cruz, and J. Solis. Optimization of ultra-fast interactions using laser pulse temporal shaping controlled by a deterministic algorithm. *Applied Physics A 2013 114:2*, 114:477–484, 4 2013.

[130] Leonard Mandel and Emil Wolf. Optical coherence and quantum optics. *Optical Coherence and Quantum Optics*, 9 1995.

[131] Wilfried G.J.H.M. van Sark, Patrick L.T.M. Frederix, Ageeth A. Bol, Hans C. Gerritsen, and Andries Meijerink. Blueing, bleaching, and blinking of single cdse/zns quantum dots. *ChemPhysChem*, 3, 2002.

[132] Marco Allione, Ana Ballester, Hongbo Li, Alberto Comin, José L. Movilla, Juan I. Climente, Liberato Manna, and Iwan Moreels. Two-photon-induced blue shift of core and shell optical transitions in colloidal cdse/cds quasi-type ii quantum rods. *ACS Nano*, 7:2443–2452, 3 2013.

[133] Guichuan Xing, Yile Liao, Xiangyang Wu, Sabyasachi Chakrabortty, Xinfeng Liu, Edwin K.L. Yeow, Yinthai Chan, and Tze Chien Sum. Ultralow-threshold two-photon pumped amplified spontaneous emission and lasing from seeded cdse/cds nanorod heterostructures. *ACS Nano*, 6:10835–10844, 12 2012.

[134] Xiangping Li, Joel Van Embden, James W.M. Chon, and Min Gu. Enhanced two-photon absorption of cds nanocrystal rods. *Applied Physics Letters*, 94:103117, 3 2009.

[135] Y. S. Park, A. V. Malko, J. Vela, Y. Chen, Y. Ghosh, F. García-Santamaría, J. A. Hollingsworth, V. I. Klimov, and H. Htoon. Near-unity quantum yields of biexciton emission from cdse/cds nanocrystals measured using single-particle spectroscopy. *Physical Review Letters*, 106:187401, 5 2011.

[136] Gautham Nair, Jing Zhao, and Moungi G. Bawendi. Biexciton quantum yield of single semiconductor nanocrystals from photon statistics. *Nano Letters*, 11:1136–1140, 3 2011.

[137] Tak San Ho and Herschel Rabitz. Why do effective quantum controls appear easy to find? *Journal of Photochemistry and Photobiology A: Chemistry*, 180:226–240, 6 2006.

[138] Herschel A. Rabitz, Michael M. Hsieh, and Carey M. Rosenthal. Quantum optimally controlled transition landscapes. *Science*, 303:1998–2001, 3 2004.

[139] Lukasz Piatkowski, Esther Gellings, and Niek F. Van Hulst. Broadband single-molecule excitation spectroscopy. *Nature Communications 2016 7:1*, 7:1–9, 1 2016.

[140] Bingwei Xu, Chien hung Tseng, Ian Borukhovich, Marcos Dantus, Thomas Weinacht, Tissa C. Gunaratne, Vadim V. Lozovoy, and Yves Coello. Interference without an interferometer: a different approach to measuring, compressing, and shaping ultrashort laser pulses. *JOSA B, Vol. 25, Issue 6, pp. A140-A150*, 25:A140–A150, 6 2008.

[141] Doron Meshulach and Yaron Silberberg. Coherent quantum control of multiphoton transitions by shaped ultrashort optical pulses. *Physical Review A*, 60:1287, 8 1999.

[142] Marcos Dantus and Vadim V. Lozovoy. Experimental coherent laser control of physicochemical processes. *Chemical Reviews*, 104:1813–1859, 4 2004.

[143] L. Bonacina, Y. Mugnier, F. Courvoisier, R. Le Dantec, J. Extermann, Y. Lambert, V. Boutou, C. Galez, and J. P. Wolf. Polar fe(io3)3 nanocrystals as local probes for nonlinear microscopy. *Applied Physics B 2007 87:3*, 87:399–403, 3 2007.

[144] Jerome Extermann, Luigi Bonacina, Francois Courvoisier, Denis Kiselev, Yannick Mugnier, Ronan Le Dantec, Christine Galez, Jean-Pierre Wolf, Ja Squier, M Muller, G J Brakenhoff, and K R Wilson. Nano-frog: Frequency resolved optical gating by a nanometric object. *Optics Express, Vol. 16, Issue 14, pp. 10405-10411*, 16:10405–10411, 7 2008.

[145] Paweł Wnuk, Loc Le Xuan, Abdallah Slablab, Cédric Tard, Sandrine Perruchas, Thierry Gacoin, Jean-François Roch, Dominique Chauvat, Czesław Radzewicz, Y Nakayama, P J Pauzauskie, A Radenovic, R M Onorato, R J Saykally, J Liphard, P Yang, Le Xuan, C Zhou, A Slablab, D Chauvat, C Tard, S Perruchas, T Gacoin, P Villeval, J f, J F Roch, and S Brasselet. Coherent nonlinear emission from a single ktp nanoparticle with broadband femtosecond pulses. *Optics Express, Vol. 17, Issue 6, pp. 4652-4658*, 17:4652–4658, 3 2009.

[146] Achim Hartschuh, Alberto Comin, Giovanni Piredda, Kevin Donkers, and Richard Ciesielski. Compression of ultrashort laser pulses via gated multiphoton intrapulse interference phase scans. *JOSA B, Vol. 31, Issue 5, pp. 1118-1125*, 31:1118–1125, 5 2014.

[147] Daan Brinks, Fernando D. Stefani, Florian Kulzer, Richard Hildner, Tim H. Taminiau, Yuri Avlasevich, Klaus Müllen, and Niek F. Van Hulst. Visualizing and controlling vibrational wave packets of single molecules. *Nature 2010 465:7300*, 465:905–908, 6 2010.

[148] X. Michalet, F. F. Pinaud, L. A. Bentolila, J. M. Tsay, S. Doose, J. J. Li, G. Sundaresan, A. M. Wu, S. S. Gambhir, and S. Weiss. Quantum dots for live cells, in vivo imaging, and diagnostics. *Science*, 307:538–544, 1 2005.

[149] Daniell R. Larson, Warren R. Zipfel, Rebecca M. Williams, Stephen W. Clark, Marcel P. Bruchez, Frank W. Wise, and Watt W. Webb. Water-soluble quantum dots for multiphoton fluorescence imaging in vivo. *Science*, 300:1434–1436, 5 2003.

[150] J. S. Bell. On the einstein podolsky rosen paradox. *Physics Physique Fizika*, 1:195, 11 1964.

[151] John F. Clauser, Michael A. Horne, Abner Shimony, and Richard A. Holt. Proposed experiment to test local hidden-variable theories. *Physical Review Letters*, 23:880, 10 1969.

[152] A. V. Akimov, A. Mukherjee, C. L. Yu, D. E. Chang, A. S. Zibrov, P. R. Hemmer, H. Park, and M. D. Lukin. Generation of single optical plasmons in metallic nanowires coupled to quantum dots. *Nature 2007 450:7168*, 450:402–406, 11 2007.

[153] Roman Kolesov, Bernhard Grotz, Gopalakrishnan Balasubramanian, Rainer J. Stöhr, Aurélien A.L. Nicolet, Philip R. Hemmer, Fedor Jelezko, and Jörg Wrachtrup. Wave–particle duality of single surface plasmon polaritons. *Nature Physics 2009 5:7*, 5:470–474, 5 2009.

[154] Abram L. Falk, Frank H.L. Koppens, Chun L. Yu, Kibum Kang, Nathalie De Leon Snapp, Alexey V. Akimov, Moon Ho Jo, Mikhail D. Lukin, and Hongkun Park. Near-field electrical detection of optical plasmons and single-plasmon sources. *Nature Physics 2009 5:7*, 5:475–479, 5 2009.

[155] Reinier W. Heeres, Sander N. Dorenbos, Benny Koene, Glenn S. Solomon, Leo P. Kouwenhoven, and Valery Zwiller. On-chip single plasmon detection. *Nano Letters*, 10:661–664, 2 2010.

[156] Reinier W. Heeres, Leo P. Kouwenhoven, and Valery Zwiller. Quantum interference in plasmonic circuits. *Nature Nanotechnology 2013 8:10*, 8:719–722, 8 2013.

[157] James S. Fakonas, Hyunseok Lee, Yousif A. Kelaita, and Harry A. Atwater. Two-plasmon quantum interference. *Nature Photonics 2014 8:4*, 8:317–320, 3 2014.

[158] E. Altewischer, M. P. Van Exter, and J. P. Woerdman. Plasmon-assisted transmission of entangled photons. *Nature 2002 418:6895*, 418:304–306, 7 2002.

[159] Esteban Moreno, F. J. García-Vidal, Daniel Erni, J. Ignacio Cirac, and L. Martín-Moreno. Theory of plasmon-assisted transmission of entangled photons. *Physical Review Letters*, 92:236801, 6 2004.

[160] Sylvain Fasel, Franck Robin, Esteban Moreno, Daniel Erni, Nicolas Gisin, and Hugo Zbinden. Energy-time entanglement preservation in plasmon-assisted light transmission. *Physical Review Letters*, 94:110501, 3 2005.

[161] Sylvain Fasel, Matthäus Halder, Nicolas Gisin, and Hugo Zbinden. Quantum superposition and entanglement of mesoscopic plasmons. *New Journal of Physics*, 8:13, 1 2006.

[162] Javier Del Pino, Johannes Feist, F. J. García-Vidal, and Juan Jose García-Ripoll. Entanglement detection in coupled particle plasmons. *Physical Review Letters*, 112:216805, 5 2014.

[163] S. P. Walborn, M. O. Terra Cunha, S. Pádua, and C. H. Monken. Double-slit quantum eraser. *Physical Review A*, 65:033818, 2 2002.

[164] Marian O. Scully, Berthold Georg Englert, and Herbert Walther. Quantum optical tests of complementarity. *Nature 1991 351:6322*, 351:111–116, 1991.

[165] G.I. TAYLOR. Interference fringes with feeble light, 1983.

[166] M. Arndt, M. Aspelmeyer, H. J. Bernstein, R. Bertlmann, C. Brukner, J. P. Dowling, J. Eisert, A. Ekert, C. A. Fuchs, D. M. Greenberger, M. A. Horne, T. Jennewein, P. G. Kwiat, N. D. Mermin, J. W. Pan, E. M. Rasel, H. Rauch, T. G. Rudolph, C. Salomon, A. V. Sergienko, J. Schmiedmayer, C. Simon, V. Vedral, P. Walther, G. Weihs, P. Zoller, and M. Zukowski. Quantum physics from a to z. 5 2005.

[167] Anton Zeilinger, Gregor Weihs, Thomas Jenmewein, and Markus Aspelmeyer. Happy centenary, photon. *Nature 2005 433:7023*, 433:230–238, 1 2005.

[168] R. Mir, J. S. Lundeen, M. W. Mitchell, A. M. Steinberg, J. L. Garretson, and H. M. Wiseman. A double-slit 'which-way' experiment on the complementarity–uncertainty debate. *New Journal of Physics*, 9:287, 8 2007.

[169] Patrick J. Coles, Jedrzej Kaniewski, and Stephanie Wehner. Equivalence of wave–particle duality to entropic uncertainty. *Nature Communications 2014 5:1*, 5:1–8, 12 2014.

[170] Berthold Georg Englert. Fringe visibility and which-way information: An inequality. *Physical Review Letters*, 77:2154, 9 1996.

[171] Gregg Jaeger, Abner Shimony, and Lev Vaidman. Two interferometric complementarities. *Physical Review A*, 51:54, 1 1995.

[172] Daniel M. Greenberger and Allaine Yasin. Simultaneous wave and particle knowledge in a neutron interferometer. *Physics Letters A*, 128:391–394, 4 1988.

[173] H. J. Lezec, A. Degiron, E. Devaux, R. A. Linke, L. Martin-Moreno, F. J. Garcia-Vidal, and T. W. Ebbesen. Beaming light from a subwavelength aperture. *Science*, 297:820–822, 8 2002.

[174] C. Genet, F. J. Garcia-Vidal, L. Martin-Moreno, O. Mahboub, S. Carretero Palacios, Sergio G. Rodrigo, and T. W. Ebbesen. Optimization of bull's eye structures for transmission enhancement. *Optics Express, Vol. 18, Issue 11, pp. 11292-11299*, 18:11292–11299, 5 2010.

[175] Aurélien Drezet, Cyriaque Genet, and Thomas W. Ebbesen. Miniature plasmonic wave plates. *Physical Review Letters*, 101:043902, 7 2008.

[176] Yuri Gorodetski, Emmanuel Lombard, Aurélien Drezet, Cyriaque Genet, and Thomas W. Ebbesen. A perfect plasmonic quarter-wave plate. *Applied Physics Letters*, 101:201103, 11 2012.

[177] Fabian Steinlechner, Pavel Trojek, Marc Jofre, Henning Weier, Daniel Perez, Thomas Jennewein, Rupert Ursin, John Rarity, Morgan W Mitchell, Juan P Torres, Harald Weinfurter, Valerio Pruneri, D Bouwmeester, J w Pan, K Mattle, M Eibl, H Weinfurter, and A Zeilinger. A high-brightness source of polarization-entangled photons optimized for applications in free space. *Optics Express, Vol. 20, Issue 9, pp. 9640-9649*, 20:9640–9649, 4 2012.

[178] Marissa Giustina, Marijn A.M. Versteegh, Sören Wengerowsky, Johannes Handsteiner, Armin Hochrainer, Kevin Phelan, Fabian Steinlechner, Johannes Kofler, Jan Åke Larsson, Carlos Abellán, Waldimar Amaya, Valerio Pruneri, Morgan W. Mitchell, Jörn Beyer, Thomas Gerrits, Adriana E. Lita, Lynden K. Shalm, Sae Woo Nam, Thomas Scheidl, Rupert Ursin, Bernhard Wittmann, and Anton Zeilinger. Significant-loophole-free test of bell's theorem with entangled photons. *Physical Review Letters*, 115:250401, 12 2015.

[179] Hatim Salih. Quantum erasure cryptography. *Frontiers in Physics*, 4:16, 5 2016.

[180] Xin He Jiang, Peng Chen, Kai Yi Qian, Zhao Zhong Chen, Shu Qi Xu, Yu Bo Xie, Shi Ning Zhu, and Xiao Song Ma. Quantum teleportation mediated by surface plasmon polariton. *Scientific Reports 2020 10:1*, 10:1–8, 7 2020.

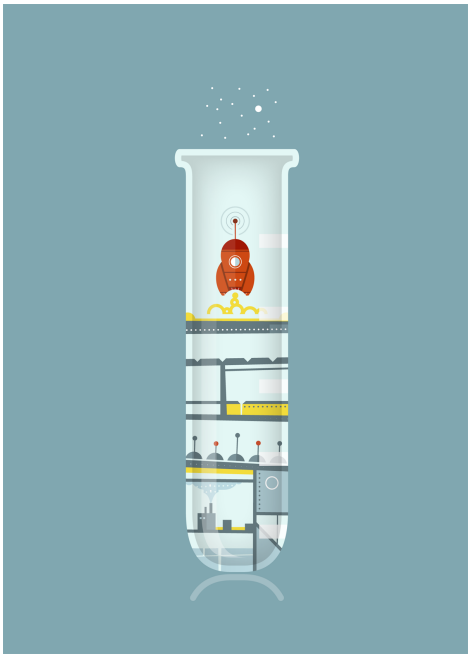

This thesis was typeset using LaTeX, originally developed by Leslie Lamport and based on Donald Knuth's TeX. The body text is set in 11 point Egenolff-Berner Garamond, a revival of Claude Garamont's humanist typeface. The above illustration, *Science Experiment 02*, was created by Ben Schlitter and released under CC BY-NC-ND 3.0. A template that can be used to format a PhD dissertation with this look & feel has been released under the permissive AGPL license, and can be found online at github.com/suchow/Dissertate or from its lead author, Jordan Suchow, at suchow@post.harvard.edu.